FLINDERS
UNIVERSITY
ADELAIDE
AUSTRALIA

FEM Analysis of an Amplified Bidirectional Piezoelectric Actuator for Shape Control of Thermally Distorted Structures

by

Christian van der Horst, *B.Eng. (Electrical),*
School of Computer Science, Engineering and Mathematics,
Faculty of Science and Engineering

July 2011

A thesis presented to the
Flinders University of South Australia
in total fulfilment of the requirements for the degree of
Masters of Engineering (research)

Adelaide, South Australia, 2011

Contents

List of Figures

List of Tables

LIST OF TABLES

Abstract

Increasingly, engineers are pushing the boundaries of aerospace vehicles to fly at hypersonic speeds of Mach 10. However, flying at these speeds introduces aerothermoelastic problems, since the skin of the hypersonic vehicle is subjected to friction with the hypersonic airstream. As a result, the skin demonstrates deformation as well as melting of the leading edges of the vehicle.

A significant amount of research has been conducted to control this deformation by employing an actuator that is bonded on, or within, the structure. The actuator usually consists of a smart material that is able to change one or more of its properties under the influence of an external stimulus, e.g. electric field, stress or temperature. One of the challenges that arises, is that, under the influence of high temperature, the performance and properties of the smart materials change. Furthermore, the actuator must typically be able to generate sufficient force and displacement in order to compensate for the thermally induced deformation. The generated force and displacement depends on the amount of external stimulus applied to the smart material, as well as the magnitude of actuator authority that the smart material can produce. However, when shape control is applied to aerospace structures, such as a hypersonic vehicle, the possibility to generate a large amount of external stimulus is not always guaranteed. The deformation that occurs when a structure is subjected to thermal loading is bidirectional, forcing the structure to exhibit a displacement orthogonal to the original shape. The challenge arises that most smart materials used for shape control exhibit unidirectional or semi-bidirectional displacements and, therefore, only compensate for shape distortions in one direction. In order to achieve shape compensation of thermally exposed

structures, there is a need for a bidirectional actuator that is able to generate large strains and forces to counteract the thermal stress. In this research, two amplified bidirectional actuators are proposed, namely: the Amplified Dual-Stack Actuator (ADSA) and the Amplified Bidirectional Actuator (ABA). The actuators can be mounted to one side of a structure and are able to compensate for the deformation generated by the thermally induced loading. The actuators are self-preloading, which eliminates the need of a preload spring to protect the actuators against tensile stresses. Moreover, the actuators are able to operate under a relatively small external stimulus.

Both actuators consist of a bidirectional actuator that employs two piezoelectric ring-stack elements. The piezoelectric stacks are operated in opposing fashion, i.e. when the first stack contracts, the second extends and vice versa. The displacements generated by the bidirectional actuator are amplified using a diamond-shaped amplifying compliant structure. To identify the actuation performance and thoroughly study the behaviour of the actuators, theoretical calculations and finite element simulations are conducted. A benchmark finite element model is built containing a beam structure that is subjected to thermal loading by two film heaters and is actively compensated using two piezoelectric patches, which are mounted either side of the structure. The compensation performance of the proposed amplified actuators is then identified by mounting the actuators to an identical beam structure as used in the benchmark model.

A comparison of the compensation performance of the ADSA and the ABA against that of the benchmark model, demonstrates that both actuators are able to compensate for shape deformations of the beam structure. The main advantage of the proposed actuators is their ability to generate equal bidirectional displacements to control the shape of a structure, when mounted to only one side of the structure. Furthermore, the actuators are actuated by applying a relatively low electrical field and obtain self-preloading capabilities.

This study servers as a foundation to examine the potential of using amplified bidirectional actuators to control the shape of a hypersonic vehicle, and demonstrates that the proposed actuators show promise to be used for control of bidirectional shape deformations.

List of Abbreviations

1-D	One-Dimensional
2-D	Two-Dimensional
3-D	Three-Dimensional
ABA	Amplified Bidirectional Actuator
AC	Alternating Current
ADSA	Amplified Dual-Stack Actuator
APC	American Piezo Ceramics
APDL	ANSYS Parametric Design Language
BMT	Barium Magnesium Tantalate
BST	Barium Strontium Titanate
BT	Bismuth Titanate
DC	Direct Current
DOF	Degrees Of Freedom
FEM	Finite Element Method
FSDT	First-order Shear Deformation Theory
LiNbO3	Lithium Niobate
MFC	Macro-Fibre Composite
MIMO	Multiple Input Multiple Output
MPC	Multi Point Constraint
NiTiCu	Nickel-Titanium-Copper
Nitinol	Nickel-Titanium Naval Ordnance Laboratory
PID	Proportional Integral Derivative
PVDF	Polyvinylidene Fluoride
PZT	Lead Zirconate Titanate
SMA	Shape Memory Alloy
UX	Displacement in X-direction
UY	Displacement in Y-direction
UZ	Displacement in Z-direction

Certification

I certify that this thesis does not incorporate, without acknowledgement, any material previously submitted for a degree or diploma in any university; and that, to the best of my knowledge and belief, it does not contain any material previously published or written by another person except where due reference is made in the text.

Adelaide, 19 July 2011

Christian van der Horst

Acknowledgements

I would like to thank my supervisors Assoc. Prof. Karl Sammut and Assoc. Prof. Fangpo He for their support and guidance throughout this journey. Their patience, time, knowledge and constructive criticism kept me inspired and motivated. Karl, thank you for giving me the opportunity that allowed me to come back and do my research. To Fangpo, thank you for your valuable input and discussions in the meetings and the long-distance phone conversations we have had.

I want to give thanks to the staff of the School of Computer Science, Engineering and Mathematics for helping me deal with paperwork, computer problems and the casual chats over lunch. Thanks to Sharon who always provided the so important coffee, and giving me the opportunity to go and watch AFL games.

Writing this thesis in a second language was a challenge but it turned out in a good shape and a great accomplishment thanks to the proofreading of June Persico and Kate Deller-Evans.

To my family who has supported me throughout my life and especially these two years of my research, my heartfelt thanks go to Dad, Mum, Hans and Yvonne. Thanks for your love, the advice during our weekly Skype conversations, and the financial support, which made this journey possible.

I would like to say thank you to Katrina for her love, understanding, support, and encouragement during the preparation of this thesis. You were a very important person to me the last couple of months of my research. The research was quite demanding on my time and our relationship, but we have prevailed.

Finally, I want to thank Dino, June, Chris and Holly, for their support,

encouragement and good times during the family night dinners. It really made me relax and wind down after a busy and stressful week of work and study.

Christian van der Horst

July 2011

Adelaide

I dedicate this thesis in honour of my beloved grandfather

Leonardus Hubertus Oijen

Chapter 1

Introduction

This chapter begins with addressing the motivation for the work conducted in this research. The research methodology is presented and followed by a literature review. Finally, an outline of the thesis is given, along with a list of original contributions.

1.1 Motivation

The pursuit of pushing the boundaries of aerospace vehicles and achieving developments that seemed impossible decades ago, has led to new research challenges. The quest to fly faster than sound, which seemed a difficult enough challenge in the 1950s, is currently superseded by attempts to fly at Mach 10.

Hypersonics is an area of re-emerging interest after the success of the HyShot 2 test flight in Woomera, South Australia, in July 2002, which demonstrated the world's first supersonic combustion in an atmospheric flight. Also the two NASA X-43a test flights in March and November 2004, where the scramjet engine worked successfully at nearly Mach 7 and Mach 10, respectively [1]. However, flying at these speeds introduces aerothermoelastic problems since the skin of the vehicle is subjected to friction with the hypersonic airstream, which causes the skin to deform as well as melting of the leading edges of the vehicle.

Figure 1.1 X-43a hypersonic vehicle from NASA [2]

These demands and challenges have forced researchers to develop lighter and more advanced composite materials to increase performance and to overcome undesirable thermal effects. In addition, a large amount of research is conducted in the area of shape control. However, shape control of structures, induced by thermal loading, remains a challenging task due to the following factors:

1. In order to achieve shape control of a structure that is subjected to thermal loading, an actuator is required that is bonded or connected to the structure. The actuator usually consists of a smart material that is able to change one or more of its properties under the influence of an external stimulus. The challenge arises that the performance and properties of the smart materials change under the influence of thermal loads [3, 4].

2. To activate the smart material, an external stimulus is required. This stimulus can be in the form of a temperature, electrical field, magnetic field, flux or stress applied to the material. In the field of shape control, relatively large displacements are required from the smart material [5], in response to the amount of external stimulus applied. However, when shape control is applied to aerospace structures, as discussed in previous examples, the possibility to

generate a large amount of electrical field, magnetic field, flux, stress or temperature is not always guaranteed.

3. Structural deformation occurs when a structure is subjected to thermal loading causing distortion and bulging of the surface. These distortions are bidirectional, forcing the surface to exhibit a displacement orthogonal to the undistorted shape [1]. However, most smart materials used for shape control exhibit only unidirectional or semi-bidirectional displacements and therefore are only able to compensate for shape distortions in one direction.

In order to achieve shape compensation of thermally exposed structures, there is a need for a bidirectional actuator that is able to generate large strains and forces to counteract the thermal stress. Moreover, the actuator must be able to operate under a relatively small external stimulus and be resistant to high temperatures and harsh environments, such as vibrations and high-pressure environments. The weight of the actuator is also a very important factor, since the range and manoeuvrability will be reduced when several actuators are bonded to an aerospace vehicle. Other desirable requirements include employing a minimum number of actuators and using the actuator simultaneously as both a sensor and actuator, i.e. a *sensoriactuator* [6]. Given these requirements, the motivation of this research is to design and implement an actuator that is capable of meeting most of these requirements.

1.2 Research Methodology

The research methodology consists of three steps. In the first step, a literature review is conducted that starts by defining smart structures and smart materials and covers the properties, advantages and disadvantages of several smart materials that are suitable for shape compensation. According to certain selection criteria defined in the next section, which is specific to the aim of this study, the most suitable smart material is selected. The review continues to cover shape control studies and applications that use an identical smart material. Gaps and drawbacks of current

techniques are identified and discussed and, based on these shortcomings, a new actuator is proposed.

In the second step, an existing actuator is modelled and theoretically analysed to identify its performance and behaviour. To validate the theoretical model and further identify the behaviour of the actuator, a finite element model is generated and a piezoelectric analysis is conducted. Based on the results of the finite element analysis, modifications are then made to the design in order to obtain optimal performance of the actuator.

In the third step, a benchmark model is created to analyse the performance of the proposed bidirectional actuator. The model consists of a beam structure with two film heaters, each bonded to either surface of the structure, to induce a thermal difference through the thickness of the structure. Two piezoelectric patches, each mounted to either surface of the beam structure, compensate for the thermal deformation. A structural-thermoelectric coupled-field analysis is conducted to identify the compensation performance of the two piezoelectric patches. This compensation method used in the benchmark model is similar to the technique applied by other researchers [7, 8]. The proposed bidirectional actuator is then mounted to an identical beam structure, as used in the benchmark, and an identical analysis is conducted to evaluate the effectiveness and compensation performance of the proposed actuator.

1.3 Smart Structures and Materials

Smart materials have continuously gained attention in the past decade, due to the increasing demand for smart structures. *Smart structures* can be defined as structures that utilise the coupling properties of smart materials to provide functionality [9]. In the same context, Rogers and Giurgiutiu [10] defined smart structures as the integration of actuators, sensors and controls with a material or structural component. An example of a smart material system is the use of smart material ceramics as a means to control the vibrations induced in the vertical tails of a jet fighter [11, 12]. Another specific example is the use of a smart material to precisely control the shape

of a large-scale space antenna [13]. Other names for smart structures frequently used within the literature are: *smart material systems*, *intelligent structures*, *adaptive structures*, *active structures*, *adaptronics* or *structronics*.

Smart materials are defined as materials that exhibit coupling and convert energy between multiple physical domains, where a domain is any physical quantity that can be described by a set of two variables [9]. An example of a physical domain that is discussed in this thesis is the mechanical domain, whose state variables are stress and strain within a material as described in Table 1.1. The coupling occurs when a change in the state variable, in one physical domain, causes a change in the state variable of a separate physical domain. For example, changing the electrical field applied to a material, which is a state variable of the electrical domain, can cause a change in the state of strain, which is the mechanical domain. This type of coupling is called *electromechanical coupling*.

This section continues focusing on four types of smart materials with the purpose of creating a general overview of the available smart materials and their properties. Furthermore, the general advantages and disadvantages of each material are studied, when the materials are used for shape control.

Piezoelectric ceramics, which are the first set of materials studied, have the ability to convert energy between the mechanical and electrical domains and vice versa. The second set of materials studied are the shape memory alloys, which are thermomechanical materials that deform when heated and cooled. The third set of materials studied are the magnetostrictive materials, which changes their shape or dimensions during the process of magnetisation.

Mechanical	**Electrical**	**Thermal**	**Magnetic**	**Chemical**
Stress	Electric field	Temperature	Magnetic field	Concentration
Strain	Electric displacement	Entropy	Magnetic flux	Volumetric flux

Table 1.1 Example of physical domains and associated state variables [9]

Piezoelectric polymers that exhibit electromechanical coupling, are the fourth and last set of materials studied. The piezoelectric polymer materials are similar to the piezoelectric materials but exhibit different electromechanical response characteristics.

Important material properties such as density, elastic modulus, stress, energy density and response speed of each smart material are compared to find the most suitable actuator for this study. In addition to the material properties, the operating temperature, field strength to activate the material, and complexity to mount or integrate the smart material to a structure, are taken into account. The stress and the strain properties are used to compare the different materials with each other since they are intrinsic properties. *Intrinsic properties* are properties that do not depend on the geometry, whereas *extrinsic properties* do depend on the geometry, for example, force and displacement.

An enormous variation in data concerning the mechanical and active properties of smart materials can be observed in the literature, since most of the data is provided by different manufacturers [14]. The cause for this variation is the difference in composition of each smart material. In addition, different manufacturers can use different measuring methods to measure the performance of the material, since there is no standardised method. Therefore, close correspondence with the manufacturers and the request for a specific measurement report is strongly recommended.

1.3.1 Piezoelectric Ceramics

In the late nineteenth century, the brothers Curie discovered several natural materials, including quartz, which exhibit an interesting property. They demonstrated that an electric output is produced when a mechanical strain is imposed on the material. They verified this coupling by measuring the charge induced across electrodes placed on the material when it underwent an imposed deformation. This phenomenon is described as the *direct piezoelectric effect*. Some years later, it was demonstrated that a mechanical strain is induced when an electrical field is applied to the material, which is described in the literature as the *converse piezoelectric effect*.

There are many different types of piezoelectric material manufactured and it is

virtually impossible to mention all the specific properties of each type. An example of a widely used piezoelectric material is lead zirconate titanate (PZT). This material is subdivided into Navy Type I to Navy Type IV, which all have different properties. Other examples are lithium niobate (LiNbO3) and bismuth titanate (BT), which are both high temperature piezoelectric materials. Therefore, the following material properties mentioned in this section are specified in ranges, which cover the largest part of the piezoelectric materials.

The density of piezoelectric materials is typically in the range of 7000 to 8000 kg/m^3 and the elastic modulus of piezoelectric materials has values of the order of 10 to 100 GPa, depending on the type and composition of the material. Piezoelectric materials generate a relatively small strain of approximately one part in thousand or 0.1%, compared to other smart materials [14]. However, because of the material's high elastic modulus, the generated stress is high and depending if the material is a hard or soft ceramic generally has a value between the 1 and 50 MPa. The volumetric energy density can be calculated when the stress is multiplied by the strain of the material. *Energy* is defined as the capacity to do work and *volumetric energy density* is defined as the capacity to do work per unit volume [9]. Even though the strain of the piezoelectric material is limited, the energy density of the material is of the order of 10 to 100 kJ/m^3. The reason for this is that the material is relatively stiff and induces a high stress. The *response speed* of the material is very fast and is generally defined as the rate of change of the displacement, strain, or force of the material when there is a variation at the applied input energy. The response speed of piezoelectric material depends on the size and type of material used and it is possible to get a response time of the order of microseconds. Therefore, the piezoelectric material can operate from the near static to the high-frequency range [15].

Several studies have been conducted concerning the thermal effect on the properties of piezoelectric material. When the operating temperature increases, the piezoelectric performance of the material slightly decreases until depolarisation occurs at the Curie point. The *Curie point* is the maximum exposure temperature for any piezoelectric material, and once it is heated above this point, all piezoelectric properties are lost.

Sherrit *et al.* [16] conducted a small signal resonance study on thickness and radial or ring modes of a series of piezoelectric samples with a Curie temperature greater than 400 °C. The aim of the study was to establish the capability of piezoelectric materials to operate at the ambient temperature of Venus, which is 460 °C. This study determined that the bismuth titanate material is stable up to 500 °C, whereas the barium strontium titanate (BST) and barium magnesium tantalate (BMT) material samples are depoled between 400 °C and 500 °C. These results are very promising for the use of piezoelectric materials in high temperature environments. However, a drawback of using bismuth titanate material for shape control is the fact that it has a relatively low piezoelectric strain coefficient. The *piezoelectric strain coefficient* relates the generated mechanical strain to the applied electrical field and has units of metres per volt (m/V). Therefore, a material with a high piezoelectric strain coefficient is capable of generating a larger strain than a material with a low piezoelectric strain coefficient, when both materials are subjected to the same electrical field strength. If an application requires a piezoelectric actuator that is able to generate a large strain, a piezoelectric material with a high piezoelectric strain coefficient should be used.

A study on the electrical properties of PZT piezoelectric material at high temperatures was conducted by Gubinyi *et al.* [3]. Whereas the study of Sherrit *et al.* [16] focussed on bismuth titanate piezoelectric material, Gubinyi *et al.* studied the temperature effect on the piezoelectric properties of PZT Navy Type II material. The PZT samples were subjected to controlled temperatures ranging from 25 °C to 400 °C. Gubinyi *et al.*'s findings were that the temperature-dependent piezoelectric constant d_{33} is stable up to 200 °C and the coupling factor k_{33} is found to be relatively constant up to 150 °C and only exhibits slight temperature dependence above 200 °C. These results indicate that the operating temperature of PZT material, which is around 200 °C [17], is lower than the operating temperature of bismuth titanate, which is stable up to 500 °C. In practice, the typical operation temperature limits are about two-thirds of the ceramic's Curie point [18]. However, the piezoelectric constant of PZT is about ten times larger than bismuth titanate, making it more suitable for shape control.

Kazys *et al.* [17] reviewed over ten piezoelectric materials suitable for operating at high temperatures for use in ultrasonic transducers. Their focus was mainly on the operating temperature of the material and the bonding method used to connect the piezoelectric material to the structure. The authors concluded that bismuth titanate is one of the most suitable piezoelectric materials. However, the application for this piezoelectric element was in the ultrasonic frequency range and their conclusion was based on the operating temperature and bonding methods. Alongside the PZT and bismuth titanate materials, the authors also reviewed the high temperature material Lithium Niobate, which has a Curie temperature of 1210 °C. Kazys *et al.* states that at 600 °C, Lithium Niobate starts to lose oxygen to the environment, which makes it unsuitable to use for their application. However, since the operating temperature of 600 °C of Lithium Niobate is still higher than the operating temperature of PZT and bismuth titanate, it is possibly more suitable to be used for shape control.

Kawamata *et al.* [19] studied the performance of a multilayered Lithium Niobate actuator and, by optimising the cutting angle to cut each piezoelectric layer out of a ceramic block, created a perfect linear actuator with no hysteresis. However, the piezoelectric constant is still relatively low at 38 pC/N, compared to 374 pC/N for a Navy Type II material, which limits the strain of the actuator. Therefore, Kawamate *et al.* applied an electrical field as high as 700 V to the electrodes of the material to achieve a displacement of $300E^{-9}$ m with a $10.5E^{-3}$ m actuator.

Piezoelectric material is a very suitable candidate for both shape and vibration control of structures. An advantage of piezoelectric material is that it is controllable by a broad electrical field up to one thousand volts. Because of the material's high elastic modulus, it is able to generate a large amount of force up to one kilonewton. The material can be used for applications from the near static to the high frequency range and it has a fast response time. However, piezoelectric materials have the limitation that they are *semi-bidirectional*, which means that the largest amount of displacement is generated in the extending direction and only a small amount in the contracting direction. The reason for this is that, when a large electrical field is applied opposite to the polarisation direction, the piezoelectric material depolarises and loses its piezoelectric properties. Another drawback of piezoelectric material is its limited strain generation, which is approximately 0.1%. The material's

characteristic is approximately linear since the material does exhibit hysteresis of 2% for very small signals and reaches 10 to 15% at nominal voltage [14].

1.3.2 Shape Memory Alloys

Although the shape memory effect was long known to exist in certain materials, it was not until 1965 when the Naval Ordnance Laboratory in the United States developed a material with a significant strong shape memory effect [9]. Researchers demonstrated that an alloy of nickel and titanium exhibited significant shape memory properties when heated and named the material nitinol (Nickel-Titanium Naval Ordnance Laboratory). *Shape memory alloys*, or SMAs, are materials that induce a large mechanical strain when they are heated or cooled. Many shape memory materials are metal alloys and, therefore, also produce a large mechanical stress when thermally activated, which makes them well suited for applications in controllable shape change [9]. SMA materials have two stable phases, i.e. a high temperature phase, which is called the *austenite* and a low-temperature phase, called the *martensite*. These materials can exhibit a one-way shape memory effect or a two-way shape memory effect. When the material exhibits a one-way effect, the material is soft and easily deformable in the austenite phase and, when heated to the martensite phase, the material resumes to its original shape and will stay in its original shape until it is deformed again. It remembers only one shape. The two-way effect indicates that the material remembers two different shapes and returns to one of those shapes by either heating or cooling.

The density and elastic modulus of the shape memory alloys are in the same range as the piezoelectric ceramics, with density values in the range of 7000 to 8000 kg/m^3 and an elastic modulus of approximately 10 to 100 GPa. SMAs have the ability to produce large strains of the order of 4 to 8% and their stress generation is in the same range as piezoelectric ceramics, which is between 5 and 50 MPa. The energy density of SMAs is very high since the material exhibits a large strain and stress and has a value in the range of 5 to 500 kJ/m^3. The time response of shape memory alloys is limited by the speed with which the stimulus can cause changes in the molecular structure of the alloy and is generally limited to a time scale of the

order of 10 to 100 ms [9]. SMAs can be activated by an external heat source or by electrical heating with an electrical current. For the latter, the energy consumption has to be carefully considered since most of the input energy is transformed to heat rather than mechanical strain, resulting in a low efficiency [14]. The transition temperatures of SMAs, between the martensite and austenite, phase depends largely on the type of alloy. For nitinol, the transition temperature is in between the −200 to 110 °C and can be adjusted by varying the proportions of nickel and titanium within the alloy [14].

Several studies focussed on the control of shape with shape memory alloys [20-22]. Barbarino *et al.* [23] conducted a numerical and experimental study with a shape memory alloy ribbon to control the shape of a wing structure to reduce its drag. The nickel-titanium-copper (NiTiCu) material was used where the martensite phase started at a temperature of 43 °C and an ended at a temperature of 27 °C. The austenite phase started at a temperature of 47 °C and ended at a temperature of 59 °C. A DC power source that generated 10 A at 1.5 V was used to activate the SMA element by Joule's heating. An experimental model was designed where an SMA ribbon created a bending motion to a panel, as illustrated by Figure 1.2. Each side of the SMA ribbon is bonded to a hinge, which in turn is bonded to the panel. The experimental results demonstrated displacement values of 4 mm generated by the SMA wire. However, Barbarino *et al.* [23] identified a drawback in the use of SMAs, which is the slow response time of the material. In the experimental test, the maximum displacement was reached four minutes after heating the SMA wire. As a possible solution, they proposed the use of complementary heat sources, i.e. exhaust gases to speed up the heating of the wire. However, their study did not make mention of functional testing at low temperatures, which is unusual since an aeroplane wing usually experiences sub-zero temperatures that would affect the SMA's response time. Barbarino *et al.* [23] also stated that a major drawback of SMAs is the difficulty of fully characterising their behaviour, which is highly nonlinear and load history dependent.

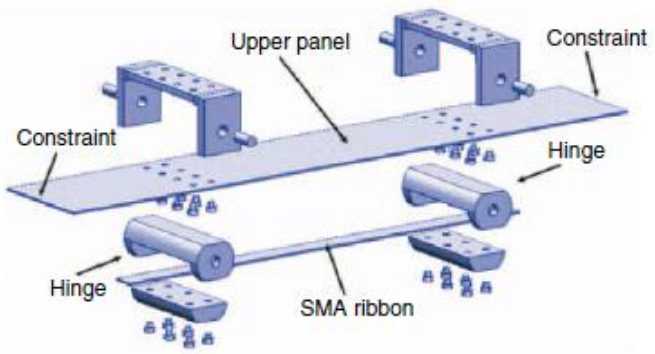

Figure 1.2 SMA-actuated bending device [23]

Another study, performed by Berton [5], researched and implemented a system made of push-pull SMA wires connected to mechanical links that actuate the trailing edge of a high altitude unmanned air vehicle. The motivation of the research was to reduce the wave drag in transonic cruise, which is achieved by modifying the shape of the trailing edge from a divergent one to a straight one. Many tests were conducted to evaluate the performance of the system and the SMA. The tests were conducted at room temperature and at a low temperature of −35 °C. The total cycle time for the trailing edge, to open and close, took around five minutes. This was measured at room temperature with 24 W of power applied to the SMA wires. The report did not specify the total cycle time at the low temperature, nor the amount of power applied to the SMA wires. However, Berton [5] does mention that the energy yield (electrical/mechanical) of the system is very low and below 1%. It was concluded that one of the limitations of SMA materials is the complexity in behaviour, especially under cyclic conditions.

The advantage of shape memory alloys is their ability to generate large displacements and, therefore, can be useful in morphing or shape control applications. However, their major drawback is the slow response time, which limits the range of application in which SMAs can be useful. Using shape memory alloys to control the shape of a structure that is subjected to high thermal loading is not suitable since the temperature radiated from the structure will affect the SMA material. Furthermore, it will be a big challenge to cool down the SMA material to its low temperature phase or martensite.

1.3.3 Magnetostrictive Materials

Magnetostriction is the change of the physical dimensions of a material in response to a change in the material's magnetisation. Therefore, a magnetostrictive material changes shape when it is subjected to a magnetic field. Magnetostrictive materials are materials that couple a magnetic field to a mechanical motion. The effect was first discovered in nickel by James Prescott Joule in 1842 [14]. However, the maximum strain of material was very low and reached only 0.005%. Later on, in the 1970s, a research group at the Naval Ordnance Laboratory discovered Terfenol-D, which produced a significantly larger strain of the order of 0.1 to 0.2%. Terfenol-D is one of the most commonly used materials since it presents the best compromise between a large magnetostrain and a low magnetic field at room temperature [24]. Magnetostrictive materials are useful for motion control applications and as elements of sensing systems for non-destructive damage evaluation [9]. The magnetic field is generated by a coil and a magnetic enclosure that is surrounding the magnetostrictive material. The magnetic field is altered by applying an AC current to the coil, which changes the strain respectively. A drawback of using a coil and a magnetic enclosure is the increase in weight of the actuator that can be ten times heavier in comparison to a piezoelectric stack actuator [24].

The density of Terfenol-D has a value between the 9150 to 9250 kg/m^3 [24, 25]. The elastic modulus of Terfenol-D strongly depends on the applied magnetic field and the compressive stress, and has been measured at values between 12 and 120 GPa [26]. The Curie temperature of Terfenol-D has a value of 380 °C [14, 25]. The stress generated by the material also depends on the applied magnetic field, compressive stress and elastic modulus, and is of the order of 22.8 [26] to 105 MPa [27]. Strains generated by magnetostrictive materials are equal to piezoelectric ceramics and of the order of 0.1 to 0.2%.

The use of magnetostrictive actuators in a helicopter blade trailing edge flap design was investigated by Fenn *et al.* [28]. In the analytical study, pairs of magnetostrictive Terfenol-D rods were mechanically linked to the trailing edge flap using a control rod. The study predicted that three pairs of magnetostrictive rods, driving four flaps per blade, would provide ±2° blade deflection, which was

necessary to reduce vibration in the helicopter. However, an experimental validation of the analysis was not carried out. Friedmann *et al.* [29] also studied the control flap actuation of a helicopter rotor. In this study, a minimum-mass magnetostrictive actuator was developed with a resulting mass of 630 g. It was shown that the magnetostrictive actuated flap was capable of producing vibration reduction in high-speed forward flight of 90%. Also in this study, no experimental validation was conducted.

The giant magnetostrictive actuator, developed by Zhang *et al.* [30] for active vibration control, displays promising results. The total output displacement obtained was $100E^{-6}$ m and an output force of 1500 N with a driving current of 1.2 A. The actuator was built around an $80E^{-3}$ m long Terfenol-D rod with a diameter of $7.2E^{-3}$ m. However, the study does not mention anything about the mass of the actuator.

The major drawback of magnetostrictive material is its weight and since its performance characteristics are almost identical to those of piezoelectric ceramic stack actuators, the latter is more commonly used in shape control applications because of its reduced weight advantage. Piezoelectric stack actuators are therefore more attractive because of their relatively low power consumption and high output energy per mass unit [14].

1.3.4 Piezoelectric Polymers

In the late 1960s, Kawai [31] discovered the strong piezoelectricity of the material polyvinylidene fluoride or PVDF, which is a piezoelectric polymer. Piezoelectric polymers belong to the class of electroactive polymers that exhibit electrostrictive behaviour. *Electrostrictive materials* are those that exhibit quadratic coupling between polarisation (or electrical field) and strain [9]. Piezoelectric polymers are softer materials compared to piezoelectric ceramics. Their elastic modulus is of the order of 1 to 3 GPa with a density of approximately 1000 to 3000 kg/m^3. The maximum strain produced by piezoelectric polymers is of the order of 0.1 to 0.2% that is manifested as either linear piezoelectric coupling or quadratic electrostrictive coupling and is almost identical to the strain generated by piezoelectric ceramics.

However, piezoelectric ceramics have much larger piezoelectric constants compared to piezoelectric polymers, which means that, in order to achieve the same amount of maximum strain, the electrical field applied to the piezoelectric polymers needs to be significantly higher. The stress produced by piezoelectric polymers is only 1/10 to 1/100 of the stress produced by a piezoelectric ceramic [9]. This is due to the low stiffness of the material limiting the material to applications with low force generation requirements [14]. Hence, the energy density of piezoelectric polymers is also smaller compared to piezoelectric ceramics and is between 50 to 500 J/m^3. The response time depends on the construction and type of material but is generally of the order of 5 to 30 ms. A major drawback of piezoelectric polymers, like PVDF, is the limited operating temperature with a lower limit of around −40 °C and a upper limit of 60 to 80 °C [14].

Chen *et al.* [13] investigated the development of PVDF-based piezoelectric polymer actuators for controlling the surface of a large lightweight membrane reflector. Flexible PVDF actuators with a thickness of $27E^{-6}$ m were attached to the back of the reflector. Chen *et al.* stated that PZT actuators were not applicable for this application at the time of the research. In order to create a bidirectional bending displacement, a three-layered actuator was proposed. The actuator consists of two electrostrictive layers that are actuated independently, which are bonded to a backing layer. However, it was found that the bending displacements in the two directions were not equal. The maximum allowable electrical field for the PVDF patch was 1620 V and the deformation of the reflector was measured when an electrical field of 800 V was applied. The study proves that it is possible to control the shape of a large lightweight reflector with the use of PVDF patches. The research did not study the effects of temperature on the properties of the actuator.

Advantages of the PVDF patches are their low mass, high flexibility and relatively low production costs. PVDF is available as thin sheets, which are easy to cut into different shapes. However, because of the low piezoelectric constant, the material requires a high electrical field to generate strains equal to those of piezoelectric ceramics. If shape control of a mobile structure, for example an aerospace vehicle is required, there is a possibility that the use of high voltage (greater than one kilovolt) power supplies may either not be compatible with existing

avionic systems, or not available on board of the vehicle. In addition, the limited range in operating temperature does not make piezoelectric polymer a suitable material for shape control of structures under thermal loading.

1.3.5 Smart Material Applied in this Research

Four groups of smart materials have been studied in Sections 1.3.1 – 1.3.4 and the advantages and disadvantages are identified. The performance properties and operating temperatures of each of the materials are compared, together with the potential capability to use the material as an actuator. An overview of the discussed smart materials is given by Table 1.2. Note that the values in this table are given in ranges, since the values strongly depend on a large number of factors, e.g. the applied field strength, the operating temperature or the composition of each material.

Shape memory alloys have the ability to generate large strains, however their response speed is slow and the generated strain is affected by the temperature. A drawback of magnetostrictive material is their large weight, which is caused by the coil and magnetic enclosure used to generate a displacement. Piezoelectric polymers have the ability to generate equal strain values as the piezoelectric ceramics. However, the generated stress by the piezoelectric polymers and energy density are relatively low.

	Piezoelectric ceramics	**Shape memory alloys**	**Magnetostrictive materials**	**Piezoelectric polymers**
Density [kg/m^3]	7000–8000	7000–8000	9150–9250	1000–3000
Elastic modulus [GPa]	10–100	10–100	12–120	1–3
Strain [%]	0.1	4–8	0.1–0.2	0.1–0.2
Stress [MPa]	1–50	5–50	22.8–105	0.1–1
Energy density [kJ/m^3]	10–100	5–500	10–100	0.05–0.5
Response speed [ms]	1	10–100	10	5–30
Operating temp. [°C]	200 to 1000	−200 to 1100	380	−40 to 80
Applied field	Electric	Thermal	Magnetic	Electric

Table 1.2 Overview of the smart materials discussed in the previous sections

It is determined that piezoelectric ceramics are the most suitable smart material for low weight, high temperature and high strain applications. Piezoelectric materials are widely and commercially available. A large amount of research has been conducted using these materials as ultrasonic transmitter and receiver transducers, for sonar applications and as actuators for precision positioning devices, and shape and vibration control. The material is controllable by a broad electrical field up to one thousand volts and has a high elastic modulus, which results in a large generation of force. The operating frequency of piezoelectric ceramics ranges from near static up to the kilohertz range. With Curie temperatures ranging from 380 to 1000 °C, this material is suitable for shape and vibration control in high temperature applications. The material exhibits small but precise strokes with nanometre resolution and has a fast response time. The actuation characteristic of piezoelectric ceramics is approximately linear with hysteretic behaviour.

The following section continues with the review of piezoelectric ceramics and their applications in shape control.

1.4 Shape Control Using Piezoelectric Actuators

Smart structures that incorporate integrated piezoelectric actuators and sensors offer potential benefits in a wide range of engineering applications such as structural health monitoring, vibration control, and shape control. Shape control involves activating the actuators that are either mounted to the structure or integrated in the structure, in order to eliminate external disturbances and to achieve a certain desired shape specified by the user. Disturbances that affect the shape of a structure can be subdivided into two areas [32]. One area is the *static shape control* and is associated with fixed deformations or those that are slowly varying over time. The second area is the *dynamic shape control*, which is associated with disturbances that are dynamic deformations. When the external disturbances as well as their effects upon the structural deformation are known in advance, the necessary control actuation may be estimated from an inverse structural analysis, which is called a *passive control strategy* [32]. When the external disturbances are not known in advance, but it is able to identify the disturbances by a sensor, an *active control strategy* can be utilised.

A large amount of research has been conducted in developing theoretical models to predict the shape of a smart structure, when the piezoelectric elements are activated. Two cases of static shape control using piezoelectric actuators were studied by Kokonis *et al*. [33, 34], which were *voltage specified* and *desired shape specified*. In the voltage specified case, Kokonis *et al.* developed an analytical method, which could be used to calculate the changes in shapes for specified voltages applied to the actuators. In the desired shape specified case, the voltages were determined to achieve a specified desired shape. The analytical methods developed in the research were validated by comparing them to other analytical and experimental results and agreed extremely well.

Thinh and Ngoc [35] developed a finite element model based on the first-order shear deformation theory (FSDT) for the static flexural shape and vibration control of a glass fibre and polyester composite plate bonded with piezoelectric patches. The finite element model was validated with an experiment that used a composite beam with two piezoelectric patches, bonded on the top and bottom side of the beam. One piezoelectric patch served as an actuator and the other as a sensor. The thickness of the composite beam was $1E^{-3}$ m and the thickness of each piezoelectric patch was $0.25E^{-3}$ m. An electrical field of 82 V was applied to the actuator. The experiment demonstrated that, with the proper piezoelectric actuators and voltage, it is feasible to generate enough force to control the shape of a laminated composite plate. However, since Thinh and Ngoc only used one piezoelectric patch as an actuator, it was only possible to control the shape of the beam in one direction.

Chandrashekhara and Varadarajan [36] studied the shape control of a laminated composite beam, with integrated piezoelectric actuators, and developed a mathematical model based on the higher order shear deformation theory. The optimal actuator voltages were calculated to minimise the error. The paper presented numerical results for open and closed loop shape control. In order to control the shape of the beam in both directions, the optimal voltages were calculated within the −200 to 200 V electrical field range. Ren [37] developed a theoretical model based on the Rayleigh-Ritz principle for the control of deformation of a thin arbitrary lay-up composite laminate with a piezoelectric actuator. In order to validate the theoretical model, it was compared with the results of a finite element analysis. In

this analysis, electrical fields of approximately −500 V and 500 V were applied to the piezoelectric element. Luo and Tong [38] presented a high precision control for the specified plate twisting and bending shapes using orthotropic piezoelectric actuators. In this study, a finite element model was derived and verified against the finite element simulation results of the commercial package NASTRAN. Optimal voltages were calculated using an optimisation algorithm. Voltages in the range of approximately −1000 to 600 V were calculated to obtain the desired shape. All three studies demonstrate that it is possible to develop a model and optimise the voltages to obtain a specified shape. However, it was not possible to find a practical validation of the concepts in the literature. In practise, it is unusual to operate piezoelectric material under large negative voltages, since the material is semi-bidirectional and permanent depolarisation occurs.

Piezoelectric elements are polarised, which means that the electrical field is usually applied in the polarisation direction that causes the element to expand. When a large electrical field is applied opposite to the polarisation direction, it is possible to depolarise the material. At room temperature, a negative electrical field up to 20% of the maximum driving voltage may be applied in order to achieve semi-bidirectional operation [18]. Piezoelectric materials operate in a *semi-bidirectional* manner, which means that the largest amount of displacement is typically generated in the extending direction and only a small amount in the contracting direction. The amount of negative electrical field that is applied to the piezoelectric element, without depolarising the material, depends on the type and temperature of the element. The stability of PZT ceramics against unwanted de-poling effects increases dramatically at low temperatures [18]. Only at *cryogenic temperatures* (<150 °C), is it possible to operate piezoelectric ceramics in bidirectional operation.

Researchers Song and Zhou *et al.* [7] took their study a step further and focussed on the thermal deformation compensation of a composite beam using piezoelectric actuators. The thermal deformation was induced by two heater patches that were surface-mounted to the top side of the beam, and the deformation was compensated by four PZT patches mounted to the bottom surface of the beam. A practical experiment was conducted to validate the model, where the developed proportional-integral-derivative (PID) controller supplied the appropriate electrical field to the

PZT patches. The results demonstrate that the PZT patches are able to compensate the shape of the composite beam. A similar study was conducted by Binette and Dano *et al.* [8] that investigated the shape control of a composite structure under thermal loading, using two Macro-Fiber Composite (MFC) actuators. The practical experiment demonstrated that the MFC actuators are able to compensate the deformed composite beam, when a large electrical field is applied to the actuators.

In both studies, the piezoelectric patches were bonded to one side of the beam, and therefore shape compensation only occurred in one direction. However, Ho and Paull [1] conducted a structural-thermal analysis of a combustor and intake of a M10 Generic HyShot Engine and demonstrated that the displacements of the structure are bidirectional, where some areas deform upwards and other downwards. Therefore, it is crucial to use an actuator that is able to compensate the shape of a structure in both directions. One solution could be to mount the piezoelectric actuators to both sides of the structure. A disadvantage of this solution would be that one piezoelectric actuator is bonded to the side of the structure that is heated, the hot side, and therefore directly subjected to the heat, which would result in a performance loss and reduced lifetime of the actuator [3, 4, 18].

Since piezoelectric elements experience a reduction in performance when directly subjected to thermal loading and exhibit only semi-bidirectional actuation at room temperature, this thesis continues focussing on bidirectional actuators that can be mounted to one side of the structure to compensate for deformation changes.

1.5 Compliant Mechanisms

A *compliant mechanism* is a mechanical device used to transfer or transform motion, force, or energy, gaining at least some of their mobility from the deflection of flexible members rather than from movable joints only [39]. Piezoelectric elements, combined with a compliant mechanism, have been implemented by several researchers to achieve bidirectional actuation [40-43] or an amplification in displacement [40, 42-49].

1.5.1 Bidirectional Compliant Mechanisms

Since piezoelectric elements exhibit semi-bidirectional operation, researchers have utilised compliant mechanisms to create actuators with bidirectional operation.

Bharti and Frecker [42] developed a compliant mechanism that is able to exhibit bi-directional actuation in order to stabilise a rifle. The compliant mechanism serves as an amplifier for the generated displacements of the piezoelectric stacks. Whereas certain studies [40, 41, 43] used a DC-bias to create equal bidirectional displacements, Bharti and Frecker used a large compressive preload on the piezoelectric stacks. The type of piezoelectric stack, used in their study, was a type PZ26 stack manufactured by Noliac that was operated under electrical fields in the range of −100 to 200 V. However, their experimental studies demonstrated that the free displacement at 200 V was seven times bigger than the free displacement at −100 V. Hence, Bharti and Frecker suspected that the prototype had insufficient compressive preload on the stack actuators.

Several other studies used a positive electrical field as a bias to achieve equal bidirectional displacements [40, 41, 43]. Mangeot and Andersen *et al*. [40] developed a bidirectional actuator, as reported in, which is illustrated by Figure 1.3. The actuator uses four piezoelectric stack elements connected in pairs and was operated using an electrical field in the range of 0 to 3000 V. The focus of their research was to increase the energy density and temperature stability of the actuator. The actuator exhibited displacements in the millimetre range and has a mass of 5800 g. Although the actuator demonstrates a large energy density, its drawbacks include the large operating voltage, the actuator's mass and the use of hinges, which results in an increase in wear. The report does not mention the amount of DC-bias applied to the actuator to create the bidirectional motion.

Ardelean *et al.* [43] developed a v-shaped compliant mechanism that leverages the displacements of two integrated piezoelectric stacks. With a DC-bias of 125 V as the null position, the actuator produced equal forces and displacements in both directions.

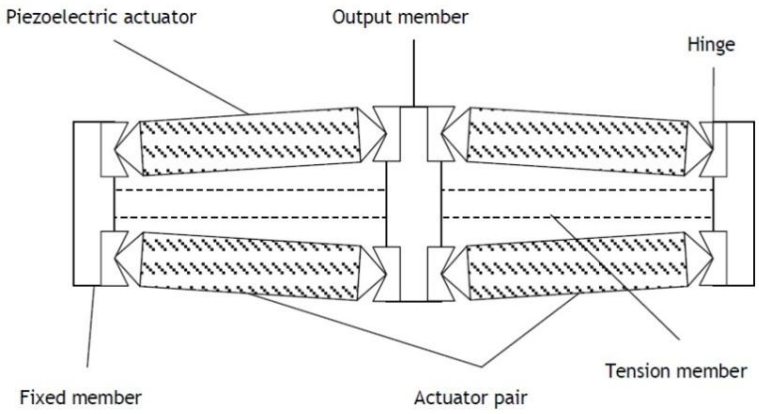

Figure 1.3 Diamond frame actuator employing four piezoelectric stacks [40]

However, the actuator generates leveraged displacements instead of pulling or pushing displacements. Another bidirectional actuator was developed by Heverly *et al.* [41] that incorporates two opposing piezoelectric stacks to generate pulling and pushing displacements. Identical bidirectional displacements were achieved by applying a DC-bias of 50 V to both stacks. The results of the analytical and experimental study demonstrate that the bidirectional actuator generates a push and pull displacement of approximately $9E^{-6}$ m and a force up to 350 N. However, more displacement is required in order to use this actuator for shape control of a structure subjected to thermal loading. One way to achieve this is to integrate the actuator in an amplification compliant mechanism.

1.5.2 Amplification Compliant Mechanisms

One of the limitations of piezoelectric actuation is that a single piezoelectric element produces displacements in the micrometre range. The need to increase the displacements generated by piezoelectric elements has led to the development of piezoelectric stack actuators. Piezoelectric stack actuators are capable of linear positioning with nanometre resolution, large blocking force, high stiffness, and rapid response characteristics. However, the generated stroke is minute, which typically accounts for 0.1% to 0.2% of the length of the piezoelectric stack. For applications that require a large stroke, amplifying compliant mechanisms are used to increase the

displacement.

Amplifying mechanisms for piezoelectric actuators can be broadly classified into four groups: directly amplified mechanisms, accumulating mechanisms, ultrasonic mechanisms, and pump actuator structures [48]. *Direct amplified mechanisms* include one or two-stage lever structures [50] and diamond or elliptical-shaped structures [51]. Diamond or elliptical-shaped structures use a hinge to lever the force and the movement of the piezoelectric stack to the output of the structure. Bender actuators are also directly amplified mechanisms and consist of two piezoelectric layers that produce a curvature when one layer expands while the other contracts. These transducers are also referred to as bimorphs or flexural elements. Bender motions of approximately hundreds to thousands of microns and bender forces of up to ten newton are typical. *Accumulating mechanisms,* like the self-moving cell linear motor [52], use the high frequency characteristics of piezoelectric material to generate very small steps into larger displacements. *Ultrasonic mechanisms* use the vibrations generated by the piezoelectric material. This technique is implemented in the deep hole drilling process by superimposing additional vibration energy in the ultrasonic frequency range by means of a piezoelectric transducer [53]. *Piezoelectric pump actuators* use a hydraulic fluid in a reservoir that is actuated by a piezoelectric actuator [54]. The hydraulic fluid drives a small piston cylinder that is hydraulically connected to a larger cylinder to produce the amplified displacement.

The most suitable amplifying mechanism to use, in combination with a bidirectional actuator, is the diamond or elliptical-shaped amplifier, since it is the simplest and most effective amplifier mechanism. This mechanism is able to amplify the actuator's stroke, which depends on the geometry, by approximately nine times [44, 48]. Several studies [40, 48, 49] and manufacturers [55, 56] have implemented this type of amplification mechanism to amplify the displacement generated by a piezoelectric stack. However, the operating mode of the amplified actuators developed to-date, and to the author's best knowledge, is semi-bidirectional and not fully bidirectional with equal displacements in both directions.

1.6 Aim of the Thesis

Motivated by the need for an actuator that is capable of operating in bidirectional mode, this thesis is devoted to the investigation and analysis of an amplified bidirectional actuator that has been developed with the primary purpose of minimising the deformation of a structure subjected to thermal loading.

Two amplified bidirectional actuators are proposed, analysed and discussed in this thesis. The first proposed actuator is the a*mplified dual-stack actuator* (ADSA), which combines the dual-stack actuator developed by Heverly *et al.* [41] with a diamond frame to amplify the displacement. The performance and capability of the ADSA, to be employed for shape control, is theoretically analysed and simulated using the finite element method (FEM) to identify the behaviour of the actuator. The second actuator proposed in this thesis is the *amplified bidirectional actuator* (ABA), which is an improvement with respect to the shortcomings of the ADSA and more suitable for shape control.

In order to identify the bidirectional compensation abilities of both actuators, a benchmark model is created containing a beam structure subjected to thermal loading that employs two piezoelectric patches, one on each side of the structure, to compensate for the thermally induced deformation. Two piezoelectric patches are employed in order to create a bidirectional actuation. Piezoelectric materials demonstrate semi-bidirectional actuation and generate the largest amount of displacement in the extending direction and only a small amount in the contracting direction. Therefore, to excite the beam structure in a bidirectional manner, it is essential to mount one piezoelectric patch on each side of the structure. The displacement data and compensation generated by the piezoelectric patches serve as a benchmark for the performance of the ADSA and ABA. Both actuators are separately mounted onto one side of identical structures.

1.7 Outline of the Thesis

This thesis presents the design and the FEM simulation results of an amplified bidirectional actuator, which has been developed to compensate the thermally

induced deformation of a structure. A detailed outline of the structure applied in this thesis is given below.

In Chapter 2, the constitutive equations and the relationship between the stress and the strain of piezoelectric material are discussed, to get a better understanding of the electromechanical coupling of piezoelectric material. The modelling techniques are then described to model piezoelectric elements in the finite element software tool ANSYS®.

Chapter 3 starts with a theoretical analysis of the amplification frame used to amplify the displacement generated by the actuator. A mathematical function is derived that calculates the amplification factor and amplified displacement. The chapter continues with a brief discussion about two conducted analyses of amplified bidirectional actuators and their shortcomings.

In Chapter 4, the ADSA is proposed. The dual-stack actuator developed by Heverly *et al.* [41] is first discussed and theoretically analysed. One of the piezoelectric stacks used in the dual-stack actuator is modelled in ANSYS and the displacement and blocked force results are verified against the manufacturer's specifications. The chapter continues by modelling the dual-stack actuator in ANSYS to identify its behaviour. According to the dimensions of the dual-stack actuator, a diamond-shaped amplifying compliant mechanism is developed and mounted to the actuator to amplify the displacements. The performance of the ADSA is then simulated. In order to compare the compensation performance of the ADSA, a benchmark model is built that contains a beam structure with two piezoelectric patches mounted to each side of the beam to compensate for the thermally induced deformation in both directions. This benchmark is almost identical to experiments conducted in other studies [7, 8]. The difference is the fact that the patches are mounted on each side of the beam structure to excite the beam in both directions. The ADSA is then mounted to an identical beam structure, as used in the benchmark, and the compensation performances of both models are compared. The discussion of the results leads to the development of a new bidirectional actuator, which is more suitable for shape control.

In Chapter 5, the novel amplified bidirectional actuator (ABA) is proposed. The chapter begins with a discussion of the shortcomings of the dual-stack actuator and

the ADSA and continues by describing the improved geometry of the ABA. A finite element model of the bidirectional actuator is generated and the behaviour is simulated in ANSYS. A diamond-shaped amplifying compliant structure is developed to amplify the displacements of the bidirectional actuator. A new finite element model of the ABA is then generated and the behaviour and performance is identified using ANSYS. Finally, the ABA is mounted to an identical beam structure as used in the benchmark model and the simulation results are compared against the results of the ADSA and the benchmark model.

In Chapter 6, a summary of the overall conclusions obtained from the research is presented and recommendations for further directions of the research are given.

1.8 Original Contributions to the Thesis

To the author's knowledge, the design and analysis of the amplified actuators that are able to generate equal positive and negative displacements, i.e. the ADSA (in Chapter 4), and the bidirectional actuator and ABA (in Chapter 5) as presented in this thesis, are original. More specifically, the original contributions are highlighted as follows:

1. A finite element model of the dual-stack actuator, developed in the study of Heverly *et al.* [41], is designed to thoroughly analyse and understand the behaviour of the actuator. An advantage of a finite element model is the relatively easy ability to change important design properties, such as the length of the piezoelectric stack, or the type of piezoelectric ceramic, to simulate and identify the new performance values of the actuator.

2. A new a*mplified dual-stack actuator* (ADSA), using the existing dual-stack actuator in combination with a diamond-shaped amplifying compliant structure, is proposed in Chapter 4. The dual-stack actuator is used in combination with a DC-bias to create equal bidirectional displacements, whereas the amplifying frame amplifies the generated displacements by the

actuator. Both the dual-stack actuator and the diamond-shaped compliant structure exist. However, the design is new in the sense that nobody has previously attempted to combine the dual-stack actuator with an amplifying compliant structure to obtain larger bidirectional displacements.

3. A novel *amplified bidirectional actuator* (ABA) is proposed in Chapter 5. This actuator is new in the sense that the geometry is optimised. Hence, the bidirectional actuator does not need a DC-bias to generate equal bidirectional displacements. Therefore, no initial displacement is generated, which makes the actuator more suitable for shape control applications. The ABA combines the improved bidirectional actuator, with a diamond-shaped amplifying compliant structure, to obtain larger displacements. The main advantage of the ABA, compared to the ADSA, is the lack of a DC-bias to create bidirectional displacements, which reduces the amount of energy dissipated by the actuator. Hence, the actuator is more suitable for shape control.

The outcomes of these three original contributions provide a basis for further research concerning the development and implementation of bidirectional actuators in the field of shape control.

Chapter 2

Finite Element Modelling of a Piezoelectric Stack Actuator

To get a better understanding of the electromechanical coupling properties of piezoelectric materials, this chapter begins by examining the constitutive equations, which define the coupling relationship between the different variables. The common operating modes and the relationship between force and displacement of piezoelectric actuators are discussed. The chapter then continues with a brief outline of the finite element analysis approach and techniques applied in this study to model piezoelectric material.

2.1 Electromechanical Coupling in Piezoelectric Actuators

Piezoelectric material exhibits electromechanical coupling and is therefore applied in a wide range of sensing and actuation devices. The coupling, known as the *direct effect,* is demonstrated by the fact that the material produces an electrical displacement when a mechanical stress is applied. The *electrical displacement* is defined as the produced charge divided by the area of the electrodes. The opposite effect, known as the *converse piezoelectric effect*, occurs when the material is subjected to an electrical field that causes the material to produce a mechanical strain.

2.1.1 Fundamental Equations for Piezoelectric Material

The basic properties of piezoelectric material are mathematically expressed as a relationship between the stress and strain, which are the two mechanical variables, and the electric field and electric displacement, which are the two electrical variables. The direct and converse piezoelectric effect can be mathematically combined in one matrix expression by writing the relationship between strain and electric displacement as a function of applied stress and electrical field [9]:

$$\begin{Bmatrix} S \\ D \end{Bmatrix} = \begin{bmatrix} s & d \\ d & \varepsilon \end{bmatrix} \begin{Bmatrix} T \\ E \end{Bmatrix}, \tag{2.1}$$

where

S = strain [m/m],
s = mechanical compliance [m^2/N],
d = piezoelectric strain coefficient [m/V],
T = stress [N/m^2],
D = electric displacement [C/m^2],
ε = dielectric permittivity [F/m],
E = electric field [V/m].

The top part of (2.1) represents the converse piezoelectric effect, whereas the bottom part of the equation represents the direct effect. An important parameter for comparing the strength of piezoelectric material is the piezoelectric strain coefficient. A larger piezoelectric strain coefficient results in a material that produces more strain for an applied electrical field and more electric displacement for an applied mechanical stress.

Rewriting the strain and the electric displacement from (2.1) into separate notations, the full constitutive equations for a linear piezoelectric material are defined as [57]:

$$S_{ij} = s_{ijkl}^{E} T_{kl} + d_{kij} E_k, \tag{2.2}$$

and

$$D_i = d_{ikl} T_{kl} + \varepsilon_{ik}^{T} E_k, \tag{2.3}$$

where the subscripts $i, j, k, l =$ 1,2,3 and refer to the coordinate axis of a Cartesian coordinate system. The complete set of constitutive equations is defined by eighty-one mechanical compliance constants, twenty-seven piezoelectric strain coefficient values, and nine dielectric permittivities. However, the equations can be written in a more compact form, since the stress and strain tensors are symmetric for piezoelectric materials. Therefore, (2.2) and (2.3) can be written into the form:

$$\begin{Bmatrix} S_1 \\ S_2 \\ S_3 \\ S_4 \\ S_5 \\ S_6 \end{Bmatrix} = \begin{bmatrix} s_{11} & s_{12} & s_{13} & s_{14} & s_{15} & s_{16} \\ s_{21} & s_{22} & s_{23} & s_{24} & s_{25} & s_{26} \\ s_{31} & s_{32} & s_{33} & s_{34} & s_{35} & s_{36} \\ s_{41} & s_{42} & s_{43} & s_{44} & s_{45} & s_{46} \\ s_{51} & s_{52} & s_{53} & s_{54} & s_{55} & s_{56} \\ s_{61} & s_{62} & s_{63} & s_{64} & s_{65} & s_{66} \end{bmatrix} \begin{Bmatrix} T_1 \\ T_2 \\ T_3 \\ T_4 \\ T_5 \\ T_6 \end{Bmatrix} + \begin{bmatrix} d_{11} & d_{21} & d_{31} \\ d_{12} & d_{22} & d_{32} \\ d_{13} & d_{23} & d_{33} \\ d_{14} & d_{24} & d_{34} \\ d_{15} & d_{25} & d_{35} \\ d_{16} & d_{26} & d_{36} \end{bmatrix} \begin{Bmatrix} E_1 \\ E_2 \\ E_3 \end{Bmatrix}, \tag{2.4}$$

$$\begin{Bmatrix} D_1 \\ D_2 \\ D_3 \end{Bmatrix} = \begin{bmatrix} d_{11} & d_{12} & d_{13} & d_{14} & d_{15} & d_{16} \\ d_{21} & d_{22} & d_{23} & d_{24} & d_{25} & d_{26} \\ d_{31} & d_{32} & d_{33} & d_{34} & d_{35} & d_{36} \end{bmatrix} \begin{Bmatrix} T_1 \\ T_2 \\ T_3 \\ T_4 \\ T_5 \\ T_6 \end{Bmatrix} + \begin{bmatrix} \varepsilon_{11} & \varepsilon_{12} & \varepsilon_{13} \\ \varepsilon_{21} & \varepsilon_{22} & \varepsilon_{23} \\ \varepsilon_{31} & \varepsilon_{32} & \varepsilon_{33} \end{bmatrix} \begin{Bmatrix} E_1 \\ E_2 \\ E_3 \end{Bmatrix}. \tag{2.5}$$

Equations (2.4) and (2.5) represent the constitutive relationship for a linear piezoelectric material. However, in the literature it is common to use the compact form of the constitutive equations as a matrix expression, represented by [9]:

$$\underline{S} = \boldsymbol{s}^{E} \underline{T} + \boldsymbol{d}' \underline{E}, \tag{2.6}$$

and

$$\underline{D} = \boldsymbol{d} \underline{T} + \boldsymbol{\varepsilon}^{T} \underline{E}, \tag{2.7}$$

where $\boldsymbol{s}^E$ is a 6×6 matrix of compliance coefficients evaluated at a constant electrical field, $\boldsymbol{d}$ is a 3×6 matrix of piezoelectric strain coefficients, where the prime in $\boldsymbol{d}'$ denotes a matrix transpose, and $\boldsymbol{\varepsilon}^T$ is a 3×3 matrix of dielectric permittivity values evaluated at a constant stress.

Since many piezoelectric materials are orthotropic materials with symmetry associated with the elastic, electrical, and electromechanical properties, the number of variables represented by (2.4) and (2.5), which specify the piezoelectric properties, reduce significantly. By applying the symmetry, (2.4) and (2.5) are modified to [9]:

$$\begin{Bmatrix} S_1 \\ S_2 \\ S_3 \\ S_4 \\ S_5 \\ S_6 \end{Bmatrix} = \begin{bmatrix} s_{11} & s_{12} & s_{13} & 0 & 0 & 0 \\ s_{21} & s_{22} & s_{23} & 0 & 0 & 0 \\ s_{31} & s_{32} & s_{33} & 0 & 0 & 0 \\ 0 & 0 & 0 & s_{44} & 0 & 0 \\ 0 & 0 & 0 & 0 & s_{55} & 0 \\ 0 & 0 & 0 & 0 & 0 & s_{66} \end{bmatrix} \begin{Bmatrix} T_1 \\ T_2 \\ T_3 \\ T_4 \\ T_5 \\ T_6 \end{Bmatrix} + \begin{bmatrix} 0 & 0 & d_{31} \\ 0 & 0 & d_{32} \\ 0 & 0 & d_{33} \\ 0 & d_{24} & 0 \\ d_{15} & 0 & 0 \\ 0 & 0 & 0 \end{bmatrix} \begin{Bmatrix} E_1 \\ E_2 \\ E_3 \end{Bmatrix}, \tag{2.8}$$

$$\begin{Bmatrix} D_1 \\ D_2 \\ D_3 \end{Bmatrix} = \begin{bmatrix} 0 & 0 & 0 & 0 & d_{15} & 0 \\ 0 & 0 & 0 & d_{24} & 0 & 0 \\ d_{31} & d_{32} & d_{33} & 0 & 0 & 0 \end{bmatrix} \begin{Bmatrix} T_1 \\ T_2 \\ T_3 \\ T_4 \\ T_5 \\ T_6 \end{Bmatrix} + \begin{bmatrix} \varepsilon_{11} & 0 & 0 \\ 0 & \varepsilon_{22} & 0 \\ 0 & 0 & \varepsilon_{33} \end{bmatrix} \begin{Bmatrix} E_1 \\ E_2 \\ E_3 \end{Bmatrix}. \tag{2.9}$$

2.1.2 Characterisation of a Piezoelectric Actuator

A common operation mode of a piezoelectric actuator is the direction along the axis of polarisation, which is called the 33-*operating mode*. In the literature, the convention with piezoelectric material is to align the 3-axis of the material in the polarisation direction, as illustrated in Figure 2.1, so that the 1 and 2-directions are in the plane of the actuator.

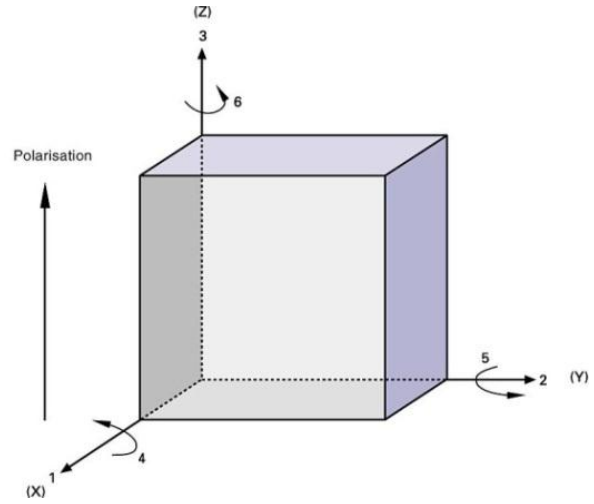

Figure 2.1 Orthogonal coordinate system of piezoelectric material [58]

When the assumptions are made that the nonzero stress and electric field are only in the 3-direction, (2.8) and (2.9) are reduced to [9]:

$$S_1 = -\frac{v_{13}}{Y_1^E} T_3 + d_{13} E_3 \,, \tag{2.10}$$

$$S_2 = -\frac{v_{23}}{Y_1^E} T_3 + d_{23} E_3 \,, \tag{2.11}$$

$$S_3 = \frac{1}{Y_3^E} T_3 + d_{33} E_3 \,, \tag{2.12}$$

$$D_3 = d_{33} T_3 + \varepsilon_{33}^T E_3 \,, \tag{2.13}$$

where $Y_i^E, i = 1, 2$ and 3 are the short-circuit elastic moduli in the 1, 2 and 3-directions, v_{ij} is the Poisson's ratio of the transverse strain in the j direction to the axial strain in the i direction when stressed in the i direction, and G_{23}^E, G_{13}^E, and G_{12}^E are the short-circuit shear moduli.

Equations (2.10), (2.11), (2.12), and (2.13) define the state of strain and electric displacement in piezoelectric material as a function of the stress and electric field. In the case of a piezoelectric actuator operating in 33-mode, the direction of interest of the piezoelectric material is the 3-direction. Therefore, the electrical and mechanical boundary conditions, S_3 and D_3, are specified and solved for the stress and electrical

field values, or the stress and electric field are specified and solved for the strain and electric displacement.

Two important design parameters for a piezoelectric actuator in the 33-operating mode are the blocked stress and the free strain, which are defined as [9]:

$$T_{3|S_3=0} = -Y_3^E d_{33} E_3 \tag{2.14}$$

and

$$S_{1|T_3=0} = d_{13} E_3 \,, \tag{2.15}$$

$$S_{2|T_3=0} = d_{23} E_3 \,, \tag{2.16}$$

$$S_{3|T_3=0} = d_{33} E_3 \,. \tag{2.17}$$

Equation (2.14) represents the *blocked stress*, which is defined as the stress produced by the actuator when the strain is constrained to be zero. Whereas (2.15), (2.16) and (2.17) represent the *free strain*, which is defined as the strain produced by the actuator when there is no stress applied to the material.

The relationship between the stress that is produced by a piezoelectric actuator as a function of the strain and applied electric field is illustrated in Figure 2.2. The point where the line intercepts the Y-axis, i.e. where the strain is zero, is the blocked stress of the actuator for a given electrical field. The point where the line intercepts the X-axis, i.e. where the stress is zero, is the free strain of the actuator for a given electrical field. These values are, therefore, the maximum achievable values that the actuator is able to generate at a given electrical field. Figure 2.2 also illustrates the relationship between the applied electrical field and the generated stress and strain curves. An increase of the applied electrical field results in an increase in the blocked stress and free strain. The slope of the lines plotted in Figure 2.2 is identical to the short-circuit elastic modulus Y_3^E.

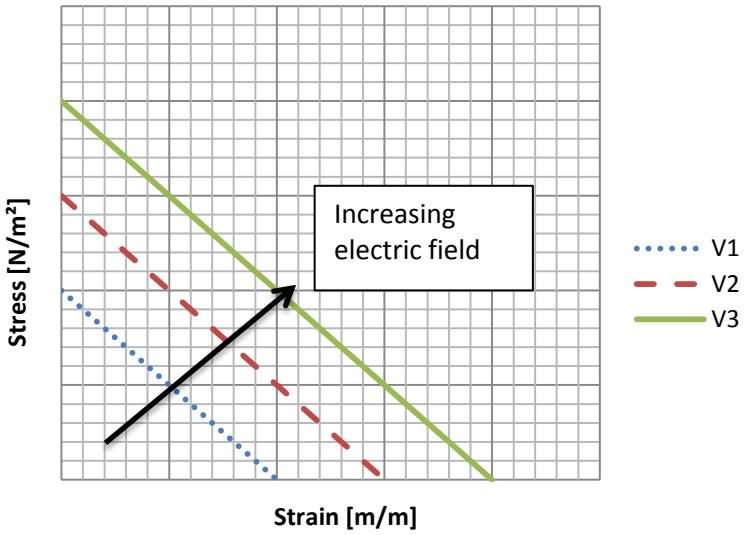

Figure 2.2 Stress vs. strain relationship of piezoelectric material

Equations (2.2) and (2.3) define the constitutive relationship of piezoelectric actuators using stress and strain, which are properties that do not depend on the geometry, the so called *intrinsic properties*. However, when designing a piezoelectric actuator, it is convenient to use equations that directly relate the force and displacement relationships. Therefore, the assumptions are made that the strain in the 3-direction, the stress, electric field, and the electrode surfaces are uniform. Applying these assumptions to (2.2) and (2.3) yields:

$$\frac{u_3}{t_p} = \frac{1}{Y_3^E}\frac{f}{A_p} + d_{33}\frac{v}{t_p}, \tag{2.18}$$

and

$$\frac{q}{A_p} = d_{33}f + \varepsilon_{33}^T\frac{v}{t_p}, \tag{2.19}$$

where u_3 represents the displacement in the 3-direction, t_p the thickness of the piezoelectric element, f the force, A_p the area of the piezoelectric element, v the applied potential, and q represents the charge. Solving (2.18) for u_3, and (2.19) for q gives:

$$u_3 = \frac{t_p}{Y_3^E A_p} f + d_{33} v \,, \tag{2.20}$$

and

$$q = d_{33} f + \frac{\varepsilon_{33}^T A_p}{t_p}\, v \,. \tag{2.21}$$

Equation (2.20) illustrates that the *free displacement*, when force f applied to the actuator is zero, equals:

$$\delta_0 = u_{3|f=0} = d_{33} v \,. \tag{2.22}$$

Deriving the *blocked force* from (2.20), where the displacement is constrained to be zero, gives:

$$f_{bl} = -f|_{u_3=0} = d_{33} Y_3^E \frac{A_p}{t_p} v \,. \tag{2.23}$$

2.1.3 Piezoelectric Stack Actuator

The generated strain of a piezoelectric element operating in the 33-mode is very limited and approximately 0.1 to 0.2%. Therefore, the need for larger displacement values generated by a piezoelectric actuator has led to the development of piezoelectric stack actuators. A *piezoelectric stack actuator* is an actuator that consists of piezoelectric elements stacked on top of each other. An electrode is placed in between the separate layers to provide an electrical field to each element. Since the elements are stacked, ideally the total displacement of the stack is equal to the sum of the displacement of each element. The blocked force, however, is not amplified and ideally is identical to the blocked force generated by a single element. Therefore, a piezoelectric stack actuator is capable of generating a large displacement compared to a single piezoelectric element, without a reduction of the force.

The relationship between the displacement u_{stack} and the number of elements n, in a stack actuator, is equal to the sum of each individual element. Assuming that each element in the stack is identical and the mechanical and electrical properties of the electrodes and bonding layers are negligible, the displacement is represented by [9]:

$$u_{stack} = nu_3 = \frac{nt_p}{Y_3^E A_p} f + nd_{33} v \,. \tag{2.24}$$

The total length of the stack actuator is equal to the number of elements multiplied by the thickness of the element, $L_{stack} = nt_p$, therefore (2.24) becomes:

$$u_{stack} = \frac{L_{stack}}{Y_3^E A_p} f + \frac{d_{33} L_{stack}}{t_p} v \,. \tag{2.25}$$

It is possible to derive the blocked force and free displacement of a stack actuator from (2.25), which are very useful parameters when designing a piezoelectric stack for a certain application. In order to derive the free displacement, the applied force to the stack is constrained to zero, which eliminates the coefficient in front of the addition sign and is represented by:

$$\delta_0 = u_{stack|f=0} = \frac{d_{33} L_{stack}}{t_p} v \,. \tag{2.26}$$

The blocked force generated by a stack actuator is derived by constraining the displacement to zero and is represented by:

$$f_{bl} = -f|_{u_3=0} = d_{33} Y_3^E \frac{A_p}{t_p} v \,, \tag{2.27}$$

and in an ideal situation, taking the assumptions into account, is equal to the blocked force generated by a single element.

Equations (2.26) and (2.27) demonstrate that the blocked force is equal to the amount of force generated by the piezoelectric stack when the displacement is constrained to zero. The free displacement is the amount of displacement generated by the stack when there is zero force applied to the stack. Determining the working point of the piezoelectric stack actuator is always a trade-off between the generated force and displacement. Amongst the blocked force and the free displacement, the piezoelectric stack has three operating regions. In order to identify these regions, the displacement, blocked force and energy transfer of a piezoelectric stack working against an elastic load is analysed. Consider a piezoelectric stack actuator that is modelled as a generated force f and the short-circuit stiffness k_s^E, working against a load k_l, and creating a displacement u, as illustrated in Figure 2.3. To facilitate the analysis, (2.25) is modified in the form:

$$u = \frac{1}{k_s^E} f + \delta_0 \,, \tag{2.28}$$

where $k_s^E = Y_3^E A / L_{stack}$, and u represents the generated displacement.

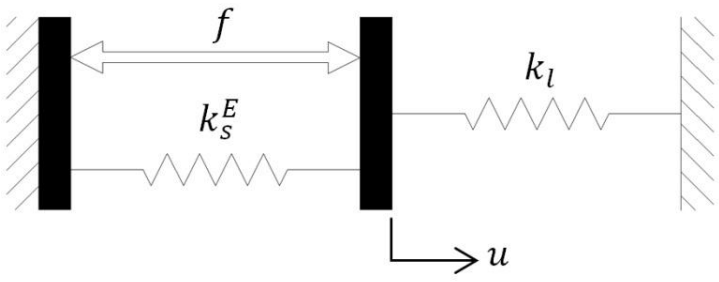

Figure 2.3 Schematic diagram of a piezoelectric stack actuator driving an elastic load

For the situation illustrated in Figure 2.3, the force generated by the actuator is represented by $f = -k_l u$. Substituting this expression into (2.28) and solving it for the displacement as a function of the stiffness provides:

$$\frac{u}{\delta_0} = 1 + \frac{k_l}{k_s^E}. \tag{2.29}$$

Analysing (2.29) and assuming that the stiffness of the actuator is much larger than the stiffness of the load, $k_s^E \gg k_l$, results in a generated displacement that is nearly identical to the free displacement. When the stiffness of the actuator is much smaller than the stiffness of the load, $k_s^E \ll k_l$, results in a displacement much smaller than the free displacement. A plot of this function is represented by the dotted blue line, illustrated in Figure 2.4.

Solving the blocked force from (2.28), by rewriting the force f as a function of the displacement u that is constrained to zero, gives:

$$f_{bl} = k_s^E \delta_0 . \tag{2.30}$$

The force generated by the actuator is represented by the expression $f = -k_l u$. Solving the ratio of force to the blocked force gives:

$$\frac{f}{f_{bl}} = \frac{k_l \delta_0 / (1 + \frac{k_l}{k_s^E})}{k_s^E \delta_0} = \frac{\frac{k_l}{k_s^E}}{1 + \frac{k_l}{k_s^E}}. \tag{2.31}$$

A plot of (2.31), where the output force of the actuator is normalised with respect to the blocked force, is represented by the dashed red line illustrated in Figure 2.4. When the actuator is working against a very soft load, such that the stiffness of the actuator is much larger than the stiffness of the load, $k_s^E \gg k_l$, the generated force is very low compared to the blocked force. When the actuator is working against a very stiff load, such that the stiffness of the actuator is much less than the stiffness of the load, $k_s^E \ll k_l$, the generated force is approximately identical to the blocked force.

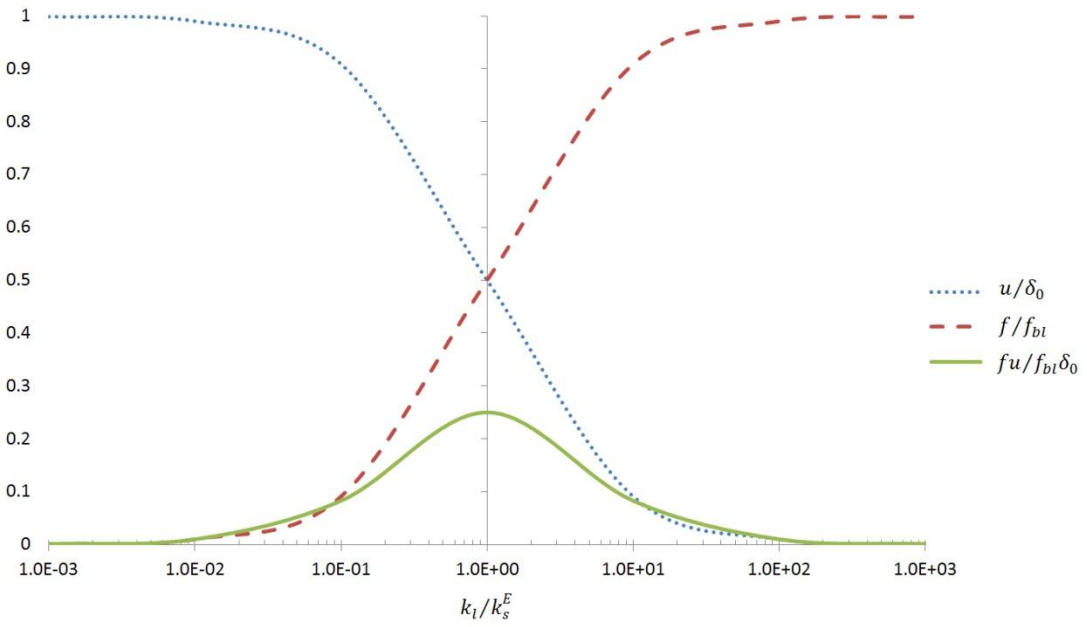

Figure 2.4 Behaviour of a piezoelectric stack actuator driving an elastic load, where $\boldsymbol{u/\delta_0}$ represents the normalised displacement with respect to the free displacement, $\boldsymbol{f/f_{bl}}$ represents the normalised force with respect to the blocked force and $\boldsymbol{fu/f_{bl}\delta_0}$ represents the output work normalised to the maximum work

The final parameter analysed is the output work. The *output work* of a piezoelectric stack is defined as the product of the force and the displacement and is represented by $W = fu$. The *maximum output work* of a piezoelectric actuator is defined as the blocked force multiplied by the free displacement. The relationship between the normalised output work with respect to the maximum output work is represented by (2.32):

$$\frac{fu}{f_{bl}\delta_0} = \frac{\frac{k_l}{k_s^E}}{1+\frac{k_l}{k_s^E}} \times\ 1+\frac{k_l}{k_s^E}. \tag{2.32}$$

Simplifying (2.32) gives:

$$\frac{fu}{f_{bl}\delta_0} = \frac{\frac{k_l}{k_s^E}}{\left(1+\frac{k_l}{k_s^E}\right)^2} \quad . \tag{2.33}$$

A plot of (2.33), where the output work is normalised with respect to the maximum output work, is represented by the solid green line in Figure 2.4. The maximum output work occurs when the stiffness of the actuator is equal to the stiffness of the load and is equivalent to a quarter of the product of the free displacement and the blocked force.

Figure 2.4 illustrates the three regions of operation for a piezoelectric stack actuator. The first operating region is where the stiffness of the actuator is much larger than the stiffness of the load, $k_s^E \gg k_l$, and is illustrated at the left side of the Y-axis in Figure 2.4. In this region, the motion of the actuator is not affected by the load and the actuator is able to generate a large amount of displacement, thus very little load transfer occurs. An application for an actuator that operates in this region, is generally in motion control to achieve maximum displacement of the load. The second region of interest is where the stiffness of the actuator equals the stiffness of the load, $k_s^E = k_l$. In the literature, this is sometimes referred to as *stiffness match point*, since both the stiffness of the actuator and the load are matching. This region is located directly on the Y-axis as illustrated by Figure 2.4. At this point, maximum load transfer occurs between the piezoelectric stack actuator and the load. The last operating region is where the stiffness of the load is much larger than the stiffness of the actuator, $k_s^E \ll k_l$. This region is illustrated by Figure 2.4 at the right side of the Y-axis. The load transfer in this region, between the actuator and the load, is very little. Piezoelectric stack actuators operating in this region are usually used as sensors since the actuator generates almost zero displacement. Hence, the load is not affected by the presence of the actuator.

When a structure is subjected to a thermal load, high internal stresses are generated that result in deformation of the structure. Therefore, using the results of the theoretical analysis that identify the different operating regions of a piezoelectric stack actuator, as illustrated by Figure 2.4, it is necessary for the actuator to be

operating in the left to middle region of the graph where $1E^{-1} < k_l/k_s^E < 1E^0$. Hence, the stiffness of the actuator has to be larger or identical to the stiffness of the structure. This ensures that the actuator generates enough displacement and force to exhibit optimal compensation.

2.2 Finite Element Analysis of Piezoelectric Material

This section presents a review of the analysis techniques used to create a finite element model that couples the structural, thermal and electrical fields. The finite element models designed for this study are generated and simulated using the commercial software package ANSYS®, version 12.1. Two analysing methods are discussed, followed by a brief discussion about the two types of elements and contact algorithm used in the analyses. This section continues describing the two applied methods to acquire the free displacement and blocked force values from the FEM-computed results.

2.2.1 Coupled-Field Analysis

A *coupled-field analysis* is an analysis that models the interaction (coupling) between two or more engineering disciplines (fields). For example, a structural-thermal analysis models the interaction between the structural and thermal fields by solving the displacement of a structure that is subjected to a heat flux. Other examples of coupled-fields are *piezoresistive*, *electroelastic*, *piezoelectric* and *thermal-piezoelectric*.

The procedure for a coupled-field analysis depends on which fields are being coupled. However, two distinct methods can be identified: the load transfer method and the direct method [59]. The *load transfer method* involves two or more analyses, each belonging to a different field. The fields are coupled by sequentially applying the solution results from one analysis as loads in the other analysis. The *direct method*, on the other hand, involves only one analysis that uses a coupled-field element type, which contains all the necessary degrees of freedom to solve the model. The coupling is handled by calculating the element matrices, or load vectors,

that contain all the essential terms. The load transfer method is recommended by ANSYS for structural-thermal analyses. However, the model used in this study couples three fields: structural, thermal, and piezoelectric respectively. Therefore, all analyses conducted in this study employ the direct method.

A coupled-field analysis model can be generated using three-dimensional (3-D), two-dimensional (2-D), or one-dimensional (1-D) elements. The 3-D solid element is considered the most general of all solid elements, since all the field variables are dependent on the X, Y and Z-axis [60]. The element can have any arbitrary shape, material properties, and boundary conditions in a defined space. It is possible to model almost every structure, including beam, shell and truss structures using a 3-D solid. However, a 3-D solid element is not always the best option, since creating the geometry and meshing the model can be very time consuming. Using 3-D elements also increases the amount of computation time and resources. Therefore, it is recommended to use 1-D or 2-D elements when a structure exhibits any symmetry or when it is possible to model the behaviour in two-dimensions. Furthermore, the model can become more efficient and accurate, since it is possible to increase the mesh density without using too many computational resources. In this study, 2-D elements are used when the structures incorporate any axisymmetric properties; otherwise, the model is generated using 3-D elements.

In order to do a coupled-field analysis in ANSYS, *multidisciplinary element types* are developed by ANSYS to capture the effects that relate to two different disciplines. Six different element types are available in ANSYS in order to perform a piezoelectric analysis. PLANE13, SOLID5, and SOLID98 are the legacy element types. However, as technology advances, new element types are developed and ANSYS recommends using the current technology elements rather than the legacy elements, since the current element types, PLANE223, SOLID226 and SOLID227, use more advanced techniques and are more feature-rich [59].

One of the element types used in this study is the element PLANE223 that occupies the 2-D space. The element consists of eight nodes with up to four degrees of freedom (DOF) per node, namely, structural (UX and UY), thermal and electric. The geometry, node locations, and coordinate system for this element type are illustrated by Figure 2.5. The finite element models designed in this study that

occupy the 2-D space, are generated with quadrilateral-shaped PLANE223 elements. There is also an option to use triangle-shaped elements by defining node K, L and O in the same location, as illustrated by Figure 2.5. The discipline of the element is set with the KEYOPT(1) option, the values of which are described in Table 2.1. Note that the PLANE223 element uses four degrees of freedom and, therefore, the displacement in the Z-direction (UZ) is not simulated.

The element type used in this study to perform an analysis in the 3-D space is the type SOLID226. The element contains 20 nodes with up to five degrees of freedom per node. Each node exhibits a displacement in three directions along the X, Y and Z-axis. The models designed for this study use either hexahedral or tetrahedral- shaped elements, which are illustrated by Figure 2.6. The discipline is set with KEYOPT(1) which values are described in Table 2.1. It should be noted that UX, UY, and UZ are to indicate the displacements in the X, Y and Z-directions, which are based on the global coordinate system in ANSYS.

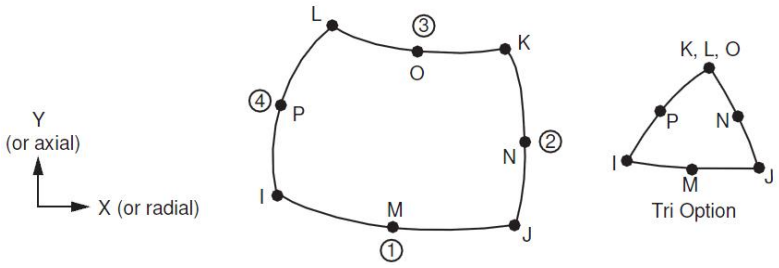

Figure 2.5 ANSYS element type PLANE223 [61]

Discipline	KEYOPT(1)	Degrees of Freedom
Structural-Thermal	11	UX, UY, TEMP
Piezoresistive	101	UX, UY, VOLT
Electroelastic	1001	UX, UY, VOLT
Piezoelectric	1001	UX, UY, VOLT
Thermal-Electric	110	TEMP, VOLT
Structural-Thermoelectric	111	UX, UY, (UZ), TEMP, VOLT
Thermal-Piezoelectric	1011	UX, UY, (UZ), TEMP, VOLT

Table 2.1 PLANE223 and SOLID226 KEYOPT(1) options

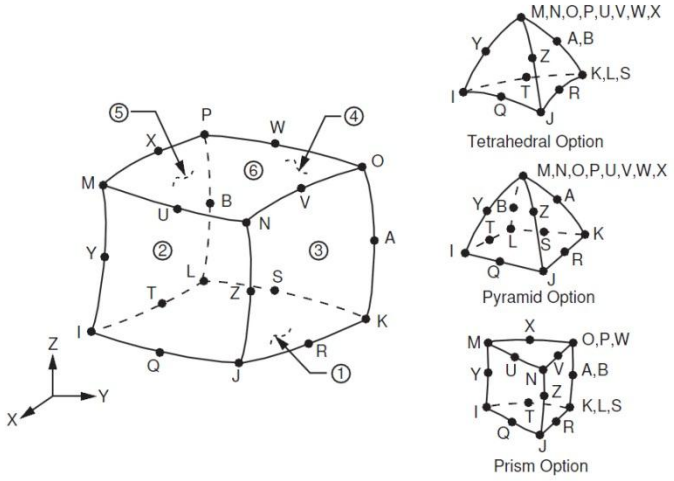

Figure 2.6 ANSYS element type SOLID226 [61]

2.2.2 Piezoelectric Material Data

ANSYS requires three types of data in order to perform a piezoelectric analysis. The stiffness matrix, also named the compliance matrix, represents the mechanical discipline. The permittivity at constant strain represents the electrical discipline, whereas the piezoelectric stress matrix represents the coupling between the mechanical and electrical disciplines. Units for the terms in the stiffness matrix $\boldsymbol{c}$ are typically N/m^2. The material data is entered in a 6 × 6 symmetric matrix for a 3-D element and a matrix of 4 × 4 is used for a 2-D element. The dielectric permittivity matrix $\boldsymbol{\varepsilon}$ defines the electrical permittivity measured at constant strain in typical units of F/m. The diagonal matrix is 3 × 3 in size and the permittivity can be specified as an orthotropic material property with the labels, PERX, PERY and PERZ, or as an anisotropic material property using the permittivity matrix. The piezoelectric stress matrix $\boldsymbol{e}$, relates the electric field to stress and typically has units of C/m^2. This matrix is 6 × 3 in size for a 3-D element and 4 × 2 in size for a 2-D element.

Comparing the material data that ANSYS requires with the available data described in the literature and provided by the manufacturers, several differences can be identified, as illustrated in Table 2.2.

ANSYS	Unit	Literature	Unit
Stiffness matrix $\boldsymbol{c}^E$	N/m^2	Compliance matrix $\boldsymbol{s}^E$	m^2/N
Permittivity at constant strain $\boldsymbol{\varepsilon}^S$	F/m	Permittivity at constant stress $\boldsymbol{\varepsilon}^T$	F/m
Piezoelectric stress matrix $\boldsymbol{e}$	C/m^2	Piezoelectric strain matrix $\boldsymbol{d}$	C/N

Table 2.2 Comparison of piezoelectric material data between ANSYS and literature

In the literature, the coupling relationship of piezoelectric material is represented by the constitutive matrix (2.6) and (2.7), whereas ANSYS requires the data in the form [62]:

$$\underline{T} = \boldsymbol{c}^E \underline{S} + \boldsymbol{e}\underline{E}\,, \tag{2.34}$$

and

$$\underline{D} = \boldsymbol{e}'\underline{S} + \boldsymbol{\varepsilon}^S \underline{E}\,, \tag{2.35}$$

where $\underline{T}$ represents the stress vector, $\underline{S}$ the elastic strain vector, $\underline{E}$ the electric field intensity vector and $\underline{D}$ represents the electric flux density vector. In the ANSYS 12.1 version, used in this research, it is possible to enter both forms of piezoelectric data, given that the appropriate type of data input is set with the element option switch, TBOPT. When the data is entered in the form described by (2.6) and (2.7), ANSYS automatically converts the data to the form represented by (2.34) and (2.35).

The location of the values in the compliance matrix and permittivity matrix depend on the polarisation direction of the piezoelectric material. By default, the polarisation direction is the 3-direction, or the Z-axis, which means that the piezoelectric element is designed in ANSYS accordingly. However, on some occasions, for example a 2-D axisymmetric analysis, it is convenient to have the polarisation direction in the Y-axis. In this situation, the matrixes are manipulated to represent the piezoelectric material with a poling direction in the 2-direction. Another matrix manipulation that is required for a piezoelectric analysis in ANSYS, is that the row data for the shear terms need to be switched [59].

Pigache developed and integrated all these conversions into an Excel worksheet, so that the manufacturers' piezoelectric data is converted to the appropriate ANSYS

data [63]. The matrix transformations are validated by Pigache, using a bimorph bender in elongation mode.

When conducting a piezoelectric analysis using ANSYS, all the coupled-field elements, regardless of whether they have structural, thermal or electric degrees of freedom, must be of piezoelectric type [59]. Very small piezoelectric coefficients can be specified for non-piezoelectric elements. Therefore, all materials used in this research must have a piezoelectric matrix, which are specified in Appendix A.

Figure 2.7 illustrates the stacking order of the piezoelectric elements to create a stack actuator. The figure illustrates that the stack consists of elements with two different polarisation directions. It is essential that all piezoelectric elements expand when a positive electrical field is applied to the electrodes. If all piezoelectric elements connected electrically in Figure 2.7 are arranged along the same polarisation direction, the stack will not show any displacement, since one piezoelectric element will expand while the other contracts. In order to simulate a piezoelectric stack actuator in ANSYS, the piezoelectric elements must be assembled in such way that each adjacent pair has opposite polarity. To achieve this, two material types must be defined in ANSYS, where one material has the opposite sign to the other's for the values of the piezoelectric matrix. The stiffness matrix and dielectric matrix are identical for the two materials [64]. The piezoelectric material types, defined for the analysis in this thesis, are described in Appendix A. All piezoelectric elements illustrated in Figure 2.7 with the arrow of the polarisation direction pointing upwards must be meshed with material one, whereas the elements with the arrow of polarisation pointing downwards must be meshed with material two, or vice versa.

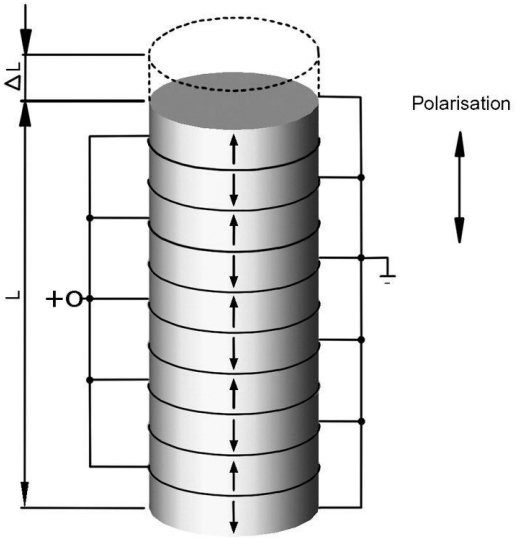

Figure 2.7 Piezoelectric elements in stack configuration [65]

2.2.3 Contact Algorithms

When a model consists of two separate geometries that must be in contact with each other, certain options are available to bond the geometries together to model their interaction. The two separate geometries can be glued together, executing the VGLUE or AGLUE command, and meshed with a consistent mesh, whereas another solution is the use of a contact algorithm. Once a model becomes more complex, i.e. using more than two different geometries that are in contact with each other, it is a challenging task to mesh all geometry parts with a consistent mesh. Therefore, the finite element models, proposed in this study, use the Multipoint Constraint (MPC) contact algorithm to bond different materials and structures with one another. ANSYS automatically generates the MPC equations once the contact and target surfaces are generated. The contact algorithms are generated using the *contact manager* in ANSYS. After the contact pair is generated, the command CNCHECK ADJUST is executed to move the contact nodes to the target nodes to close any initial gaps or reduce penetration. This produces the most accurate solutions and is always recommended for bonded contacts [66].

2.2.4 Applied Method to Simulate and Obtain the Free Displacement

Before solving the free displacement of the actuators described in this thesis, certain constraints must be applied to the model for the solution to converge. In the case of the free displacement, one side of the actuator is constrained in all directions and the model is solved.

After solving the model, the displacement at the point of interest is acquired by using surface operations. The surface is created by aligning the XY-plane of the working plane with the point of interest. The command SUCR is then executed to generate the surface. The advantage of surface operations is that ANSYS isolates the surface from the rest of the model, which makes it possible to map specific solution results onto the surface, instead of the whole model. The X, Y or Z-component of displacement is then mapped on the surface by executing the SUMAP command. In order to generate one average value, the command SUEVAL is used to calculate the average of the set of displacement values of the surface. All displacement values generated by the actuators described in this study are acquired using the above method.

2.2.5 Applied Method to Simulate and Obtain the Blocked Force

There are several methods to simulate and identify the blocked force value of an actuator. However, before the model is solved, it must be constrained for the solution to converge. Therefore, one side of the model is constrained in all directions.

ANSYS treats the relationship between the blocked force and free displacement as linear, as illustrated by Figure 2.2. The blocked force is simulated by applying a load of increasing magnitude to the actuator. For each applied load, the model is solved for the displacement. The load is increased in magnitude until the displacement of the actuator reaches its neutral point, which is the point where the line intersects the Y-axis in Figure 2.2. The data points are plotted in a graph similar to Figure 2.2, with the displacement on the X-axis and the force on the Y-axis. The least-squares regression method is then used as a linear fit. Using this method, not only is the blocked force identified, but also the force versus displacement relationship of the actuator. Therefore, the displacement is identified for any load

applied to the output of the actuator. All blocked force values generated by the actuators, described in this study are acquired using this method.

Chapter 3

Amplified Bidirectional Structures

In this chapter, the piezoelectric stack actuator, discussed in Section 2.1.3, is combined with a diamond-shaped compliant mechanism in order to amplify the generated displacement of the stack. Piezoelectric stack actuators are capable of generating large forces, but relatively small displacement values. Hence, the amplified actuator exhibits a larger displacement and a reduced blocked force. This chapter begins with an introduction and analysis of a diamond-shaped amplifying mechanism. The relationship between the dimensions of the structure and the amplification factor is studied. The chapter continues with a brief discussion of two preliminary finite element analyses studies of amplified bidirectional structures, which are conducted with the aim of identifying the behaviour and displacement values of the compliant mechanism with different stack configurations. Both structures incorporate three piezoelectric stack actuators, in different configurations, to achieve the desired bidirectional actuation.

3.1 Analysis of a Diamond-shaped Compliant Mechanism

Piezoelectric stack actuators are capable of linear positioning with nanometre resolution, large blocking force, high stiffness and rapid response characteristics [9]. However, a major drawback of PZT material arises from its small travel stroke,

which typically amounts to 0.1 to 0.2% of the length of the piezoelectric stack. For applications that require a large stroke, mechanical compliant mechanisms are used to amplify the displacement. In this study, a diamond-shaped compliant mechanism is proposed to amplify the displacement of the piezoelectric stack actuator. It also protects the piezoelectric stack from tensile stresses. The diamond structure is easy to manufacture and does not contain any movable parts. Instead, flexible hinges are used to reduce the wear and tear of the mechanism. This method of amplification has already been successfully implemented in several studies [40, 48, 49], and manufacturers [55, 56]. However, most amplification compliant mechanisms are utilised as an actuator that only generates a force and displacement in one direction. The reason for this, is that the compliant mechanism incorporates a piezoelectric stack as an actuator that is able to generate a large pushing force and only a limited pulling force. Depolarisation occurs when a stack is subjected to a large electric field opposite to the polarisation direction. As described in Section 1.6, the aim of this study is to develop an actuator that is able to generate a bidirectional motion, suitable to minimise the deformation of a structure subjected to thermal loading.

Figure 3.1 illustrates a schematic view of a compliant structure. Mounted in between the compliant structure is a piezoelectric stack that generates a force f_1 and a displacement u_1. Note that the piezoelectric stack is currently working against the stiffness of the compliant structure. Hence, the system stiffness is equal to the stiffness of the stack and the stiffness of the compliant structure. Therefore, the displacement u_1 generated by the piezoelectric stack is not equal to the free displacement. A theoretical discussion of the displacement and force produced by a piezoelectric stack that is working against a load, is presented in Section 2.1.3. When an electric field is applied to the piezoelectric stack, a displacement u_1 and force f_1 is generated and point x in Figure 3.1 exhibits an expansion. This results in a force f_2 and a displacement u_2 at the output of the compliant structure, point y, which contracts. Therefore, the pushing force of the piezoelectric stack is converted to a pulling force.

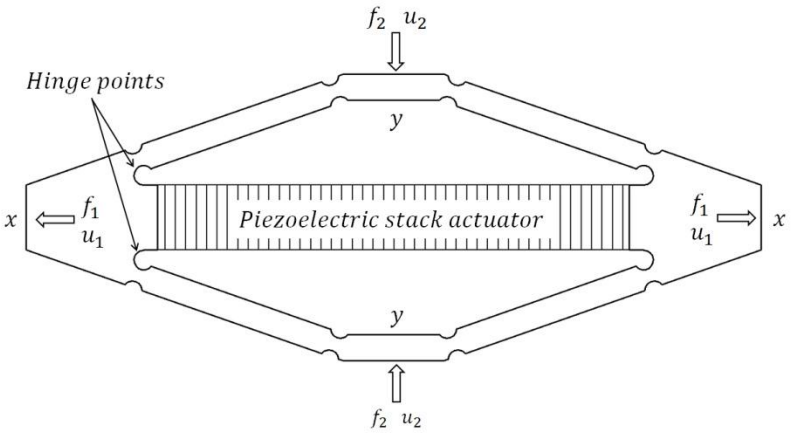

Figure 3.1 Schematic diagram of diamond-shaped compliant structure

It is common in the literature to create leaf hinges by making the compliant structure thinner at the hinge points [48, 49, 56]. This lowers the overall system stiffness, which results in a larger displacement generated by the piezoelectric stack. However, a drawback of creating these leaf hinges is that the lateral stiffness becomes relatively low [49]. Therefore, when a large external load is connected to the output of the compliant structure, the low lateral stiffness may not be sufficient to tolerate the large load, thus resulting in the compliant structure demonstrating unwanted deformation at the leaf hinges. It is therefore important to know what loading conditions are to be applied to the compliant structure so as to prevent distortion due to large loads.

In order to identify the relationship between the geometry of the structure and the amplification factor, consider one quarter of the compliant structure as illustrated by Figure 3.2, where L represents half the length, and h half the height of the compliant structure. The displacement generated by the piezoelectric stack is symbolised by Δ and the resulting displacement at point y is represented by δ. Since the structure is symmetrical, only one quarter is considered. The dotted line represents the initial shape of the compliant structure, where no electrical field is applied to the piezoelectric stack. The dashed line represents the actuated shape as a result of the expanding piezoelectric stack.

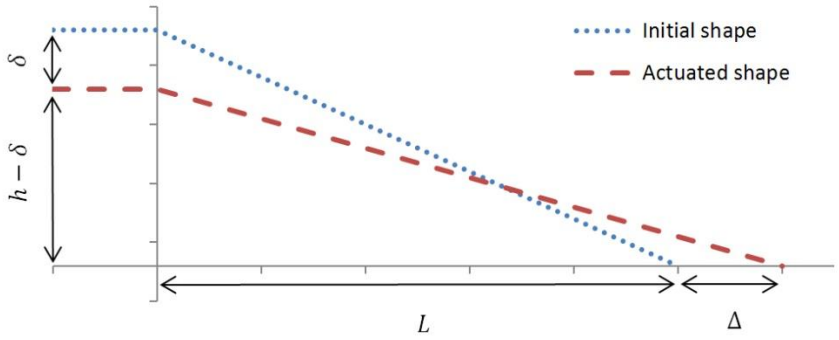

Figure 3.2 Quarter geometry of compliant structure

The assumptions are made that deformation only occurs at the hinging points, x and y, and that the rest of the compliant structure is rigid. The amount of displacement δ can be calculated using basic trigonometry equations, where the length of the hypotenuse can be calculated using:

$$a^2 + b^2 = c^2 \,. \tag{3.1}$$

Assuming that the hypotenuse is rigid, $a = L + \Delta$, $b = h - \delta$, and $c^2 = L^2 + h^2$. Substituting these expressions into (3.1) gives:

$$L^2 + h^2 = (L + \Delta)^2 + (h - \delta)^2 \,. \tag{3.2}$$

Solving (3.2) for the displacement δ at point y:

$$\delta = h - \sqrt{h^2 - 2\Delta L - \Delta^2} \,. \tag{3.3}$$

Equation (3.3) illustrates that the displacement δ depends on the length L and height h of the compliant structure. Therefore, when the length of the structure is increased, while the height stays the same, results in a larger displacement value δ, as illustrated by Figure 3.3. The horizontal axis of the graph represents the ratio between the length and the height of the compliant mechanism.

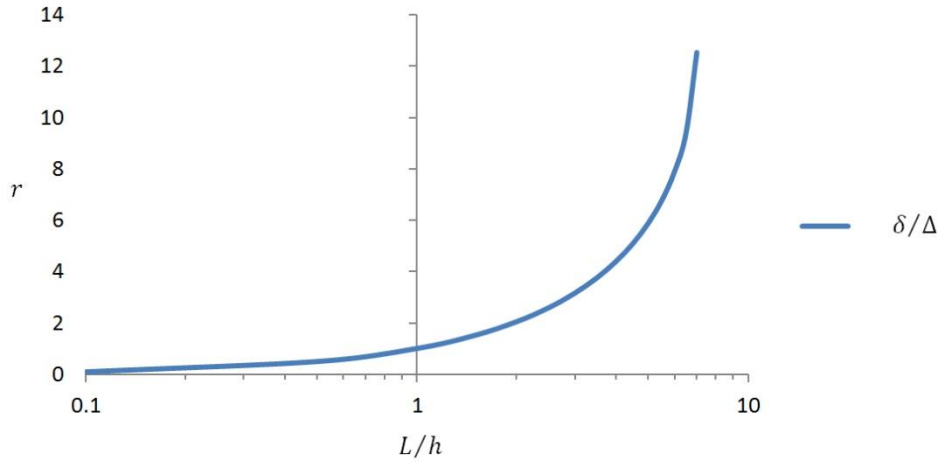

Figure 3.3 Relationship between amplification ratio $\boldsymbol{r}$ and geometry of the compliant structure

The vertical axis of the graph represents the amplification ratio. The amplification ratio is acquired by dividing the amplified displacement δ with the generated displacement of the piezoelectric stack Δ and is represented by (3.4):

$$r = \frac{h - \sqrt{h^2 - 2\Delta L - \Delta^2}}{\Delta} = \frac{\delta}{\Delta}. \tag{3.4}$$

The graph in Figure 3.3 illustrates that, when the length is equal to the height of the compliant structure, $L = h$, no amplification occurs. When the length is less than the height ($L < h$), the displacement of the piezoelectric stack is reduced. Therefore, it is important to keep the length greater than the height ($L > h$), which results in an amplification. The amplification factor is limited by the height of the compliant structure. The amplified displacement δ must always be smaller than the height h of the compliant structure, i.e. $\delta < h$.

Now that the relationship between the geometry and the amplification factor of the compliant structure is identified, this chapter continues with a brief discussion about two initial FEM analyses that were conducted to find the optimal piezoelectric stack configuration to achieve bidirectional displacements.

3.2 FEM Analysis of a Triple-Stack Bidirectional Actuator

Since piezoelectric stack actuators exhibit semi-bidirectional actuation, a compliant structure is used to achieve full bidirectional actuation, without the need of large negative electrical fields. Two preliminary finite element analyses are conducted to identify the optimal piezoelectric stack configuration.

The two models and the configuration of the piezoelectric stacks are illustrated by Figure 3.4 and Figure 3.5. The piezoelectric stacks in Model 1, represented by Figure 3.4, are configured in opposing fashion. Therefore, the forces generated by the outside stacks are directly applied to the inside stack and vice versa. The bidirectional actuation is achieved by applying opposite potentials to the inner stack and the outer two stacks. For instance, by applying a positive electrical field to both outside stacks and the maximum allowable negative electrical field (which is usually 20% of the maximum positive electrical field [18]) to the middle stack, results in the compliant structure exhibiting an expansion. Conversely, when a positive electrical field is applied to the middle stack and the maximum allowable negative electrical field is applied to the two outside stacks, the compliant structure contracts. Model 2, illustrated by Figure 3.5, consists of two vertical piezoelectric stacks and one horizontal piezoelectric stack. The mode of operation is identical to the first model. However, because of the different stack configuration, the force generated by the horizontal stack is first transferred to the compliant structure before it contracts both vertical stacks. Therefore, the forces generated by the piezoelectric stacks are not working directly against one another, unlike the case of the actuator in Model 1. This results in a more compact actuator, where all three stacks are protected against tensile forces by the compliant structure.

The piezoelectric stacks used in both models are identical, where the two outside stacks in the first model and the vertical stacks in the second model, exhibit dimensions of 5 mm × 5 mm × 18 mm. The horizontal stack, in both models, has a dimension of 5 mm × 5 mm × 36 mm. The material used to model the piezoelectric stacks is PZT5H ceramic, whereas the compliant structure is modelled using stainless steel 304. All material properties can be found in Appendix A. Table 3.1 describes the total dimensions and the number of nodes used in the FEM models.

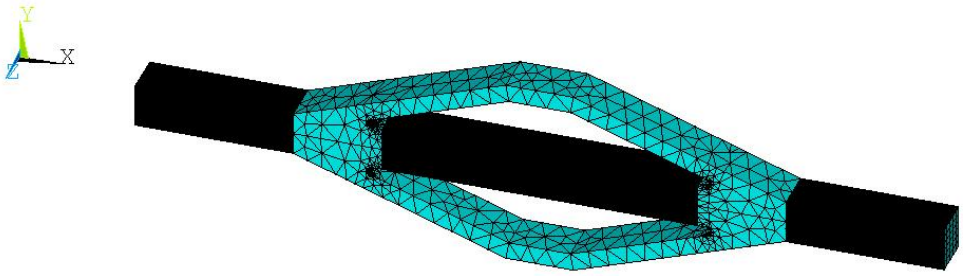

Figure 3.4 Initial bidirectional actuator configuration of Model 1

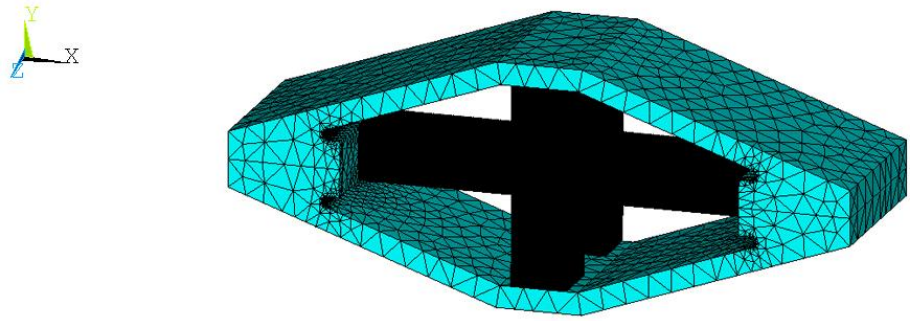

Figure 3.5 Initial bidirectional actuator configuration of Model 2

	X-direction [m]	Y-direction [m]	Z-direction [m]	No. of nodes
Model 1	$92E^{-3}$	$22E^{-3}$	$5E^{-3}$	245,439
Model 2	$56E^{-3}$	$22E^{-3}$	$16E^{-3}$	269,410

Table 3.1 Total dimensions [m] and the number of nodes of Model 1 and Model 2

Both actuators are modelled in ANSYS and are built using the 3-dimensional, SOLID226 element type. The element is set to perform a piezoelectric analysis. The connection between the piezoelectric stacks and the compliant structure is modelled using MPC contact algorithms. Each element in the piezoelectric stacks has a thickness of 0.1E^{-3} m. The free displacement of each stack, for the maximum allowable electric field of 120 V, can be theoretically calculated using (2.26). The free displacement for the 18 mm stack has a value of:

$$\delta_0 = \frac{593\text{E}^{-12} \times 18\text{E}^{-3}}{0.1\text{E}^{-3}} \times 120 = 12.80\text{E}^{-6}\ \text{m}\,, \tag{3.5}$$

whereas the 36 mm stack exhibits a free displacement of:

$$\delta_0 = \frac{593\text{E}^{-12} \times 36\text{E}^{-3}}{0.1\text{E}^{-3}} \times 120 = 25.62\text{E}^{-6}\ \text{m}\,. \tag{3.6}$$

For a negative electrical field of −20 V, the free displacement for the 18 mm stack is:

$$\delta_0 = \frac{593\text{E}^{-12} \times 18\text{E}^{-3}}{0.1\text{E}^{-3}} \times -20 = -2.13\text{E}^{-6}\ \text{m}\,, \tag{3.7}$$

whereas the free displacement for the 36 mm stack is calculated to be:

$$\delta_0 = \frac{593\text{E}^{-12} \times 36\text{E}^{-3}}{0.1\text{E}^{-3}} \times -20 = -4.27\text{E}^{-6}\ \text{m}\,. \tag{3.8}$$

Comparing the results of (3.5) and (3.6) with (3.7) and (3.8) demonstrates the semi-bidirectional operation of a piezoelectric stack actuator. The generated free displacement, in the expanding direction, is not equal to the free displacement, in the contracting direction. Note that the calculated values in (3.5) – (3.8) are free displacements, where the force applied to the stacks is zero. However, the stacks are working in opposing fashion and against the compliant structure and each other.

Therefore, the displacement generated by the stacks within the compliant structure, is less than the free displacement for the individual stacks.

The amplification factor r of the compliant structures can be calculated using (3.4), where Δ is substituted with half the displacement of the 36 mm stack, calculated in (3.6). The amplification factor r is predicted to be:

$$r = \frac{\left(6.5\mathrm{E}^{-3} - \sqrt{(6.5\mathrm{E}^{-3})^2 - 2 * 12.81\mathrm{E}^{-6} * 16.1\mathrm{E}^{-3} - (12.81\mathrm{E}^{-6})^2}\right)}{12.81\mathrm{E}^{-6}} = 2.48\,. \tag{3.9}$$

The compliant structures, for both Model 1 and 2, have identical dimensions in the X and Y-directions. Therefore, the calculated amplification factor in (3.9) is identical for both structures. The major difference between the two models is that the most left and right side of the outside piezoelectric stacks of Model 1 must be constrained in the X-direction, whereas the piezoelectric stacks in Model 2 are constrained by the compliant structure.

The electrical fields applied to both models are 120 V and −20 V. The compliant structures contract when 120 V is applied to the 36 mm stack and −20 V to both 18 mm stacks, whereas, the compliant structures expand when −20 V is applied to the 36 mm stack and 120 V to both 18 mm stacks. A static analysis is performed with the analysis type option set to “Small Displacement Static”, which performs a linear static analysis. Figure 3.6 and Figure 3.7 illustrate the solution of the Y-component displacement when the compliant structure contracts. A summary of the FEM-computed displacement values is given in Table 3.2, where the displacements are acquired according to the method described in Section 2.2.4.

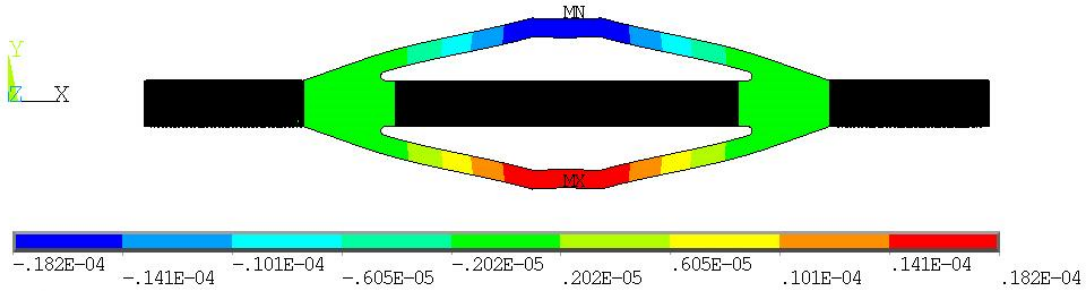

Figure 3.6 Y-component of displacement [m] of Model 1, where an electrical field of 120 V is applied to the middle stack and −20 V is applied to both outside stacks

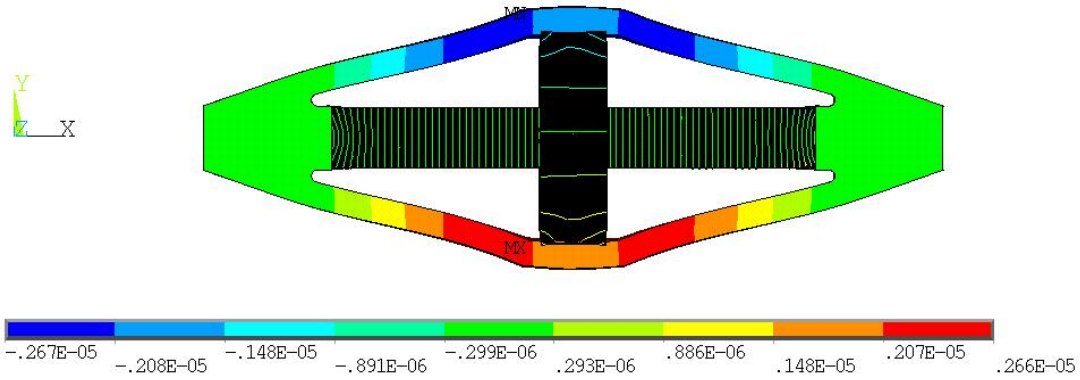

Figure 3.7 Y-component of displacement [m] of Model 2, where an electrical field of 120 V is applied to the horizontal stack and −20 V is applied to both vertical stacks

	Model 1 [m]		**Model 2 [m]**	
	Contract	**Expand**	**Contract**	**Expand**
FEM-computed δ of 36 mm stack	$13.94E^{-6}$	$-13.86E^{-6}$	$4.29E^{-6}$	$-4.08E^{-6}$
FEM-computed amplified δ of the structure	$-35.21E^{-6}$	$34.84E^{-6}$	$-4.47E^{-6}$	$11.88E^{-6}$

Table 3.2 FEM-computed displacements [m] of Model 1 and Model 2

The FEM-computed amplified displacement values for the contracting and expanding directions for Model 1, described in Table 3.2, are almost identical, whereas the FEM-computed amplified displacement values for Model 2 are not. The reason for this is illustrated in Figure 3.7, which shows that deformation occurs not only at the hinges, as assumed when calculating the amplification factor and the amplified displacement, but also on all four arms of the compliant structure. The deformation is caused by the horizontal stack, which force and displacement are transferred through the compliant structure, to the two vertical stacks or vice versa. The horizontal stack, in Figure 3.7, extends more than the vertical stacks contract, which causes the compliant structure to deform. Therefore, based on the results described in Table 3.2, the most optimal configuration of achieving bidirectional displacements is by operating the stacks in opposing fashion, where the stacks are working directly against one another, as illustrated by Figure 3.4. An identical contracting and expanding displacement is achieved when, the sum of the displacements generated by the contracting stacks, is equal to the sum of displacements generated by the expanding stack, and vice versa.

The theoretically calculated amplification factor of the compliant structure in (3.9) has a value of 2.48. In order to verify the amplification factor of the compliant structure, the FEM-computed amplified displacement of the structure in Model 1 is divided by the FEM-computed displacement of the 36 mm stack, described in Table 3.2, and is calculated to be:

$$r_{contract} = \frac{35.21E^{-6}}{13.94E^{-6}} = 2.53\,, \tag{3.10}$$

$$r_{expand} = \frac{34.84E^{-6}}{13.86E^{-6}} = 2.51\,. \tag{3.11}$$

Calculating the error between the theoretically calculated amplification factor in (3.9) and the FEM-computed amplification factor in (3.10) and (3.11) gives, 2% and 1.2% respectively. The reason for this difference to occur is that the compliant structure deforms when the displacement is transferred from the horizontal stack to the output

areas. The calculations demonstrate that it is possible to estimate the amplification factor of the compliant structure. However, it is difficult to estimate the amplified displacement, since one has to know the generated displacement of the stack working against the compliant structure, which is not equal to the theoretical free displacement. In order to estimate the amplified displacement, one can either compute the displacement using the finite element method or calculate the generated displacement of the stack by incorporating the stiffness of the compliant structure in the calculations.

Based on the findings in this chapter, the next chapter continues by presenting a design of an amplified bidirectional actuator, where the configuration of the piezoelectric stacks in the bidirectional actuator are configured in an opposing fashion to achieve identical contracting and extending displacements.

Chapter 4

FEM Analysis of an Amplified Dual-Stack Actuator

In this chapter, the design and implementation of a bidirectional dual-stack actuator is discussed. The dual-stack actuator, developed by Heverly *et al.* [41], is used as the basis for this proposal. A finite element model of the dual-stack actuator is built and a static analysis is conducted to study its behaviour, free displacements, and blocked forces. The performance and limitations of the actuator are outlined and discussed. A new Amplified Dual-Stack Actuator (ADSA) is then proposed. This actuator combines the dual-stack actuator with a diamond-shaped compliant structure, as introduced in Chapter 3, to amplify the displacements. A finite element model of the ADSA is built to simulate and identify its displacement and blocked force values. To study the actuation performance of the ADSA, a benchmark model is created. The benchmark model consists of a beam structure with two film heaters, each bonded to either surface of the structure, to induce a through-the-thickness thermal difference. Two piezoelectric patches, each mounted on either surface of the structure, compensate for the thermal deformation. A structural-thermoelectric coupled-field analysis is conducted to analyse the compensation performance of the two piezoelectric patches.

The ADSA is then mounted onto an identical beam structure, as used in the benchmark model, and an identical analysis is conducted to evaluate the effectiveness and compensation performance of the ADSA. At the end of this chapter, the results of both analyses are compared and discussed.

4.1 Dual-Stack Actuator Construction and Operation

The dual-stack actuator, developed by Heverly *et al.* [41], is cylindrical in shape and contains two stacks composed of piezoelectric ring elements. The two stacks operate in an opposing fashion. The cross-sectional view through the centreline of the actuator is illustrated by Figure 4.1. Both piezoelectric stacks are connected to each other through a piston. The central part of the housing contains a fixed stop and piston guide. Each stack element is placed between the moving piston and the central housing stop. The piezoelectric stacks are not bonded to the piston or the housing, which eliminates the possibility of developing tensile stresses in the piezoelectric stack elements. The exposed end of the piston is used to connect an external load to the actuator, while the other connection can be made through the outer housing wall to keep the actuator in its place.

To create a bidirectional motion, both piezoelectric stacks operate in opposing fashion. Therefore, when a positive electrical field is applied to Stack 1, it extends and moves the piston backwards, which forces Stack 2 to contract. The actuator is generating a contracting displacement. Conversely, when a positive electrical field is applied to Stack 2, it extends and moves the piston forwards, which forces Stack 1 to contract. The actuator is generating an extending displacement.

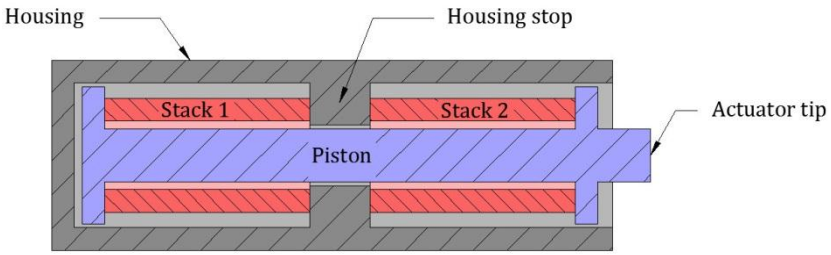

Figure 4.1 Cross-sectional view of the dual-stack actuator

The output force is only generated by the piezoelectric stack that is extending. The other piezoelectric stack contracts to eliminate resistance to the force generated by the expanding stack.

Exposure to a strong electric field of polarity, opposite to that of the polarising field of the piezoelectric stack, depolarises the material. The degree of depolarisation depends on the type of material, the exposure time, the temperature and other factors. Therefore, the maximum negative electrical field strength, applied to the stacks, is usually only 20% of the maximum allowable positive electrical field [18]. In order to create equal bidirectional displacements, Heverly *et al.* [41] varied the electrical field applied to Stack 1 and Stack 2 around a DC-bias, where the electrical field is opposite in phase for each stack, as shown in (4.1) and (4.2):

$$V_1 = V_0 + \Delta V \text{ and } V_2 = V_0 - \Delta V\,, \tag{4.1}$$

$$V_1 = V_0 - \Delta V \text{ and } V_2 = V_0 + \Delta V\,, \tag{4.2}$$

where V_1 and V_2 are the electrical fields applied to Stack 1 and 2, V_0 is the DC-bias voltage and ΔV is the variational portion of the applied electrical field. The magnitude of the DC-bias is acquired by dividing the total electrical field range, applied to the piezoelectric stack in half. Equation (4.1) generates electrical fields for a contracting displacement and (4.2) generates electrical fields for an extending displacement. Table 4.1 describes the electrical fields applied to the stacks in the study of Heverly *et al.* [41] to achieve bidirectional actuation, where i_V_1 and i_V_2 are the initial electrical fields applied to Stack 1 and 2. The initial position of the piston is denoted by i_pos_p, V_1 and V_2 are the electrical fields applied to stack 1 and 2 and e_pos_p is the end position of the piston.

	i_V_1	i_V_2	i_pos_p	V_1	V_2	e_pos_p
Pushing	50	50	Neutral	0	100	Extended
Pulling	50	50	Neutral	100	0	Contracted

Table 4.1 Applied electrical fields to the dual-stack actuator to achieve bidirectional actuation

Figure 4.2 illustrates the different positions of the actuator, where the initial state (b) is the neutral position. In this position, the actuator can either push to its extended position (a), where Stack 2 extends and Stack 1 contracts, or pull to its contracted position (c), where Stack 1 extends and Stack 2 contracts. The dual-stack actuator always experiences a compressive stress caused by the initial electrical field that keeps the actuator in the neutral position. The initial electrical field also preloads the actuator, which eliminates the need of an internal preloading spring so that the free displacements of the actuator are unaltered. Preloading the piezoelectric material is highly recommended to protect the material against tensile stresses, external shocks and irregular signals, which can destroy the piezoelectric stack [18].

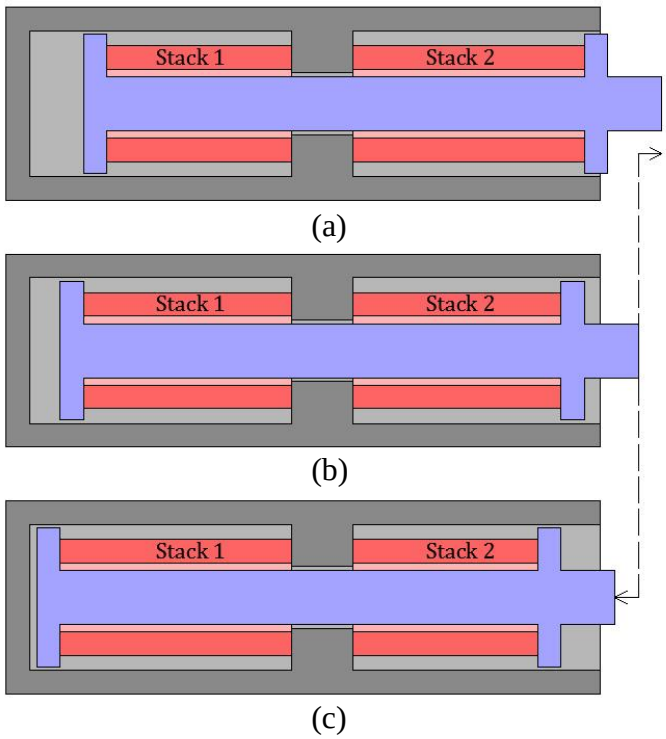

Figure 4.2 (a) Extended position of the dual-stack actuator; (b) initial or neutral position of the dual-stack actuator; (c) contracted position of the dual-stack actuator

4.2 Analytical Analysis of the Dual-Stack Actuator

The free displacement and blocked force, which are discussed in Section 2.1.3, are two important design parameters to characterise a piezoelectric material. To reiterate, the free displacement is the displacement produced by the piezoelectric material when there is no force applied to the material. The blocked force is the force generated by the material when the displacement is constrained to be zero.

Heverly *et al*. [41] conducted a quasi-static analysis and applied several input voltages to the actuator, in four steps, to derive the free displacement and blocked force expressions for the dual-stack actuator.

Step 1 Apply the DC-bias voltage, $V_1 = V_2 = V_0 = 50$ V and external load $F_{ext} = 0$ N to establish the neutral position of the actuator as the initial position, illustrated in Figure 4.2(b).

Step 2 Apply the variational portion of the input voltage $\Delta V = 50$ V so that $V_1 = 100$ V, $V_2 = 0$ V, $F_{ext} = 0$ N to establish the contracted position, x_a, illustrated in Figure 4.2(c).

Step 3 Alternate the input voltage $V_1 = 0$ V, $V_2 = 100$ V, $F_{ext} = 0$ N to establish the extended position, x_b, illustrated in Figure 4.2(a).

Step 4 Maintain the voltage inputs, $V_1 = 0$ V, $V_2 = 100$ V, and apply an external load F_{ext} of increasing magnitude until the actuator returns to the contracted position, x_a. The final load is equivalent to the blocked force, and the free stroke is the difference between Step 3 and Step 4.

A schematic diagram of the dual-stack actuator is illustrated in Figure 4.3. Both piezoelectric stacks are modelled in terms of force F_{ind1}, F_{ind2}, and short-circuit stiffness $K_{a(1)}$, $K_{a(2)}$, for Stack 1 and Stack 2, respectively. Heverly *et al.* [41] expressed the free displacement, x_0, of the dual-stack actuator as:

$$x_0 = x_b - x_a \,, \tag{4.3}$$

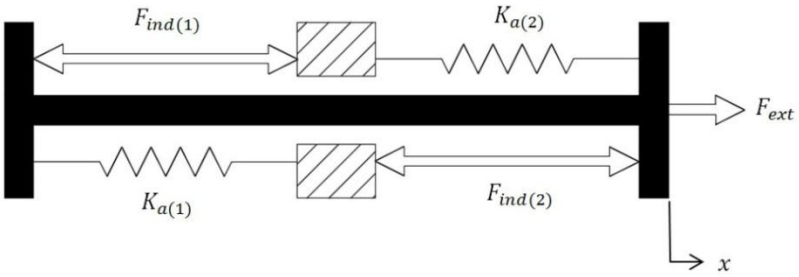

Figure 4.3 Schematic diagram of the dual-stack actuator

where, x_b represents the actuator in the extended position, and x_a represents the actuator in the contracted position. The displacements generated by the piezoelectric stacks are represented by $x_a = -F_{ind(1)}/(K_{a(1)} + K_{a(2)})$, and $x_b = F_{ind(2)}/(K_{a(1)} + K_{a(2)})$. Substituting these expressions into (4.3) gives:

$$x_0 = \frac{F_{ind(2)}}{(K_{a(1)} + K_{a(2)})} - \frac{-F_{ind(1)}}{(K_{a(1)} + K_{a(2)})}. \tag{4.4}$$

Heverly *et al.* [41] assumed that the induced force and stiffness of Stack 1 are identical to the induced force and stiffness of Stack 2, $F_{ind(1)} = F_{ind(2)}$ and $K_{a(1)} = K_{a(2)}$. Therefore, (4.4) becomes:

$$x_0 = \frac{2F_{ind}}{2K_a} = \frac{F_{ind}}{K_a}. \tag{4.5}$$

The resultant free displacement, represented by (4.5), is equivalent to the free displacement of a single piezoelectric stack. Note that (4.3) defines the free stroke as the difference between the extended and contracted position. When the actuator operates in the bidirectional mode, in order to perform a push or pull actuation, the free stroke is a factor two smaller.

Heverly *et al.* [41] expressed the blocked force F_{bl} of the dual-stack actuator as :

$$F_{bl} = \left(K_{a(1)} + K_{a(2)}\right)x_a - F_{ind(2)} \, . \tag{4.6}$$

The displacement x_a can be represented as $-F_{ind(1)}/(K_{a(1)} + K_{a(2)})$. Substituting this expression into (4.6) gives:

$$F_{bl} = \left(K_{a(1)} + K_{a(2)}\right)\frac{-F_{ind(1)}}{(K_{a(1)} + K_{a(2)})} - F_{ind(2)} = -2F_{ind} \, . \tag{4.7}$$

The resultant blocked force of the actuator, as shown in (4.7), is reported to be twice the blocked force of a single freestanding piezoelectric stack. This is a consequence of the applied measuring method and differs from the conventional definition for the blocked force. Heverly *et al.* [41] measured the blocked force by applying an external load of increasing magnitude to the actuator. The initial position of the actuator is the extended position where $V_1 = 0$ V, $V_2 = 100$ V. The magnitude of the external load is increased, causing the actuator to contract while the electrical fields applied to the stacks are left unaltered. The actuator continues to contract and Stack 2, which is generating the force, is compressed by the increasing external load past its neutral point into contraction until the dual-stack actuator reaches its contracted position. Therefore, the displacement generated by Stack 2 is not constrained to be zero, since the stack is compressed past its neutral point. The maximum force or stress that a piezoelectric stack is able to generate is where the displacement or strain is zero, as illustrated by Figure 2.2. It is unusual to compress the piezoelectric stack past the point where the displacement is zero, since the stack is unable to overcome the external force.

The conventional way of measuring the blocked force is to block the actuator from extending and, therefore, constraining the displacement to zero, while the maximum electrical field is applied. In the dual-stack actuator case, the actuator should initially be in its neutral position, as illustrated in Figure 4.2(b), where the tip

of the dual-stack actuator is constrained to be zero. The electrical fields, $V_1 = 0$ V, $V_2 = 100$ V are then applied, which causes the actuator to attempt to extend. The force measured at the tip of the actuator is equal to the blocked force. This method has been applied in a study by Bharty and Frecker to measure the blocked force of a compliant mechanism piezoelectric actuator [42].

4.3 FEM Analysis of the Dual-Stack Actuator

In this section, the development of a finite element model to study the behaviour of the dual-stack actuator is presented. First, the free displacement and blocked force of a piezoelectric stack, which is identical in properties to the stack used in the dual-stack actuator, are simulated. The results are validated using the constitutive equations of a piezoelectric stack, discussed in Section 2.1.3, and the data provided by the manufacturer. The finite element model is then expanded to simulate the behaviour, free displacements and blocked forces of the dual-stack actuator.

4.3.1 Validation of a Piezoelectric Stack

Heverly *et al.* [41] incorporated two piezoelectric stacks from the manufacturer American Piezo Ceramics (APC), in the dual-stack actuator. The stacks are of type HPst 150/14–10/25 and consist of ring elements. The specifications of the piezoelectric stacks provided by the manufacturer are listed in Appendix A. Since the piezoelectric stack exhibits axisymmetric properties, it is simulated using the PLANE223 element type, which options are set to perform an axisymmetric, piezoelectric analysis. The number of piezoelectric elements used in the stack is 262. Hence, the thickness of each piezoelectric ring for the 27 mm stack is 103E^{-6} m. The model is meshed using quadrilateral-shaped elements with the element size set to 0.1E^{-3} m. The number of elements and nodes generated in the finite element model are described in Table 4.2. An electrical field of 150 V is applied to the electrodes, so that it is possible to make a comparison between the simulated displacement of the finite element model and the displacement values specified by the manufacturer.

Number of elements	15,720
Number of nodes	48,269
Analysis type	Small Displacement Static

Table 4.2 Finite element model information of the piezoelectric stack actuator

One side of the stack is constrained in the Y-direction and the model is solved for the displacement. Figure 4.4 illustrates the free displacement of the piezoelectric stack in the Y-direction, when a positive electrical field is applied. The FEM-computed maximum displacement of the piezoelectric stack is 25E^{-6} m.

To simulate the blocked force, both ends of the piezoelectric stack are constrained in the Y-direction, which forces the displacement to be zero. An electrical field of 150 V is then applied and the finite element model is solved for the stress. Figure 4.5 illustrates the simulated Y-component of stress of the piezoelectric stack in Pascal. Note that the Y-component of stress is identical through the whole stack. Hence, only the top surface is illustrated. The Y-component of stress holds a value of 51.1 MPa. The relationship between stress and force is represented by:

$$\sigma = \frac{F}{A}, \tag{4.8}$$

where σ represents the stress, A the cross-sectional area, and F represents the force. Solving (4.8) for the FEM-computed blocked force gives:

$$F_{bl} = 0.511\text{E}^{8} * \left(7.5\text{E}^{-3^2}\pi - 4.5\text{E}^{-3^2}\pi\right) = 5779 \text{ N}. \tag{4.9}$$

The free displacement and blocked force of the piezoelectric stack are also theoretically calculated using the constitutive equations, which are discussed in Section 2.1.3.

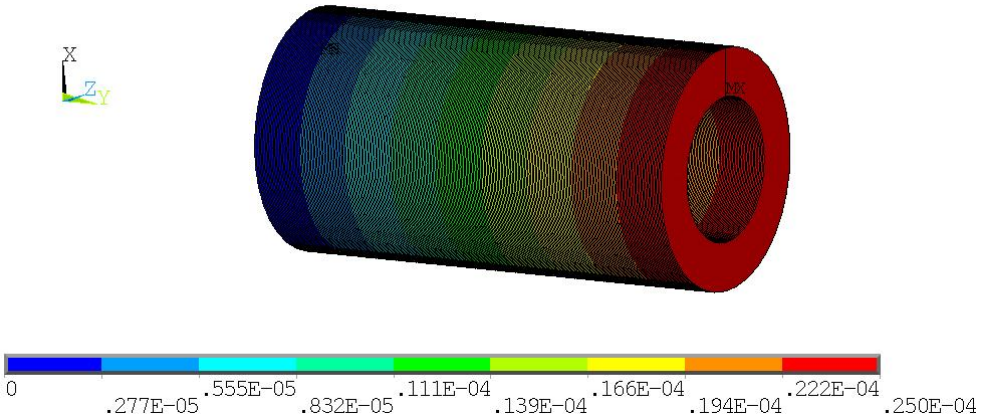

Figure 4.4 Y-component of displacement [m] generated by the piezoelectric stack at 150 V

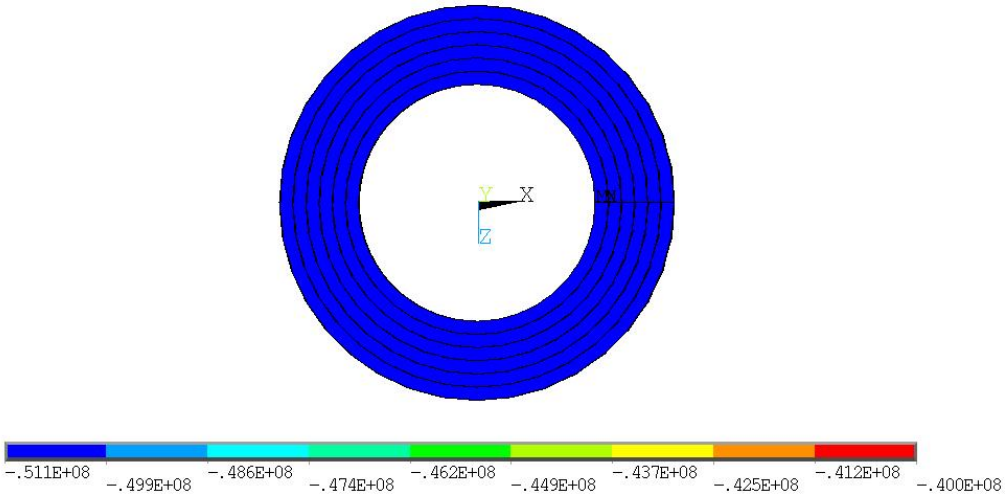

Figure 4.5 Top view of the Y-component of stress [Pa] generated by the piezoelectric stack at 150 V

The free displacement is calculated using (2.26) and has a value of:

$$\delta_0 = 635^{-12} * \frac{27\mathrm{E}^{-3}}{103\mathrm{E}^{-6}} * 150 = 24.97\mathrm{E}^{-6}\ \mathrm{m}\,, \tag{4.10}$$

whereas the blocked force is calculated using (2.27) and has a value of:

$$F_{bl} = 635\mathrm{E}^{-12} * \left(\frac{1}{18.1\mathrm{E}^{-12}}\right) * \frac{\left(7.5\mathrm{E}^{-3^2}\pi - 4.5\mathrm{E}^{-3^2}\pi\right)}{\left(\frac{27\mathrm{E}^{-3}}{262}\right)} * 150 = 5775\ \mathrm{N}\,. \tag{4.11}$$

Table 4.3 illustrates a comparison between the theoretical and FEM-computed free displacement and the manufacturer's specification. The FEM-computed and the theoretically calculated free displacements are almost identical to the manufacturer's specifications. An additional simulation and calculation is performed using an electrical field of 100 V, in order to make a comparison with the data of Heverly *et al.* [41], since they used an electrical field of 100 V to excite the dual-stack actuator. Table 4.4 compares the different values of the blocked force and it is noticeable that the theoretical and FEM-computed solutions are different from the manufacturer's specifications. The reason for this difference may be that the elastic compliance Y_3^E, which is used to calculate the blocked force in (4.11) and ANSYS is considered linear, whereas the manufacturer's specifications are measured in a practical situation. Due to the ferroelectric nature of piezoelectric ceramics, the specified parameters can vary significantly with the operating electrical field strength [18]. In practice, piezoelectric ceramics are operated with large field excitation levels for actuation, i.e. $E > 1$ kV/mm, while the piezoelectric data given by the manufacturer is measured at small signal values, i.e. $E \ll 100$ V/mm, at room temperature.

Electrical field	ANSYS [m]	Theory [m]	Manufacturer's spec. [m]
150 V	$25.00\mathrm{E}^{-6}$	$24.79\mathrm{E}^{-6}$	$25.00\mathrm{E}^{-6}$
100 V	$16.60\mathrm{E}^{-6}$	$16.65\mathrm{E}^{-6}$	N/A

Table 4.3 Comparison of the FEM-computed and theoretically calculated free displacement values [m] generated by the piezoelectric stack

Electrical field	ANSYS [N]	Theory [N]	Manufacturer's spec. [N]
150 V	5779	5775	4500 (−30 to 150 V)

Table 4.4 Comparison of the the FEM-computed and theoretically calculated blocked force values [N] generated by the piezoelectric stack

4.3.2 Finite Element Model of the Dual-Stack Actuator

After the finite element model of the piezoelectric stack that is incorporated in the dual-stack actuator is validated, the model is expanded to simulate the full dual-stack actuator. The model is generated using the ANSYS Parametric Design Language (APDL) scripting language, which allows the model to be built with the use of parameters. An advantage of building the model using APDL is that it is easy to change important design parameters, without redesigning the entire model. Figure 4.6 and Table 4.5 illustrate the geometry and dimensions of the dual-stack actuator designed by Heverly *et al* [41].

An identical dual-stack actuator is built in ANSYS where the housing and piston of the actuator are modelled out of stainless steel 304. The material data used in the analysis can be found in Appendix A. The actuator is modelled using the 2-D element type PLANE223 with KEYOPT(1) set to 1001 to perform a piezoelectric analysis. Since the actuator exhibits symmetry, KEYOPT(3) is set to "1" to set the element behaviour to axisymmetric. The entire model is meshed using quadrilateral element shapes, where element size for the piezoelectric stacks is $0.1E^{-3}$ m and the element size for the housing and piston is $0.5E^{-3}$ m. Each piezoelectric stack is bonded to the piston and housing using the MPC contact algorithm. The locations of the contact algorithms and the generated finite element model are illustrated by Figure 4.7. More information regarding the MPC algorithm can be found in Section 2.2.3. The left side of the actuator is constrained in all directions and the model is solved for the displacement. The FEM-computed displacements are measured at the tip of the actuator, as illustrated by Figure 4.1. Relevant information about the generated model is given in Table 4.6. The number of nodes is significantly larger compared to the model of the single piezoelectric stack and the total mass of the actuator is approximately 230 g.

The type of analysis is set to piezoelectric and contains three solution phases. In the first phase, the dual-stack actuator is solved for the displacement in the contracted position. Therefore, an electrical field of 100 V is applied to Stack 1 and 0 V to Stack 2.

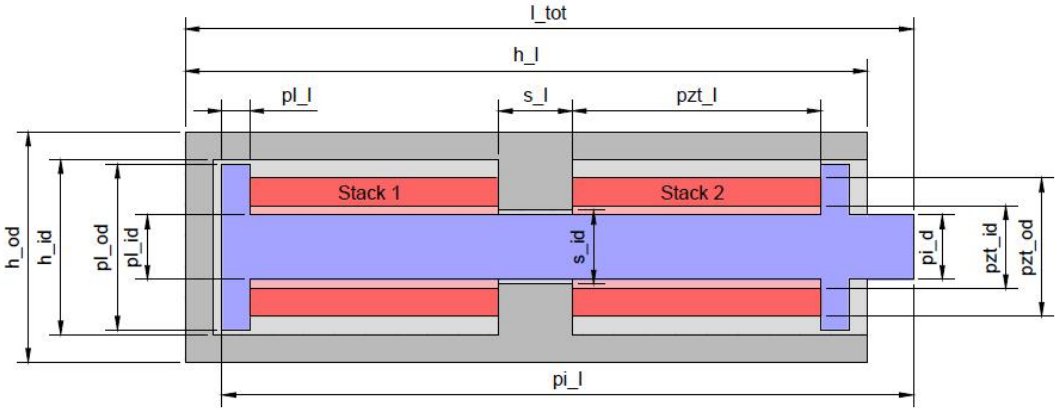

Figure 4.6 Geometry and parameters of the dual-stack actuator

Parameter	Description	Value [m]
h_od	Outer diameter of the housing	$25.0E^{-3}$
h_id	Inner diameter of the housing	$19.0E^{-3}$
h_l	Housing length	$74.0E^{-3}$
pl_od	Outer diameter of the plunger	$18.0E^{-3}$
pl_id	Inner diameter of the plunger	$7.0E^{-3}$
pl_l	Plunger length	$3.0E^{-3}$
s_l	Housing stop length	$8.0E^{-3}$
s_id	Inner diameter of the housing stop	$8.0E^{-3}$
pzt_od	Outer diameter of the piezoelectric stack	$15.0E^{-3}$
pzt_id	Inner diameter of the piezoelectric stack	$9.0E^{-3}$
pzt_l	Length of the piezoelectric stack	$27.0E^{-3}$
pi_l	Length of the piston	$75.0E^{-3}$
pi_d	Diameter of the piston	$7.0E^{-3}$
l_tot	Total length of the actuator	$79.0E^{-3}$

Table 4.5 Parameters and dimensions of the dual-stack actuator

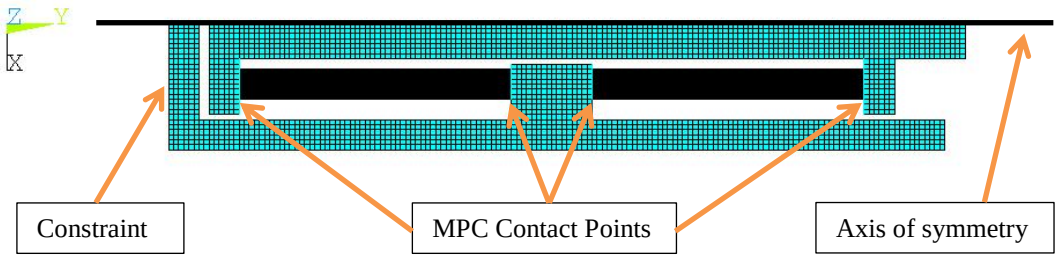

Figure 4.7 Generated 2-D axisymmetric finite element model of the dual-stack actuator

Number of elements	34,254
Number of nodes	104,742
Analysis type	Small Displacement Static
Mass	227.84 g

Table 4.6 Finite element model information of the dual-stack actuator

In the second phase, the dual-stack actuator is solved for the displacement in the neutral position, where an electrical field of 50 V is applied to both piezoelectric stacks. In the third and last phase, the dual-stack actuator is solved for the generated displacement in the extended position, where an electrical field of 0 V is applied to Stack 1 and 100 V to Stack 2. After solving each phase, the results are written to a database file.

4.3.3 Free Displacement Results of the Dual-Stack Actuator

Figure 4.8, Figure 4.9, and Figure 4.10 illustrate the nodal solution of the Y-component of displacement for the contracted, neutral, and extended positions, respectively. The figures demonstrate that the colour bands on the piston changes, where each colour represents a certain displacement value. The displacement value is the difference between the original position of the node and the new position. The displacement is acquired at the tip of the actuator, since this is the point where an external load can be attached to the actuator.

The tip of the actuator in the contracted position, illustrated by Figure 4.8, exhibits a displacement of $-4.32E^{-6}$ m, whereas the left side of the piston exhibits a

displacement in the negative direction of $-11.55E^{-6}$ m. This indicates that the piston deforms due to its elasticity. The tip of the actuator in the neutral position, in Figure 4.9, exhibits a displacement of $3.73E^{-6}$ m, whereas the left side of the piston shows a displacement of $-3.47E^{-6}$ m. Figure 4.10 illustrates the displacement of the actuator in the extended position. In this position, the tip of the actuator exhibits a displacement of $11.78E^{-6}$ m, whereas, the left side of the piston shows a displacement of $4.60E^{-6}$ m.

The figures illustrate that the piston stretches due to the force generated by the piezoelectric stacks. This does not seem to be a problem for the extended position, since the tip of the actuator exhibits maximum displacement. However, the tip of the actuator in the contracted position only exhibits a displacement of $-4.32E^{-6}$ m. The loss of displacement is calculated for the contracted position by taking the displacement at the left side of the piston, $-11.55E^{-6}$ m, and subtracting the displacement at the tip of the actuator, which is $-4.32E^{-6}$ m. The loss of displacement, due to the elasticity of the piston, is calculated to be $-7.23E^{-6}$ m. The reason that the displacement at the tip of the actuator varies, between the contracted position and the extended position, is caused by the difference in distance between Stack 1 to the tip of the actuator and Stack 2 to the tip of the actuator. The forces generated by the piezoelectric stacks are transferred through the piston. The distance between piezoelectric Stack 1 and the tip of the actuator is larger than the distance between piezoelectric Stack 2 and the tip of the actuator. The compliance of the piston is proportional to the effective length. Therefore, Stack 1 experiences a larger compliance than Stack 2, which causes the difference in displacement. Table 4.7 illustrates the displacement values generated by the dual-stack actuator.

Contracted position [m]	**Neutral position [m]**	**Extended position [m]**
$-4.32E^{-6}$	$3.73E^{-6}$	$11.78E^{-6}$
Δ displacement		Δ displacement
$8.05E^{-6}$		$8.05E^{-6}$

Table 4.7 FEM-computed free displacements [m] generated by the dual-stack actuator

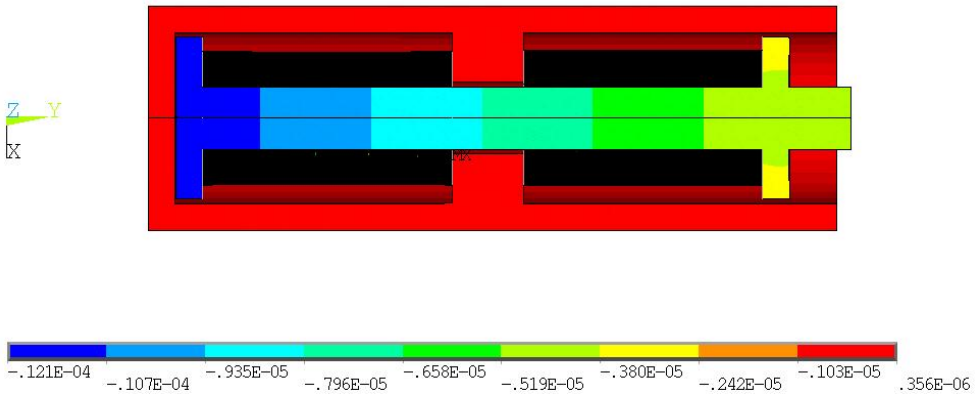

Figure 4.8 Y-component of displacement [m] generated by the dual-stack actuator in the contracted position

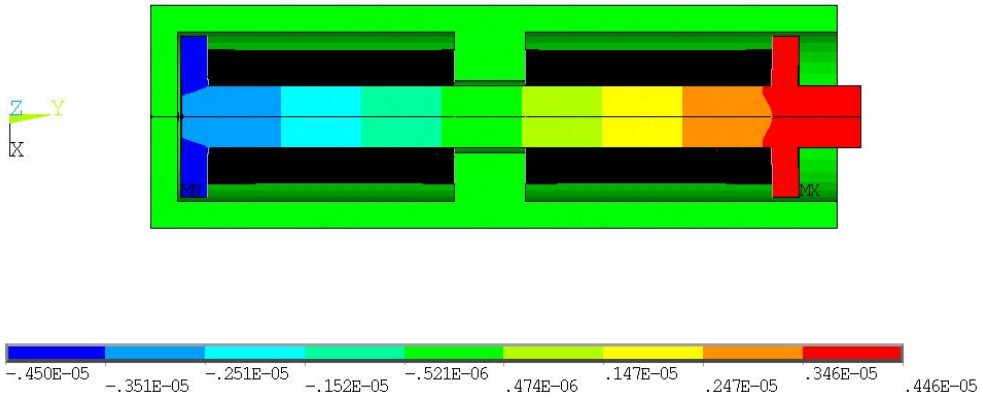

Figure 4.9 Y-component of displacement [m] generated by the dual-stack actuator in the neutral position

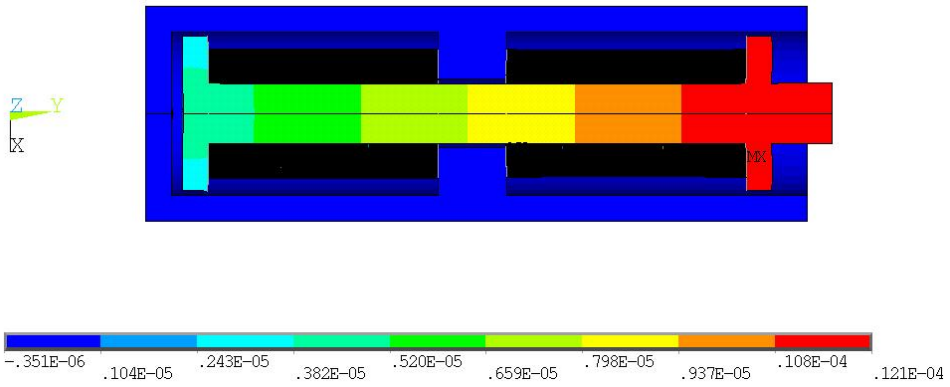

Figure 4.10 Y-component of displacement [m] generated by the dual-stack actuator in the extended position

The displacement values, in Table 4.7, are measured at the tip of the dual-stack actuator. Note that since the finite element model is built using 2-dimensional elements, no surface operations are performed to acquire the displacement values.

The actuator exhibits a positive displacement in the neutral position, as the piston is flexible and deforms. The displacements for the pulling and pushing actuations of the actuator are acquired by calculating the difference between the contracted and neutral position, and the extended and neutral position. Table 4.7 demonstrates that the pulling and pushing actuations generated by the dual-stack actuator are identical. Therefore, the actuator must be in its initial neutral position before an equal pulling and pushing actuation can be performed.

By adding the generated pulling and pushing displacement values of Table 4.7 together, a value of 16.10E^{-6} m is obtained. Comparing this value with the displacement value of a single piezoelectric stack, described in Table 4.3, demonstrates that the total free displacement generated by the dual-stack actuator is almost identical to the free displacement of a single piezoelectric stack.

4.3.4 Blocked Force Results of the Dual-Stack Actuator

The blocked force of the dual-stack actuator, for the contraction direction, is identified according to the procedure described in Section 2.2.5. To reiterate, the left side of the actuator is constrained in all directions and an electrical field of $V_1 = 100$ V, $V_2 = 0$ V, is applied to Stack 1 and Stack 2, respectively, causing the dual-stack actuator to contract. A pulling force of increasing magnitude is then applied to the tip of the actuator, illustrated by Figure 4.1, until the actuator reaches its neutral position at which point the pulling force is equivalent to the blocked contracting force. The reverse procedure is performed to identify the blocked extending force, where an electrical field of $V_1 = 0$ V, $V_2 = 100$ V is applied to Stack 1 and Stack 2, respectively. An increasing compression force is then applied to the tip of the actuator until it reaches the neutral position, at which point the compression force is equal to the blocked expansion force.

Figure 4.11 illustrates the FEM-computed force versus displacement chart of the dual-stack actuator.

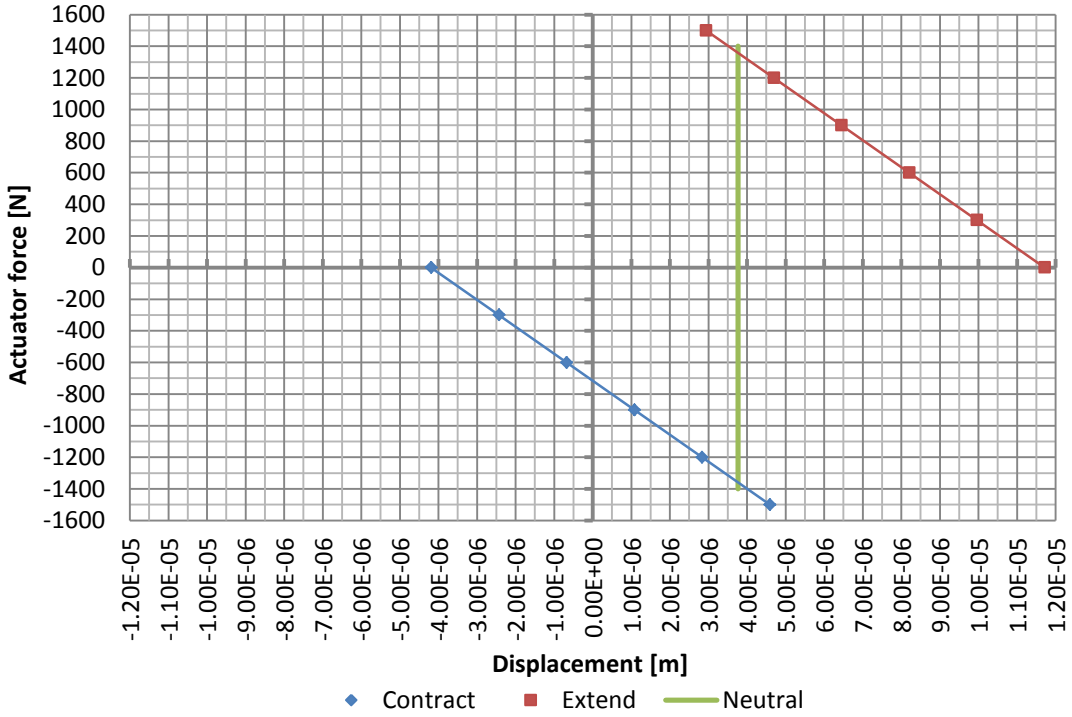

Figure 4.11 Force vs. displacement chart of the dual-stack actuator

The X-axis represents the displacement generated by the actuator, whereas the Y-axis represents the force that the actuator is able to generate, belonging to a certain displacement. The vertical line plotted in the graph is the displacement generated by the actuator in the neutral position. The points, where the contracting and extending data lines intersect the vertical displacement line, represent the blocked force of the actuator. The points, where the contracted and extended data lines intersect the X-axis, represent the free displacement values generated by the dual-stack actuator.

To calculate the relationship between the free displacement and blocked force values of the dual-stack actuator a linear regression fit is performed, which results in the following regression equations:

$$y_{con} = -1.71\mathrm{E}^{8}x - 714.75\,, \tag{4.12}$$

and

$$y_{ext} = -1.71\mathrm{E}^{8}x + 2002.41\,. \tag{4.13}$$

Equation (4.12) calculates the force for a given displacement value when the dual-stack actuator contracts. Whereas (4.13) calculates the force for a given displacement value, when the dual-stack actuator extends. The blocked force values are calculated by using the displacement generated by the dual-stack actuator in the neutral position as an input in (4.12) and (4.13). The calculated blocked force values of the actuator are described in Table 4.8.

The blocked forces generated by the dual-stack actuator for pulling and pushing actuations are almost identical and differ by 0.9%. However, a large amount of force is lost during the transfer of the force generated by the piezoelectric stack to the tip of the actuator, when the blocked force of the dual-stack actuator is compared against the blocked force of a single piezoelectric stack, which is described in Table 4.4.

Figure 4.12 and Figure 4.13 illustrate a plot of the von Mises stress, experienced by the actuator, when the actuator is forced to its neutral position. The maximum stress occurs in the corners where the plungers connect to the piston and therefore deform, resulting in a loss of force. The maximum von Mises stress has a value of $117E^6$ Pa in the extended position and $90.5E^6$ Pa in the contracted position. The yield strength of stainless steel 304 is $205E^6$ Pa [67] and is well above the maximum von Mises stress, hence the actuator does not incur fatigue.

A big difference occurs when the blocked force values, described in Table 4.8, are compared to (4.7), which states that the blocked force of the dual-stack actuator is twice the blocked force of a single stack actuator. The reason for this difference is that Heverly *et al.* [41] derived the equation by assuming that the blocked force is equal to the difference between the extended and contracted position and therefore compressing the piezoelectric stack past its neutral point. However, the conventional way of measuring the blocked force is to constrain the stack to zero or, in the case of the dual-stack actuator, the neutral position. In addition, Heverly *et al.* [41] assumed that the piston is infinitely rigid, and therefore no losses occur. However, the results of the FEM analysis demonstrate that there are losses generated, caused by the elasticity of the piston within the dual-stack actuator.

Pulling force [N]	Pushing force [N]
−1353	1365

Table 4.8 FEM-computed blocked force values [N] generated by the dual-stack actuator

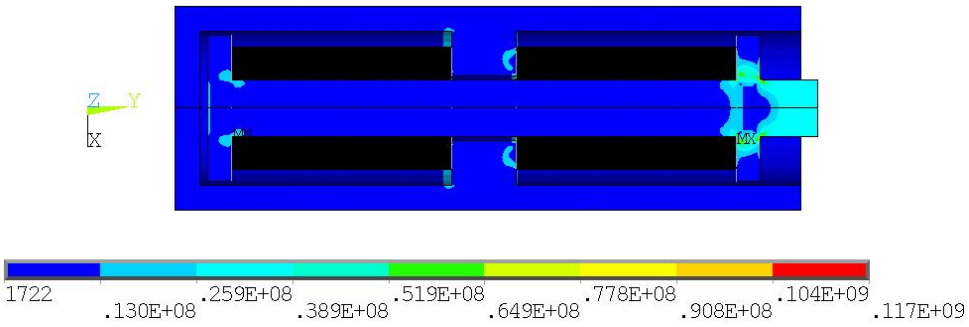

Figure 4.12 Generated von Mises stress [Pa] when the dual-stack actuator extends

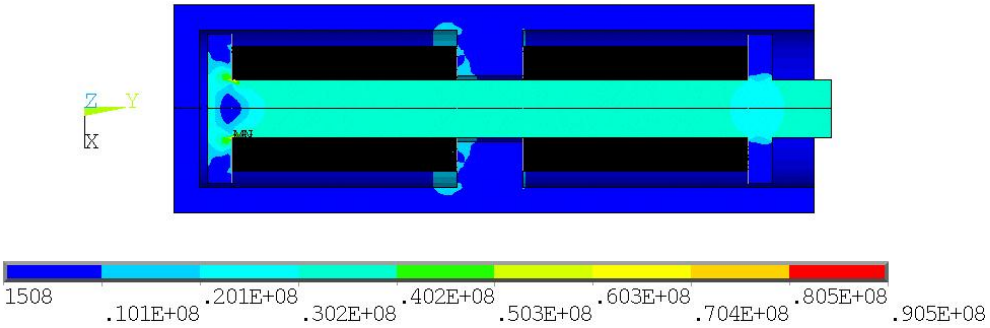

Figure 4.13 Generated von Mises stress [Pa] when the dual-stack actuator contracts

4.4 Analysis of the Amplified Dual-Stack Actuator

In Section 4.3, the displacements and blocked forces generated by the dual-stack actuator are theoretically calculated and simulated. The actuator exhibits a free displacement of $8.05E^{-6}$ m in the contracting and extending directions. One solution in order to achieve larger displacements is to increase the size of the piezoelectric stacks employed in the actuator. However, piezoelectric stacks are high in cost price and, if weight and space are a problem, this is not the ideal solution. The alternative

is to place the actuator in an amplifying compliant structure. This section describes the development of a finite element model of the amplified dual-stack actuator (ADSA), which combines an amplifying compliant structure with the dual-stack actuator, to amplify the displacements. The behaviour, free displacements, and blocked forces are identified and discussed.

4.4.1 Geometry and Finite Element Model of the ADSA

Figure 4.14 and Table 4.9 illustrate the geometry and dimensions belonging to the compliant structure. The top and the bottom of the compliant structure, denoted by fr_l_2, are the output surfaces that can be connected to an external load. The left and right sides of the actuator, represented by fr_h_2, must be free from any constraints so that the compliant structure is able to expand or contract. The dimensions of the frame, to calculate the amplification factor and displacement at the output area, are specified in Figure 4.14. The estimated amplified displacement is calculated using (3.3) and has a value of:

$$\delta = 13\mathrm{E}^{-3} - \sqrt{(13\mathrm{E}^{-3})^2 - 2 * 4\mathrm{E}^{-6} * 30.8\mathrm{E}^{-3} - (4\mathrm{E}^{-6})^2} = 9.48\mathrm{E}^{-6}\ \mathrm{m}\,. \tag{4.14}$$

Note that this is the displacement for one quarter. However, the displacement occurs at the top and bottom output surfaces of the compliant structure and therefore has a value of $18.96\mathrm{E}^{-6}$ m. The estimated amplification factor is calculated using (3.4) and has a value of:

$$r = \frac{9.48\mathrm{E}^{-6}}{4\mathrm{E}^{-6}} = 2.37\,. \tag{4.15}$$

A new finite element model is built since the compliant structure does not exhibit axisymmetric properties. Hence, the generated model is a full 3-dimensional model of the dual-stack actuator and the compliant structure.

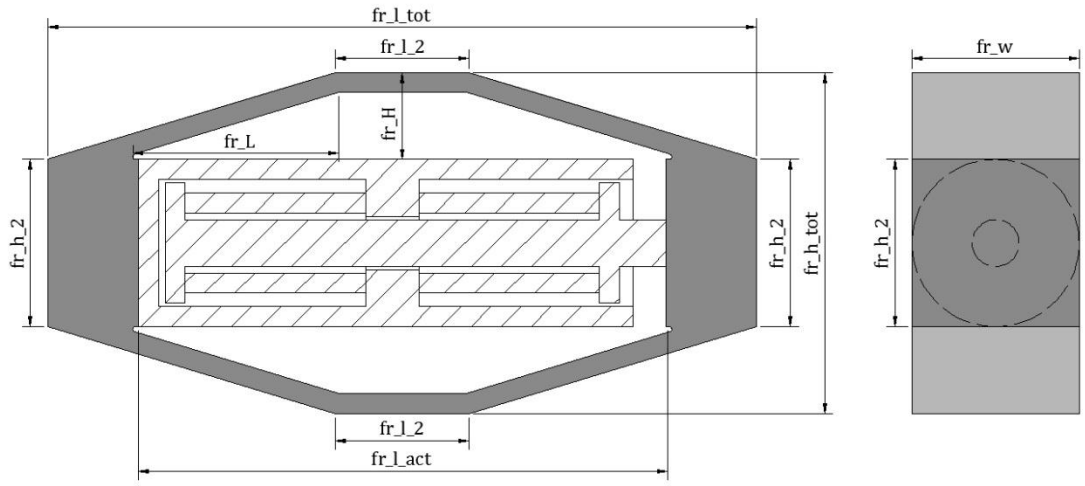

Figure 4.14 Geometry of the ADSA

Parameter	Description	Value [m]
fr_l_tot	Total length of the ADSA	$106.0E^{-3}$
fr_w	Total width of the ADSA	$25.0E^{-3}$
fr_h_tot	Total height of the ADSA	$51.0E^{-3}$
fr_l_act	Space to mount the dual-stack actuator	$79.0E^{-3}$
fr_l_2	Length of the output surface	$20.0E^{-3}$
fr_h_2	Height of the mounting area for the dual-stack actuator	$25.0E^{-3}$
fr_L	Length to calculate amplification factor	$30.8E^{-3}$
fr_H	Height to calculate amplification factor	$13.0E^{-3}$

Table 4.9 Parameters and dimensions of the ADSA

An APDL input file is generated to build the model in ANSYS. The actuator is modelled using the 3-dimensional element type SOLID226, where KEYOPT(1) is set to 1001 to perform a piezoelectric analysis. The model consists of two piezoelectric stacks that each contain 262 single piezoelectric elements. A total of 524 single piezoelectric elements that exhibit a thickness of $0.1E^{-3}$ m are used in the analysis, which causes a real meshing challenge since the piezoelectric elements are thin and circular in shape. When the model is meshed with the automatic size control enabled, elements with a size of $0.1E^{-3}$ m are generated. Therefore, each piezoelectric ring in the stack contains roughly 11,000 elements. This results in a model that is too

computationally demanding. To control the amount of elements and nodes in the generated finite element model, half of the height of the ADSA is built. The command LESIZE is executed to control the amount of elements generated on each line of the piezoelectric elements. The dual-stack actuator is then meshed using the VSWEEP command, whereas the compliant structure is meshed using the free-mesher with smart sizing enabled.

The housing and piston of the dual-stack actuator and the compliant structure are modelled out of stainless steel 304. The piezoelectric stacks are identical to those employed in the previous analysis conducted in Section 4.3.1 and are of the type HPst 150/14–10/25. The material properties used in the analysis are specified in Appendix A.

The command VSYMM is then executed, which reflects half the actuator about the Y-axis to generate a full finite element model of the ADSA, where the nodes that are generated on the same location are merged by executing the command NUMMRG. This is a crucial step, since all the nodes that lie on the ZX-plane are doubled, as illustrated by Figure 4.15, which shows the full 3-D model of the ADSA. Two extra MPC-contact points are generated to bond the dual-stack actuator to the compliant structure. Relevant information of the generated finite element model is described in Table 4.10.

Number of elements	83,670
Number of nodes	337,964
Analysis type	Small Displacement Static
Mass	467.80 g

Table 4.10 Finite element model information of the ADSA

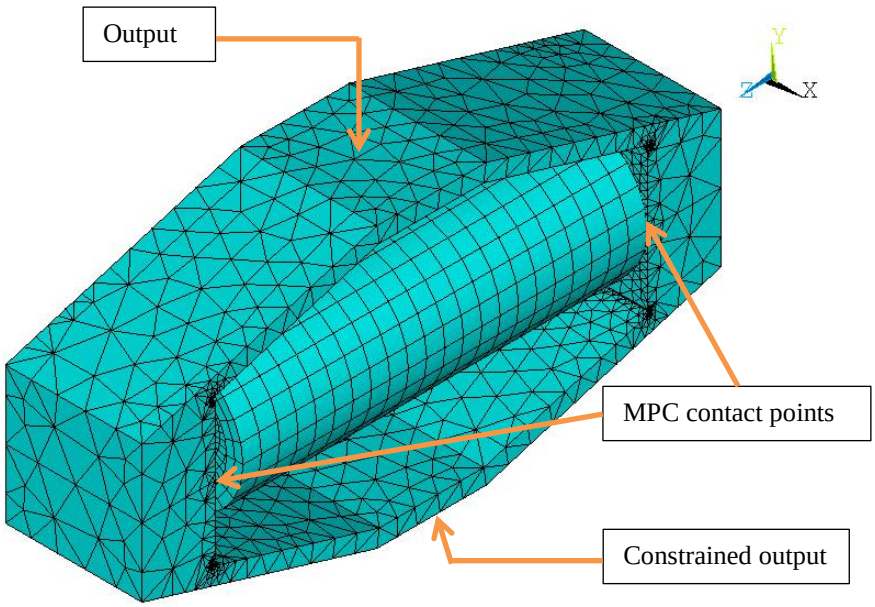

Figure 4.15 Generated finite element model of the ADSA

Table 4.10 demonstrates that the weight of the actuator is doubled since the compliant structure is modelled out of the relatively heavy material, stainless steel 304. Depending on the application, it may be possible to change the material of the compliant structure to a more advanced composite material.

In order to identify the free displacements and blocked forces of the ADSA, one output, illustrated in Figure 4.15, is constrained in all directions. The model is solved for the free displacement in three phases to identify the contracted, neutral and expanded displacement values.

4.4.2 Free Displacement Results of the ADSA

The free displacement values are obtained using the method described in Section 2.2.4. A surface is created at the unconstrained output of the ADSA, which is illustrated by Figure 4.15. The Y-component of displacement is then mapped onto the surface and the average value is calculated.

Figure 4.16 illustrates the generated Y-component of displacement by the ADSA. In this phase, an electrical field of 0 V is applied to Stack 1 and 100 V to Stack 2. This results in an extension of the dual-stack actuator, which causes the frame to contract with $-28.29E^{-6}$ m. The Y-component of displacement in the neutral position is illustrated in Figure 4.17, where an electrical field of 50 V is applied to both stacks. Simulations of the dual-stack actuator, remaining in its neutral position, demonstrate that the actuator exhibits a small extension, as illustrated by Figure 4.9. This extension is amplified by the compliant structure, resulting in a contraction of $-9.09E^{-6}$ m. In the final solution phase, an electrical field of 100 V is applied to Stack 1, and 0 V to Stack 2. The Y-component of displacement generated by the ADSA is illustrated in Figure 4.18, which shows an expansion of the compliant structure of $10.11E^{-6}$ m.

An overview of the displacement values is given by Table 4.11. The generated pulling actuation is acquired by taking the difference between the contracted and neutral position. The generated pushing actuation is acquired by taking the difference between the expanded and neutral position. Both displacement values are simulated to be $19.2E^{-6}$ m in both directions.

The values are compared with the theoretically calculated displacement in (4.14), which has a value of $19.0E^{-6}$ m and demonstrates an error of $0.2E^{-6}$ m, which is 1%. The error in the estimated value is caused by the assumption that the flexing only occurs at the hinges. However, the simulation results demonstrate that the rest of the compliant structure also exhibits a slight flexing, which results in an error.

Contracted position [m]	**Neutral position [m]**	**Expanded position [m]**
$-28.29E^{-6}$	$-9.09E^{-6}$	$10.11E^{-6}$
Δ displacement		Δ displacement
$19.20E^{-6}$		$19.20E^{-6}$

Table 4.11 FEM-computed free displacements [m] generated by the ADSA

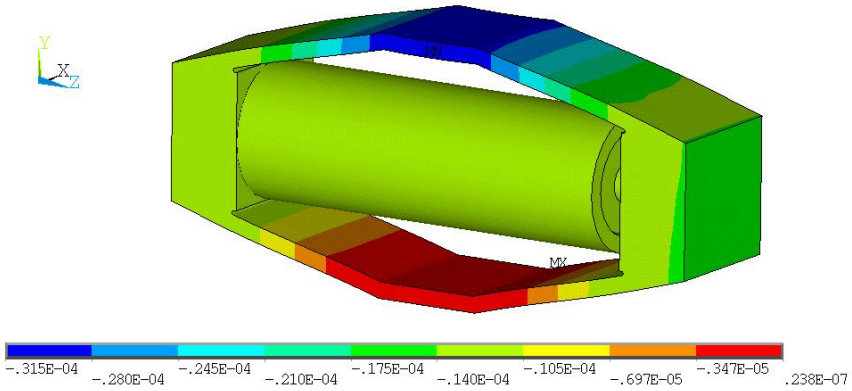

Figure 4.16 Y-component of displacement [m] generated by the ADSA in the contracted position

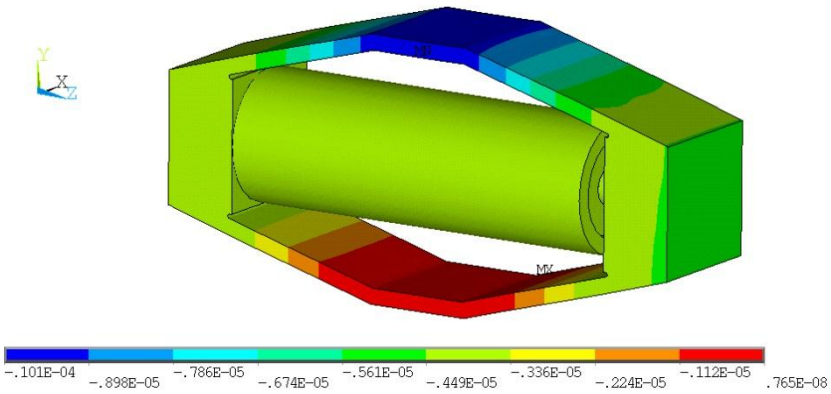

Figure 4.17 Y-component of displacement [m] generated by the ADSA in the neutral position

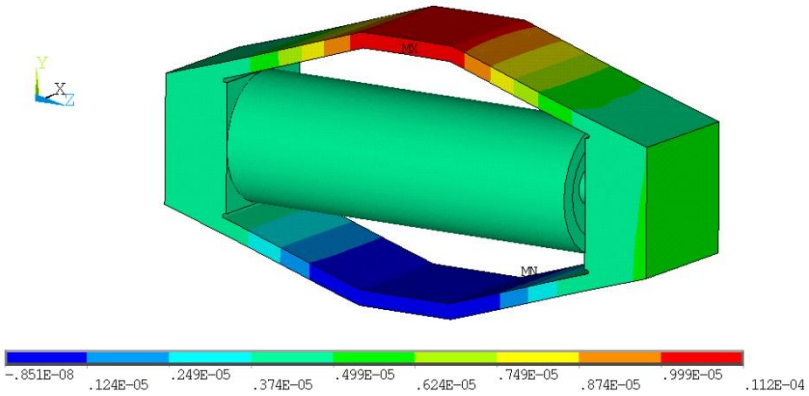

Figure 4.18 Y-component of displacement [m] generated by the ADSA in the expanded position

4.4.3 Blocked Force Results of the ADSA

The blocked force of the ADSA for the expansion direction is identified according to the procedure described in Section 2.2.5. One output is constrained in all directions, as illustrated in Figure 4.15, and an electrical field of $V_1 = 100$ V, $V_2 = 0$ V, is applied to Stack 1 and Stack 2, respectively, causing the ADSA to expand. A compression force of increasing magnitude is then applied to the unconstrained output, illustrated in Figure 4.15, until the ADSA reaches its neutral position, at which point the compression force is equivalent to the blocked expansion force. The reverse procedure is performed to identify the blocked contraction force, where an electrical field of $V_1 = 0$ V, $V_2 = 100$ V to Stack 1 and Stack 2, respectively. An increasing expansion force is then applied to the unconstrained output until it reaches the neutral position, at which point the expansion force is equal to the blocked contraction force.

The FEM-computed force versus displacement relationship is illustrated by Figure 4.19. The vertical line in the graph represents the displacement generated by the ADSA in the neutral position. This value is identical to the value of the neutral position described in Table 4.11. The points, where both contracting and expanding data lines intercept the vertical neutral displacement line, represent the blocked force of the ADSA. The points, where both contracting and expanding data lines intercept the X-axis, represent the free displacement value of the ADSA generated in the contracted and expanded positions, respectively. Both free displacement values are identical to the values described in Table 4.11.

To calculate the relationship between the free displacement and blocked force values of the ADSA, a linear regression fit is performed, which results in the following regression equations:

$$y_{con} = -1.23\mathrm{E}^{7}x - 347.44\,, \tag{4.16}$$

and

$$y_{exp} = -1.24\mathrm{E}^{7}x + 124.71\,. \tag{4.17}$$

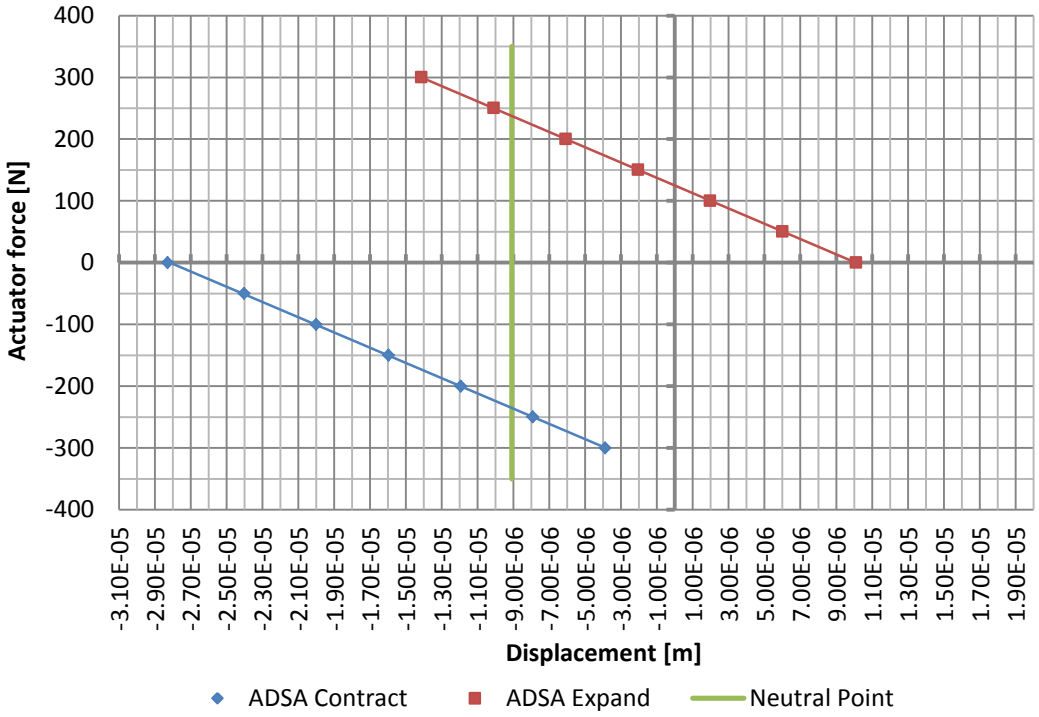

Figure 4.19 Force vs. displacement chart of the ADSA

The blocked forces generated by the ADSA are summarised by Table 4.12. Comparing these blocked force values with the blocked force values of the dual-stack actuator, described in Table 4.8, demonstrates that the blocked force is reduced significantly by 83%, which is caused by the compliant structure. This is a result of a decrease in total system stiffness, which is caused by adding the compliant structure to the dual-stack actuator. As a result, more displacement is generated, whereas the blocked force is reduced. Note that, when designing a piezoelectric actuator, there is always a trade-off between the generated force and displacement.

Pulling force [N]	Pushing force [N]
−236	237

Table 4.12 FEM-computed blocked force values [N] generated by the ADSA

4.5 Thermal Deformation Compensation Benchmark Model

In this section, a finite element benchmark model is built in order to compare the actuation performance of the ADSA. The finite element model contains a beam structure that is subjected to thermal loading, which employs two piezoelectric patches, one on each side of the structure, to compensate for the thermally induced deformation. The thermal loading is induced via film heaters on each side of the structure.

A similar method of compensation is applied in a study conducted by Song *et al.* [7] that uses four piezoelectric patches mounted on the bottom surface of a composite beam structure. Two film heaters are bonded on the top surface to induce the thermal loading. Another study conducted by Binette *et al.* [68] uses two Macro Fiber Composite (MFC) patches bonded on the top surface of a composite sandwich plate. The thermal loading was induced by a 750 W heating lamp that heated the bottom surface of the plate. In both studies, the actuators are able to compensate the thermally induced deformation successfully. However, the thermally induced deformation is only compensated in one direction, since the actuators are bonded to one surface of the structure.

In order to create a finite element benchmark model for the ADSA, which exhibits bidirectional actuation, two piezoelectric patches are employed, each bonded to one side of the beam structure. In this configuration, the top and bottom piezoelectric actuators are able to excite the beam structure in a downward and upward direction respectively. A structural-thermoelectric coupled-field analysis is conducted to identify the thermally induced deformation and the compensation performance of the piezoelectric patches.

4.5.1 Geometry and Finite Element Model of the Benchmark Structure

The geometry of the benchmark structure and configuration of the film heaters and piezoelectric patches are illustrated by Figure 4.20, whereas the dimensions belonging to the structure are described in Table 4.13. Two identical piezoelectric patches are placed at the left most side of the beam structure.

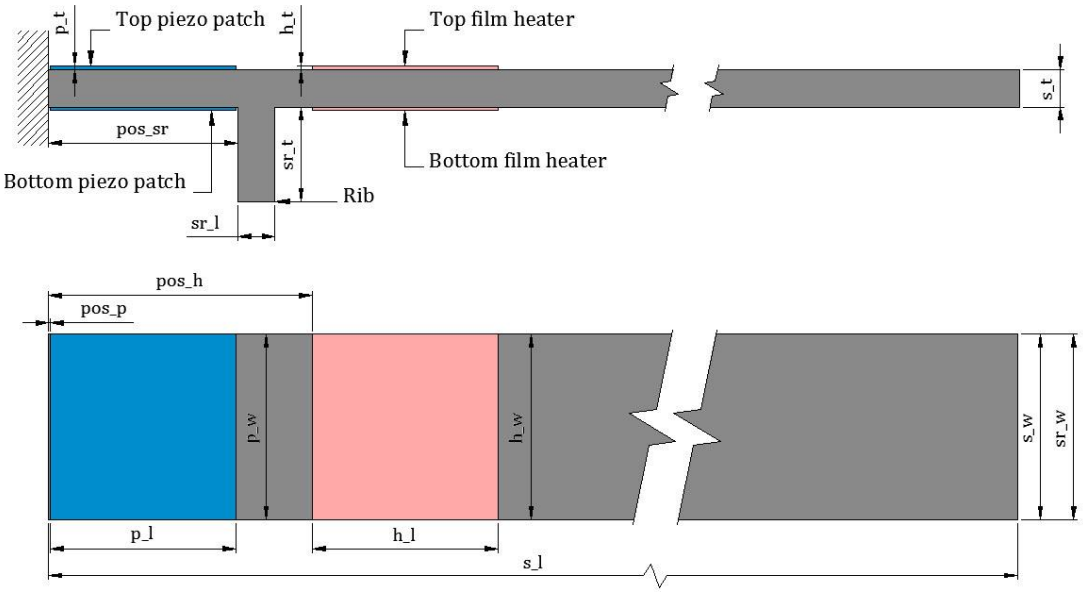

Figure 4.20 Geometry of the benchmark model

Parameter	Description	Value [m]
s_l	Length of beam structure	$800.0E^{-3}$
s_w	Width of beam structure	$50.0E^{-3}$
s_t	Thickness of beam structure	$10.0E^{-3}$
h_l	Length of film heaters	$50.0E^{-3}$
h_w	Width of film heaters	$50.0E^{-3}$
h_t	Thickness of film heaters	$0.2E^{-3}$
p_l	Length of piezoelectric patches	$50.0E^{-3}$
p_w	Width of piezoelectric patches	$50.0E^{-3}$
p_t	Thickness of piezoelectric patches	$0.3E^{-3}$
sr_l	Length of rib	$10.0E^{-3}$
sr_w	Width of rib	$50.0E^{-3}$
sr_t	Thickness of rib	$25.5E^{-3}$
pos_h	Position of film heaters	$71.0E^{-3}$
pos_p	Position of piezoelectric patches	$0.5E^{-3}$
pos_sr	Position of rib	$51.0E^{-3}$

Table 4.13 Parameters and dimensions of the benchmark model

The bottom side of the beam structure contains a rib, which serves as a mounting point for the ADSA, as shown in Figure 4.24. This rib is included in the benchmark model to make the comparison between both actuator configurations as accurate as possible. Therefore, the only difference in the analysis is the actuator. Two identical film heaters are bonded on each side of the beam structure to induce a through-the-thickness thermal difference, where the structure deforms upwards when the bottom film heater generates more heat than the top heater and conversely deforms downwards when the top film heater generates more heat than the bottom heater.

The beam structure is modelled out of aluminium alloy T6 6061 material, whereas the piezoelectric patches are modelled using identical material properties as the piezoelectric material used in the ADSA. The material properties for the film heaters, piezoelectric patches, and beam structure are described in Appendix A. The benchmark model is built using the 3-dimensional SOLID226 element type, with KEYOPT(1) set to 1011, to conduct a structural-thermoelectric coupled-field analysis. The beam structure is meshed with tetrahedral-shaped elements that exhibit a size of $5E^{-3}$ m, whereas the film heaters and piezoelectric patches are meshed out of $2E^{-3}$ m hexahedral-shaped elements, as illustrated by Figure 4.21.

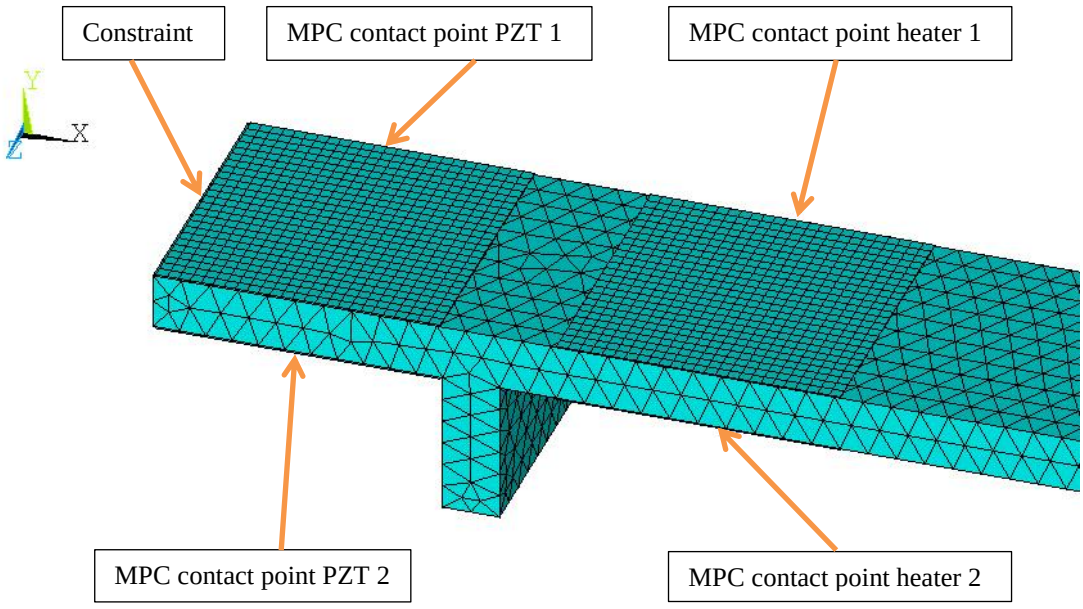

Figure 4.21 Partial view of the generated finite element benchmark model

All nodes located on the far left side of the model are constrained in all directions, and the piezoelectric patches and film heaters are bonded to the beam structure using the MPC-contact algorithm.

The model is solved in six phases, with different load conditions in each phase, described in Table 4.14, where P_{top} and H_{top} are the top piezoelectric patch and film heater, respectively. The piezoelectric patch and film heater bonded on the bottom side of the structure are denoted by P_{bot} and H_{bot}, respectively. In the first three phases, the benchmark model is solved for a thermal loading that causes the beam structure to deflect upward. In the last three phases, the model is solved for a thermal loading, which deflects the beam in a downward direction. In Phases 1 and 4, only thermal loads are applied to the model to identify the thermal deformation. The actuation displacement, generated by the piezoelectric patches, is identified in Phases 2 and 5, where only electrical loads are applied to the model. In Phases 3 and 6, both thermal and electrical loads are applied to the model to identify the amount of compensation achieved by the piezoelectric patches.

A convection coefficient to air of 5 W/(m^2·°C) is applied to the beam structure and the reference temperature is set to 22 °C. The film heaters are set at a fixed temperature of 50 °C and 45 °C. In a practical experiment, this is achieved by a temperature controller, which controls the temperature of the film heater to a pre-defined set-point. The electrical fields applied to the piezoelectric patches are identical in field strength as the electrical fields applied to the ADSA and hold a value of either 100 V or 0 V.

When all six phases are simulated, the Y-component of displacement is acquired, since this is the direction where the deformation occurs, as illustrated by Figure 4.21. The PATH operation is executed, which creates a path on the top surface across the structure. The Y-component of displacement is then interpolated onto the path, which contains 200 data points. This method allows the data to be listed, manipulated, and exported for any further post-processing purposes. The amount of nodes and elements generated in the benchmark model are described in Table 4.15.

Phase 1	1. Apply electrical field, $P_{top} = P_{bot} = 0$ V, 2. Apply temperature, $H_{top} = 45$ °C , $H_{bot} = 50$ °C, 3. Apply a convection coefficient to air of 5 W/(m^2·°C), 4. Set reference temperature to 22 °C, 5. Solve and save solution results.
Phase 2	6. Delete temperature load at H_{top} and H_{bot} , 7. Apply electrical field, $P_{top} = 100$ V, $P_{bot} = 0$ V, 8. Solve and save solution results.
Phase 3	9. Apply temperature, $H_{top} = 45$ °C , $H_{bot} = 50$ °C, 10. Apply electrical field, $P_{top} = 100$ V, $P_{bot} = 0$ V, 11. Solve and save solution results.
Phase 4	12. Apply electrical field, $P_{top} = P_{bot} = 0$ V, 13. Apply temperature, $H_{top} = 50$ °C , $H_{bot} = 45$ °C, 14. Solve and save solution results.
Phase 5	15. Delete temperature load at H_{top} and H_{bot} , 16. Apply electrical field, $P_{top} = 0$ V, $P_{bot} = 100$ V, 17. Solve and save solution results.
Phase 6	18. Apply temperature, $H_{top} = 50$ °C , $H_{bot} = 45$ °C, 19. Apply electrical field, $P_{top} = 0$ V, $P_{bot} = 100$ V, 20. Solve and save solution results.

Table 4.14 Applied loads and solution process of the benchmark model

Number of elements	24,233
Number of nodes	53,499
Analysis type	Small Displacement Static
Total mass	1116 g

Table 4.15 Finite element information of the benchmark model

4.5.2 Post-Processing the Solution Results of the Benchmark Structure

All six phases, as described in Table 4.14, are simulated and the data is acquired and plotted in two graphs. The Y-component of displacement, illustrated by Figure 4.22, is obtained from the data generated by the first three solution phases, where the beam structure deforms in an upward direction, caused by the thermal loading. The dotted red line, blue dashed line, and solid green line represent the thermal deformation, piezoelectric actuation and compensated displacement, respectively. The maximum displacement generated by the thermal loading has a value of $434E^{-6}$ m, whereas the maximum displacement that the piezoelectric patch is capable of generating is simulated to be $-45.3E^{-6}$ m, which is only a fraction compared to the displacement generated by the thermal loading. Hence, the compensated beam exhibits a displacement value of $389E^{-6}$ m, which results in a compensation of 10.43%.

Figure 4.23 illustrates the Y-component of displacement acquired from the data generated by the last three solution phases. The structure demonstrates a deformation in the downward direction, which is caused by the thermal loading. The dotted red line represents the displacement generated by the thermal loading and has a maximum value of $-391E^{-6}$ m. The dashed blue line represents the displacement generated by the bottom piezoelectric patch, which has a maximum value of $41.9E^{-6}$ m. The compensated displacement of the structure is represented by the solid green line and has a maximum value of $-349E^{-6}$ m. Hence, the compensation performance is 10.73%.

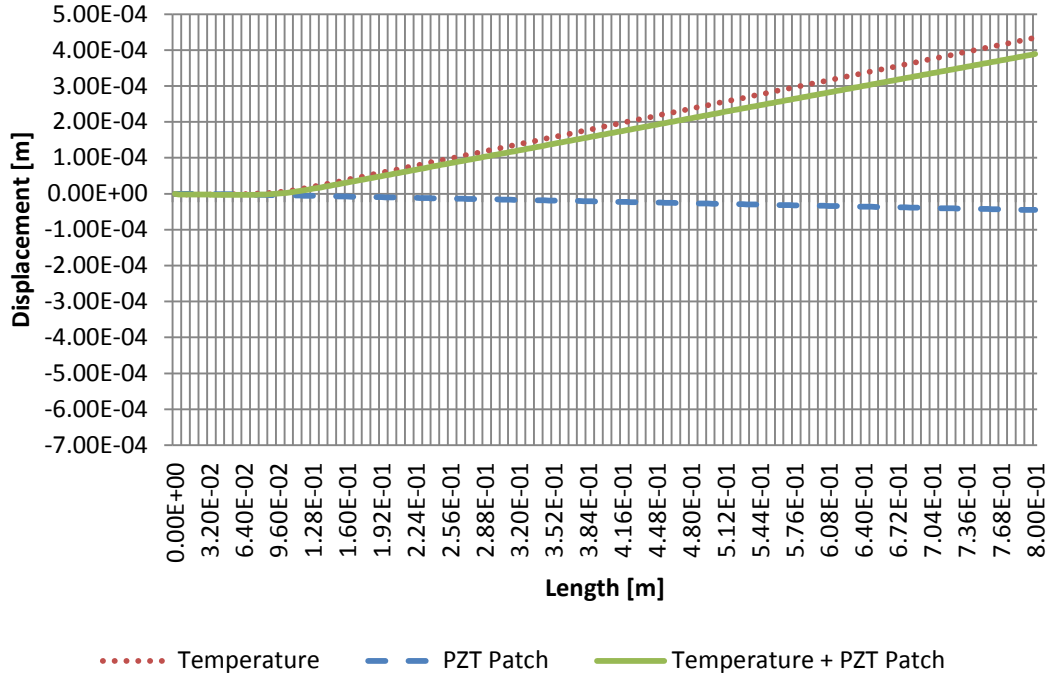

Figure 4.22 Y-component of displacement exhibited by the benchmark structure for the solution Phases 1, 2 and 3, described in Table 4.14

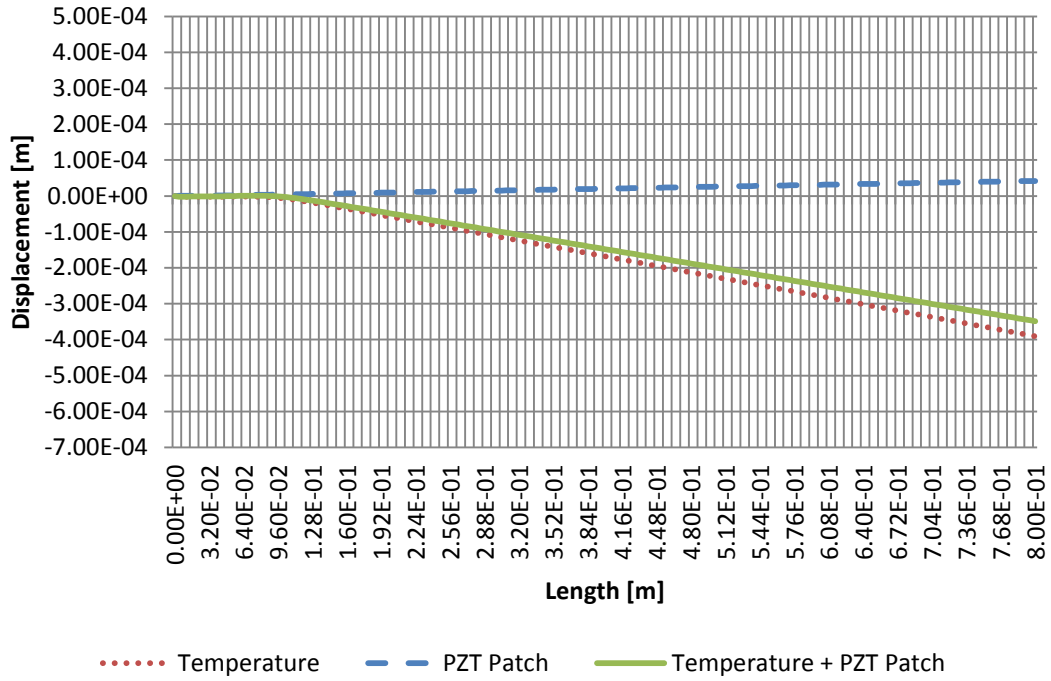

Figure 4.23 Y-component of displacement exhibited by the benchmark structure for the solution Phases 4, 5 and 6, described in Table 4.14

A summary of the compensation data of the benchmark structure, using two piezoelectric patches to compensate for the induced thermal loading, is described in Table 4.16. This table demonstrates that with the current configuration of the piezoelectric patches used in the benchmark model the compensation is not sufficient. The limiting factor might be the insufficient bending moment created by the piezoelectric patch, since the blocked force of a single piezoelectric stack is relatively high. Therefore, one solution to acquire more bending moment is by increasing the amount of piezoelectric patches, or the applied electric field strength.

However, a bigger limitation of employing piezoelectric patches is their ability to compensate for only one direction. Therefore, patches must be bonded to the top and bottom surfaces of the structure, which in certain applications is not desirable. In the hypersonic area, for example, it is not desired to mount piezoelectric patches onto the outside surface of the skin of the vehicle, since this disturbs the hypersonic airstream and directly subjects the patches to the thermal loading induced by the friction of the hypersonic airstream, which results in loss of actuation performance.

This chapter continues by substituting the piezoelectric patches in the benchmark model, with the ADSA, in order to identify its compensation performance.

Structure demonstrates upward deformation caused by thermal loading		
Thermal displacement [m]	Compensated displacement [m]	Compensation percentage
$434E^{-6}$	$389E^{-6}$	10.43%

(a)

Structure demonstrates downward deformation caused by thermal loading		
Thermal displacement [m]	Compensated displacement [m]	Compensation percentage
$-391E^{-6}$	$-349E^{-6}$	10.73%

(b)

Table 4.16 (a) Compensation results where structure deflects upward [m]; (b) Compensation results where structure deflects downward [m]

4.6 Thermal Deformation Compensation Performance of the ADSA

The aim of this section is to identify the compensation performance of the ADSA by mounting the actuator to a beam structure, identical to the benchmark model. The geometry of the beam structure and the configuration of the ADSA are illustrated by Figure 4.24, whereas Table 4.17 describes the dimensions and parameters belonging to the finite element model. The two piezoelectric patches are removed from the benchmark model and replaced by the ADSA. Therefore, the only alteration made to the finite element model is the change of actuator. One output of the ADSA is fixed to the rib of the beam structure, whereas, the other end is constrained in all directions.

The beam structure and ADSA are modelled out of material aluminium alloy T6 6061 and stainless steel 304, respectively. The material properties employed in the analysis are described in Appendix A. Since the finite element model of the ADSA is already built and analysed and possesses a larger amount of nodes and elements, compared to the benchmark model, it is expanded with the beam structure and film heaters. The entire model is built using the 3-dimensional SOLID226 element type, with KEYOPT(1) set to 1011, to perform a structural-thermoelectric coupled-field analysis. The element size and shape for the beam structure and film heaters are $5E^{-3}$ m tetrahedral and $2E^{-3}$ m hexahedral elements, respectively.

The model is solved by applying the loads in six phases, as described in Table 4.18, where V_1 and V_2 represent the voltages applied to Stack 1 and Stack 2 of the ADSA, illustrated by Figure 4.1. The top film heater is denoted by H_{top}, and the film heater bonded to the bottom surface of the beam structure is denoted by H_{bot}. The first three phases simulate and identify the compensation of the beam structure, when it demonstrates a deformation in the upward direction, caused by the thermal loading. The last three phases identify the achieved compensation by the ADSA, when the beam structure demonstrates a deformation in the downward direction. Phases 1 and 4 simulate the beam structure under thermal loading to identify the thermal deformation.

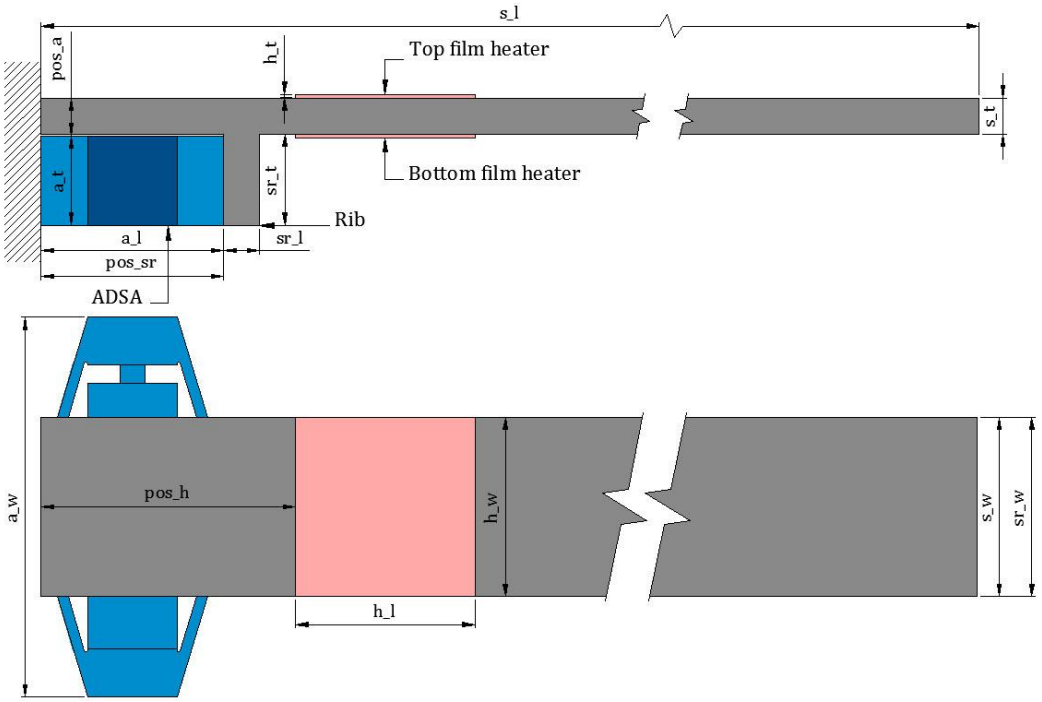

Figure 4.24 Geometry of the beam structure and ADSA

Parameter	Description	Value [m]
s_l	Length of the beam structure	$800.0E^{-3}$
s_w	Width of the beam structure	$50.0E^{-3}$
s_t	Thickness of the beam structure	$10.0E^{-3}$
h_l	Length of the film heaters	$50.0E^{-3}$
h_w	Width of the film heaters	$50.0E^{-3}$
h_t	Thickness of the film heaters	$0.2E^{-3}$
a_l	Length of the ADSA	$51.0E^{-3}$
a_w	Width of the ADSA	$106.0E^{-3}$
a_t	Thickness of the ADSA	$25.0E^{-3}$
sr_l	Length of the rib	$10.0E^{-3}$
sr_w	Width of the rib	$50.0E^{-3}$
sr_t	Thickness of the rib	$25.5E^{-3}$
pos_h	Position of the film heaters	$71.0E^{-3}$
pos_a	Position of the ADSA	$10.5E^{-3}$
pos_sr	Position of the rib	$51.0E^{-3}$

Table 4.17 Parameters and dimensions of the beam structure and ADSA

Phase 1	1. Apply electrical field, $V_1 = V_2 = 0$ V, 2. Apply temperature, $H_{top} = 45$ °C, $H_{bot} = 50$ °C, 3. Apply a convection coefficient to air of 5 W/(m^2·°C), 4. Set reference temperature to 22 °C, 5. Solve and save solution results.
Phase 2	6. Delete temperature load at H_{top} and H_{bot} , 7. Apply electrical field, $V_1 = 0$ V, $V_2 = 100$ V, 8. Solve and save solution results.
Phase 3	9. Apply temperature, $H_{top} = 45$ °C, $H_{bot} = 50$ °C, 10. Apply electrical field, $V_1 = 0$ V, $V_2 = 100$ V, 11. Solve and save solution results.
Phase 4	12. Apply electrical field, $V_1 = V_2 = 0$ V, 13. Apply temperature, $H_{top} = 50$ °C, $H_{bot} = 45$ °C, 14. Solve and save solution results.
Phase 5	15. Delete temperature load at H_{top} and H_{bot} , 16. Apply electrical field, $V_1 = 100$ V, $V_2 = 0$ V, 17. Solve and save solution results.
Phase 6	18. Apply temperature, $H_{top} = 50$ °C, $H_{bot} = 45$ °C, 19. Apply electrical field, $V_1 = 100$ V, $V_2 = 0$ V, 20. Solve and save solution results.

Table 4.18 Applied loads and solution process of the beam structure and ADSA

Phases 2 and 5 then simulate the beam structure, where only the ADSA is activated, to identify the generated displacement by the actuator. In the final Phases, 3 and 6, the finite element model is solved for thermal and electrical loading, to identify the displacement of the compensated beam structure. Therefore, both the ADSA and the film heaters are activated. After solving each phase, the solution information is written to a database file for post-processing purposes. A summary of the generated nodes and elements of the finite element model is described in Table 4.19. Figure 4.25 illustrates a partial view of the generated model, together with the positions of the MPC contact points, where the far left side of the model is constrained in all directions.

Number of elements	105,187
Number of nodes	380,985
Analysis type	Small Displacement Static
Total mass	1584 g

Table 4.19 Finite element model information of the beam structure and ADSA

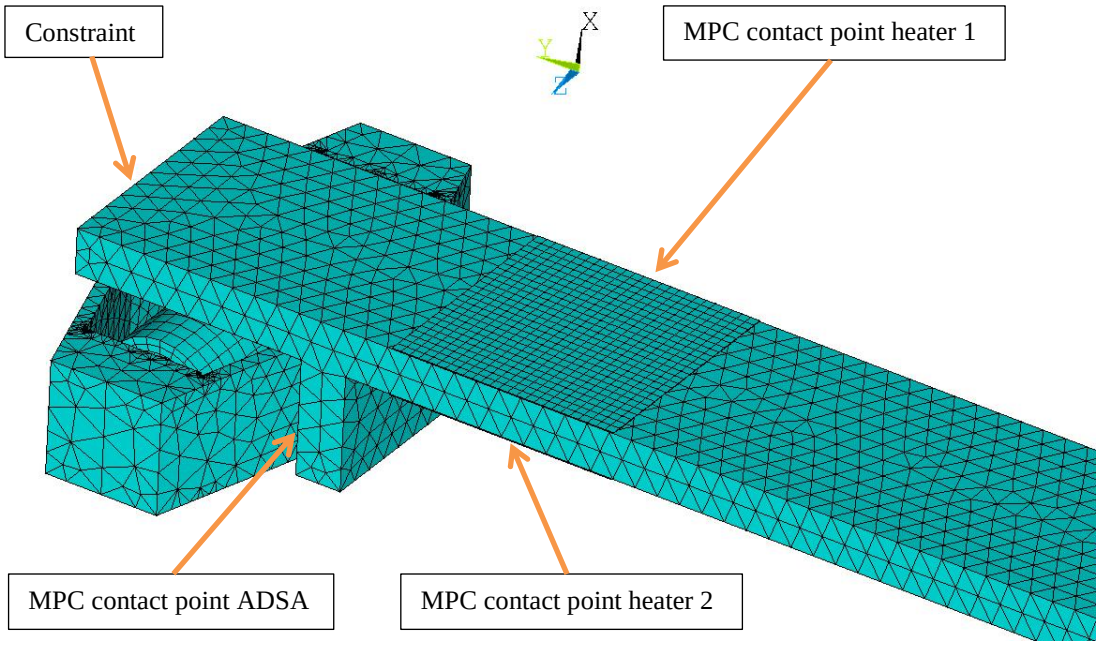

Figure 4.25 Partial view of the generated finite element model of the beam structure and ADSA

4.6.1 Post-Processing the Solution Results of the ADSA Structure

The X-component of displacement is mapped onto the beam structure by executing the PATH operation. In this simulation, the X-component of displacement is the displacement of interest, since this is the direction the beam structure deforms, as illustrated by the Cartesian coordinate system in Figure 4.25. This command generates a path across the top surface of the beam, which contains 200 data points, where each data point represents a displacement value.

The solution information of the X-component of displacement generated by the first three phases is plotted in a graph, illustrated by Figure 4.26. In these phases, the compensation performance of the ADSA is identified, when the beam structure deflects upward, which is caused by the thermal loading. The dotted red line in the graph represents the solution information of Phase 1, where only thermal loads are applied to the beam structure. The structure exhibits a maximum displacement of $351E^{-6}$ m. The dashed blue line represents the displacement of the beam structure when only electrical loads are applied, simulated in Phase 2. This is the displacement generated by the ADSA and has a maximum value of $-429E^{-6}$ m. The compensated profile of the beam, simulated in Phase 3, is represented by the solid green line in Figure 4.26 and has a maximum displacement value of $-78.2E^{-6}$ m. This indicates that the shape beam structure is over-compensated.

Figure 4.27 represents the X-component of displacement of the beam structure, which deforms in a downward direction, caused by the thermal loading. The dotted red line, dashed blue line and solid green line represent the displacement generated by the thermal loading, the displacement generated by the ADSA and the compensated displacement, respectively. The structure exhibits a maximum displacement of $-529E^{-6}$ m, caused by the thermal loading, which is simulated in Phase 4. The generated displacement by the ADSA is simulated in Phase 5 and has a value of $153E^{-6}$ m. The maximum displacement that occurs, when the beam structure is compensated for the thermal deformation, is simulated in Phase 6 and has a value of $-376E^{-6}$ m. A summary of the compensation values is given in Table 4.20.

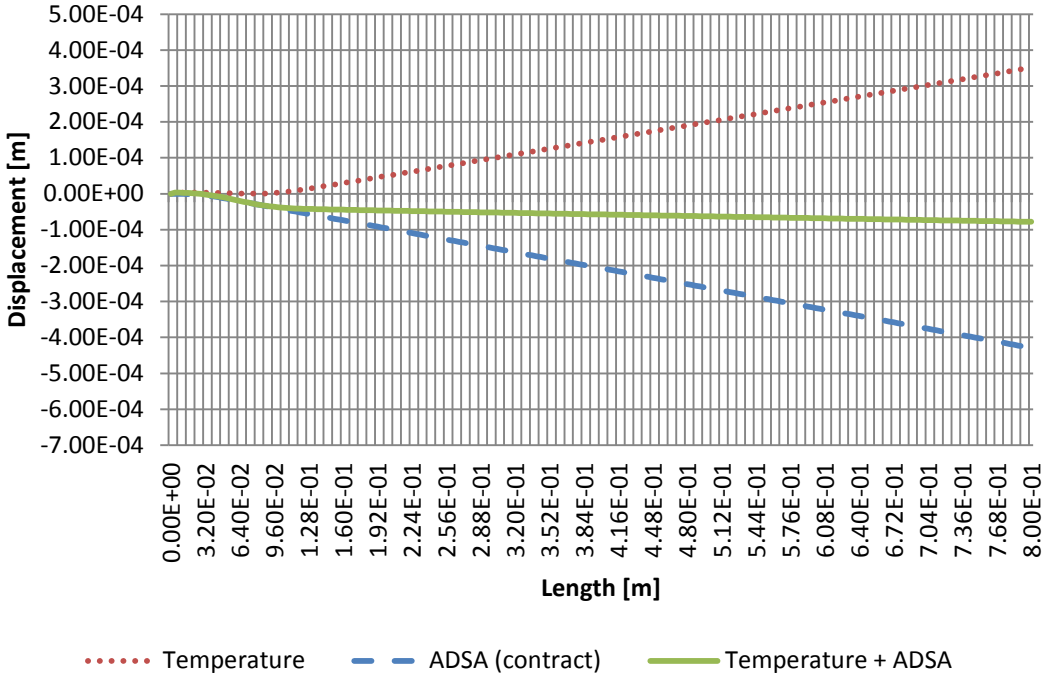

Figure 4.26 X-component of displacement exhibited by the ADSA structure for the solution Phases 1, 2 and 3, described in Table 4.18

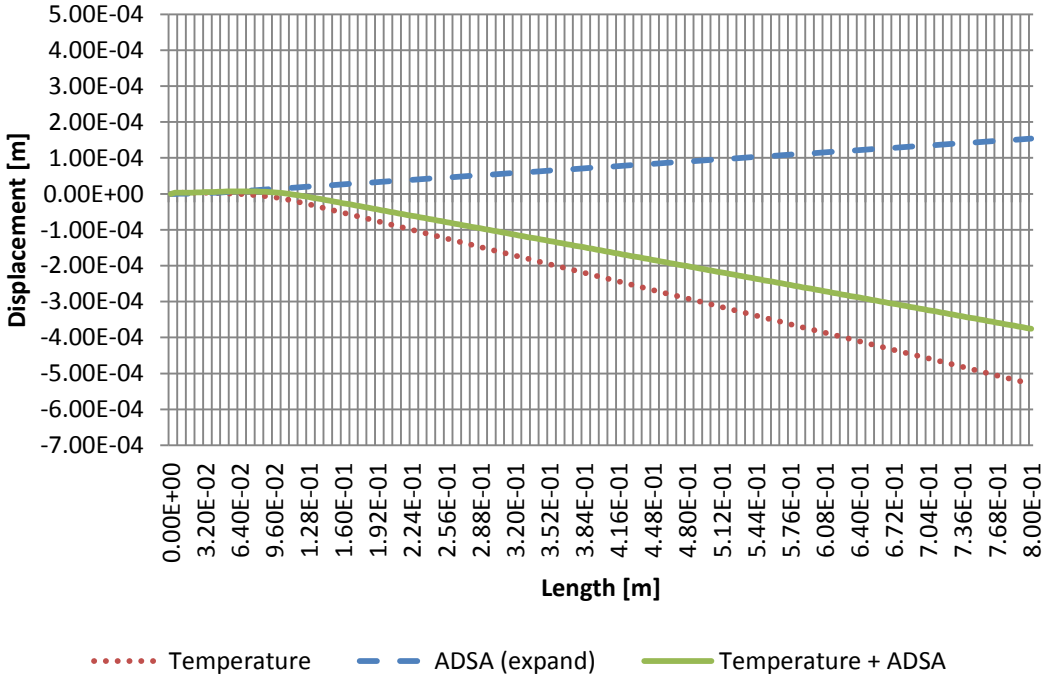

Figure 4.27 X-component of displacement exhibited by the ADSA structure for the solution Phases 4, 5 and 6, described in Table 4.18

Structure demonstrates upward deformation caused by thermal loading		
Thermal displacement [m]	Compensated displacement [m]	Compensation percentage
$351E^{-6}$	$-78.2E^{-6}$	122.26%

(a)

Structure demonstrates downward deformation caused by thermal loading		
Thermal displacement [m]	Compensated displacement [m]	Compensation percentage
$-529E^{-6}$	$-376E^{-6}$	28.99%

(b)

Table 4.20 (a) Compensation results of the ADSA where the structure deflects upward [m]; (b) Compensation results of the ADSA where the structure deflects downward [m]

Table 4.20 demonstrates that the ADSA shape compensation capacity is a dramatic improvement compared to the capability offered by the piezoelectric patches, described in Table 4.16. The table also demonstrates that the upward and downward displacements, generated by the thermal loading, vary significantly. The reason for the difference in thermal displacements is that the structure is not symmetrical, i.e. there is an actuator mounted only to the bottom side of the structure, which also explains why the compensation values differ from each other. However, this might not be the only reason. Comparing the displacement values only generated by the ADSA, which are $-429E^{-6}$ m and $153E^{-6}$ m, also demonstrate a significant difference. The displacement values obtained from the simulation are acquired by taking the difference between the original shape profile and the deformed shape profile of the beam structure, where the beam structure is in its original shape when there are no loads applied to the model. However, previous analyses of the standalone ADSA demonstrated that, when an equal pulling and pushing actuation is required, the actuator must operate around a DC-bias. This bias is not applied to the analyses conducted in this section, since it generates an undesired displacement of the beam structure, which is illustrated by Figure 4.28. The dotted blue line in the graph represents the displacement profile of the beam structure when the ADSA actuator expands. The maximum displacement value is identical to the displacement generated by solution Phase 5 and has a value of $153E^{-6}$ m.

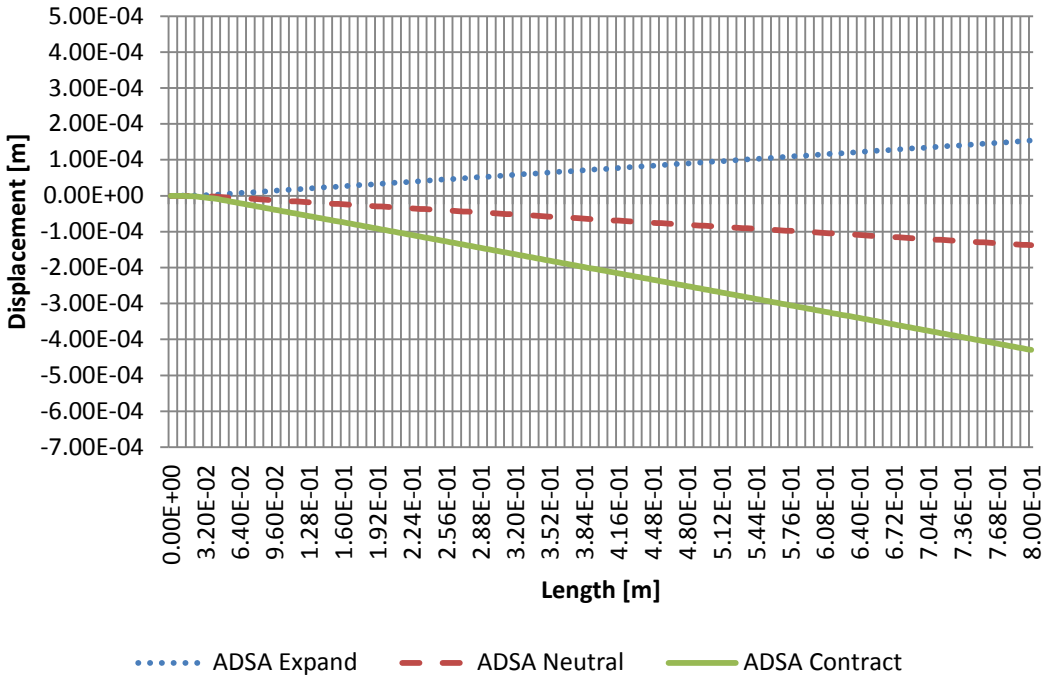

Figure 4.28 X-component of displacement exhibited by the beam structure subjected to ADSA actuation

The solid green line in Figure 4.28 represents the displacement profile of the structure when the ADSA contracts, where the structure exhibits a maximum displacement value of $-429E^{-6}$ m, which is equal to the displacement generated by solution Phase 2. The dashed red line represents the displacement profile of the beam structure when the actuator remains in its neutral position. In the neutral position, the ADSA generates an unwanted displacement of the beam structure, which has a maximum value of $-138E^{-6}$ m. The displacement is unwanted since the ADSA excites the beam structure, when it is not subjected to any thermal loads and, therefore, no displacement or compensation is required.

4.7 Chapter Summary

In this chapter, a finite element model is proposed of the dual-stack actuator developed by Heverly *et al.* [41] to study the behaviour and to identify the free displacements and blocked forces generated by the actuator. Before simulating the

dual-stack actuator, one of the piezoelectric stacks employed in the dual-stack actuator is validated theoretically, using the constitutive equations covered in Chapter 2. These values are then compared to the solution information acquired from the finite element analysis and the manufacturers' specifications of the piezoelectric stack. The free displacement values turn out to be identical, whereas the blocked force values demonstrate a difference between the manufacturers' specifications and the theoretically calculated and simulated values. This difference may be caused by the tolerance that manufacturer use in the datasheets. In addition, the piezoelectric data provided by the manufacturer is measured at small signal values, i.e. $E \ll 100$ V/mm, whereas, in practice, the piezoelectric materials operate under large field excitation values, where $E > 1$ kV/mm [18].

The finite element model is then expanded to simulate the dual-stack actuator, where the free displacements and blocked forces are identified. The total free displacement is acquired by adding the displacement of the pulling direction to the displacement of the pushing direction and is almost identical to the displacement generated by a single piezoelectric stack. However, the dual-stack actuator does exhibit a displacement in its neutral position, which is necessary to generate an identical pulling and pushing displacements. The simulated blocked force did not agree with the theoretical equation derived in the study by Heverly *et al.* [41] , since the method of measuring the blocked force in their study differs to the conventional definition. The conventional definition defines the blocked force as the force generated by the piezoelectric stack when the displacement is constrained to be zero. However, instead of constraining the displacement to zero, Heverly *et al.* [41] compressed the piezoelectric stack, that is generating all the force, beyond its neutral point into compression.

Since the displacements generated by the dual-stack actuator are limited, it is integrated into a diamond-shaped amplifying compliant structure, which amplifies the bidirectional displacements generated by the actuator. Before the finite element model of the dual-stack actuator is expanded, the compliant structure is theoretically analysed to identify and estimate the amplification ratio and resulting displacement. The compliant structure is then incorporated into the finite element model of the dual-stack actuator to create the Amplified Dual-Stack Actuator (ADSA), and solved

for the displacements and blocked forces. The solution information demonstrated that the bidirectional displacements are amplified by approximately two times. However, the compliant structure caused the overall actuator stiffness to decrease, which results in a lower blocked force.

To identify the compensation performance of the ADSA, a finite element benchmark model is built. The finite element model contains a beam structure that is subjected to thermal loading, which employs two piezoelectric patches, one on each surface of the structure, to create a bidirectional displacement of the beam structure. The thermal loading is induced by two film heaters, one on each surface of the beam structure. The thermal deformation, piezoelectric actuation and compensated displacement are identified for the beam structure, which exhibits either an upward or downward deformation caused by the thermal loading. The piezoelectric patches are then replaced by the ADSA, which is mounted to the bottom surface of the beam structure, with identical thermal and electrical loads, to make an accurate comparison between the actuation principles.

The results demonstrate that the ADSA is able to generate significantly better compensation displacements compared to the benchmark model. However, the results also revealed that the DC-bias, applied to the actuator to generate equal pulling and pushing displacements, is a great limitation when the actuator is used for shape compensation, since it creates an undesired distortion to the beam structure.

In addition, to retain the ADSA in the neutral position, an electrical field of 50 V is required at all times. Heverly *et al.* [41], who designed the dual-stack actuator that is employed in the ADSA, stated that the electrical field is necessary in order to make the actuator "self-preloading" to eliminate the requirement of a preload spring. However, preloading of a piezoelectric stack only requires a low static force level [18]. Therefore, the use of an electrical field of 50 V causes unnecessary power consumption.

The finite element analyses in this chapter provide a clear understanding of the behaviour and actuation performance of the dual-stack actuator, designed by Heverly *et al.* [41] and the ADSA. However, due to the limitation of these actuators, which cannot perform an equal bidirectional actuation without the application of a DC-bias, they are not ideal for shape control of structures. While it is still possible to

use the ADSA for shape compensation, one should note that, as a result of the DC-bias voltage, the bidirectional compensation performance is not identical. Therefore, a novel bidirectional actuator and amplified bidirectional actuator are proposed in the next chapter that eliminates the requirement of a DC-bias voltage to generate an identical pulling and pushing actuation.

Chapter 5

Design and FEM Analysis of the ABA

In this chapter, the novel bidirectional actuator and Amplified Bidirectional Actuator (ABA) are proposed, as improvements of the dual-stack actuator and the Amplified Dual-Stack Actuator (ADSA), respectively, discussed in Chapter 4. The analyses conducted in the previous chapter demonstrated an undesirable displacement effect, when the ADSA is used in an application for shape control of a structure, due to the use of a DC-bias voltage needed to preload the piezoelectric stacks, while in the neutral position.

A novel bidirectional actuator is proposed that does not need a DC-bias voltage to create identical pulling and pushing displacements. A finite element model of the bidirectional actuator is built and the free displacements and blocked force values are identified and compared to the values of the dual-stack actuator, discussed in Chapter 4. The bidirectional actuator is then incorporated in a diamond-shaped compliant amplifying structure, with the purpose of amplifying the generated bidirectional displacements. The finite element model of ABA is built, and the free displacement and blocked force values are identified. The values are then compared to the values of the ADSA. To study and identify the actuation and compensation performance of the ABA, the actuator is mounted on an identical beam structure as used for the benchmark model and the ADSA. The results are then compared against the results from the benchmark model and the ADSA and thoroughly discussed.

5.1 Construction and Operation of the Bidirectional Actuator

In Section 4.3.3, of the previous chapter, the displacement values of the dual-stack actuator developed by Heverly *et al.* [41] are identified by conducting a FEM analysis. The results, obtained in the post-processing phase, demonstrate that the extended displacement, generated by the actuator, is larger than the contracted displacement. The variation in displacement is caused by the difference in the distance along the piston from Stack 1 to the tip of the actuator, which is longer than the distance along the piston from Stack 2 to the tip of the actuator, illustrated by Figure 4.1. The compliance of the piston is proportional to its length. Therefore, Stack 1 experiences a larger compliance than Stack 2, which results in a variation in displacement generated by the actuator.

A schematic diagram of the new configuration of the piezoelectric stack is illustrated by Figure 5.1. This figure illustrates that the piezoelectric stacks are modelled in terms of generated force F_{ind1}, F_{ind2}, and short-circuit stiffness $K_{a(1)}$, $K_{a(2)}$, for Stack 1, and Stack 2, respectively. Both piezoelectric stacks are separated by a moving piston, which transfers the generated displacement x and force F_{ext}, to an external load. Therefore, the distance between Stack 1 and the piston, is identical to the distance between Stack 2 and the piston, which results in both stacks experiencing the same compliance.

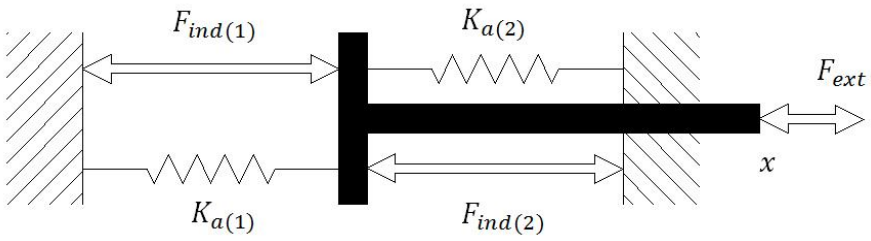

Figure 5.1 Schematic diagram of the bidirectional actuator

The far left and right sides of Stack 1 and Stack 2, respectively, must be constrained so that the displacement and force generated by the stacks are transferred to the piston.

A cross-sectional view of the geometry of the bidirectional actuator is illustrated by Figure 5.2. The two piezoelectric stacks are constrained by a rectangular-shaped housing. The piston is placed in between the two piezoelectric stacks and is the only moving part of the actuator. The piezoelectric stacks, used in the actuator, are ring stacks and are identical to the stacks used in the dual-stack actuator, discussed in Chapter 4. However, the construction of the bidirectional actuator, illustrated by Figure 5.2, allows the utilisation of solid square or cylindrical stack actuators to increase the blocked force, if required. In order to make a fair comparison between the bidirectional actuator and the dual-stack actuator, identical piezoelectric stack actuators are utilised.

The next section of this chapter continues to build a finite element model of the bidirectional actuator to identify the free displacement and blocked force values.

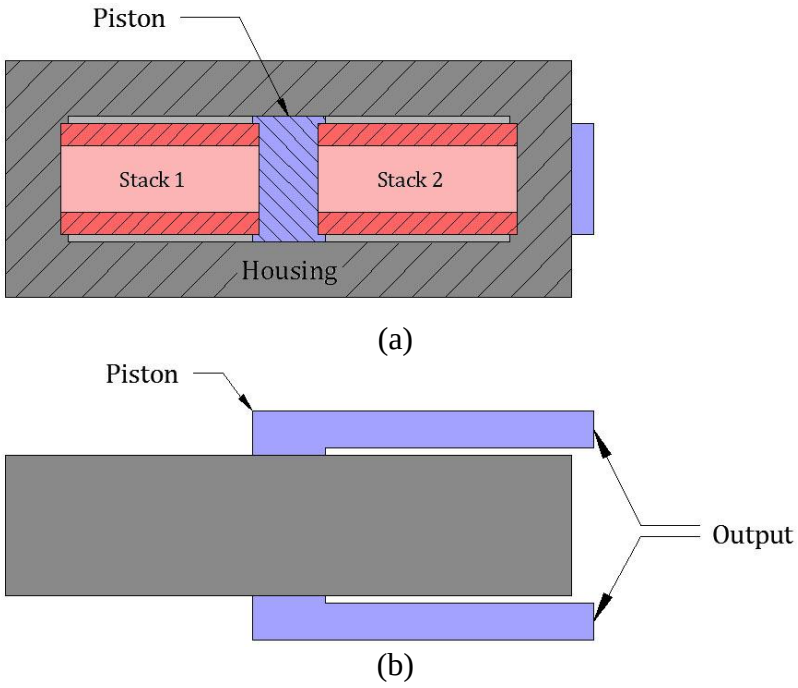

Figure 5.2 (a) Cross-sectional view of the bidirectional actuator; (b) Top view of the bidirectional actuator

5.2 FEM Analysis of the Bidirectional Actuator

In this section, a finite element model of the bidirectional actuator is built and the actuation performance is identified by simulating the free displacement and blocked force values of the actuator. Comparisons between the free displacement and blocked force values of the dual-stack actuator and the bidirectional actuator are then made, followed by a discussion of the results.

5.2.1 Finite Element Model of the Bidirectional Actuator

The configuration and parameters of the bidirectional actuator are illustrated by Figure 5.3, where the dimensions belonging to the parameters are described in Table 5.1. The u-shaped piston is mounted in between the two piezoelectric stacks and both arms of the piston exit both sides of the actuator's housing. The housing walls, denoted by l_ht1 and h_ht1, of the bidirectional actuator are relatively thick with a dimension of $7.5E^{-3}$ m, which is necessary since the housing must constrain the piezoelectric stack. The sides of the housing denoted by h_w1 are relatively thin and have a dimension of $1E^{-3}$ m. Their purpose is to protect the piezoelectric stack against environmental influences rather than to provide additional stiffness of the housing. The dimensions of the bidirectional actuator have increased by $1E^{-3}$ m, $6E^{-3}$ m and $7E^{-3}$ m for the length, width and height, respectively, compared to the dimensions of the dual-stack actuator. However, the dimensions of the bidirectional actuator are initial dimensions, and once the performance of the actuator is identified, it is possible to execute a design optimisation procedure to minimise the dimensions.

The finite element model is built using 3-dimensional SOLID226 elements, with KEYOPT(1) set to 1001, to perform a piezoelectric analysis. The housing and piston are modelled out of stainless steel 304, which is the same material used for the dual-stack actuator. The piezoelectric stacks utilised in the bidirectional actuator are identical to the stacks of the dual-stack actuator. All material properties defined in the analysis can be found in Appendix A.

First, one-half of the geometry is built, as illustrated by Figure 5.2, and the piezoelectric stacks are glued together by executing the VLGUE command.

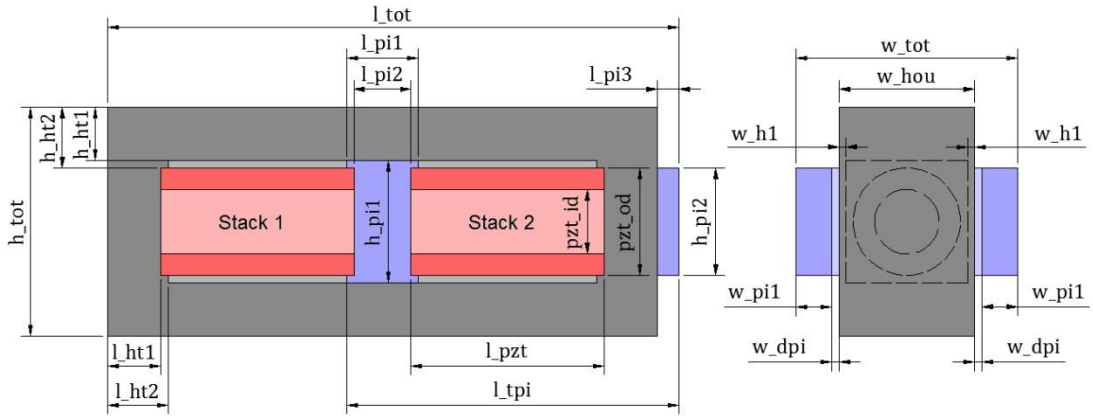

Figure 5.3 Geometry and parameters of the bidirectional actuator

Parameter	Description	Value [m]
l_tot	Total length of the actuator	$80.0E^{-3}$
h_tot	Total height of the actuator	$32.0E^{-3}$
w_tot	Total width of the actuator	$31.0E^{-3}$
l_ht1	Thickness of the left and right housing wall	$7.5E^{-3}$
l_ht2	Thickness of the left and right stack holder	$8.5E^{-3}$
h_ht1	Thickness of the top and bottom housing wall	$7.5E^{-3}$
h_ht2	Thickness of the top and bottom stack holder	$8.5E^{-3}$
w_hou	Width of the housing	$19.0E^{-3}$
w_h1	Thickness of the side walls	$1.0E^{-3}$
l_tpi	Total length of the piston	$46.5E^{-3}$
l_pi1	Length of the piston part with stack holder	$10.0E^{-3}$
l_pi2	Length of the piston part	$8.0E^{-3}$
l_pi3	Extension of the piston	$3.0E^{-3}$
h_pi1	Height of the piston part with stack holder	$17.0E^{-3}$
h_pi2	Height of the piston	$15.0E^{-3}$
w_pi1	Width of the piston that connects to external load	$5.0E^{-3}$
w_dpi	Distance between the piston arms and housing	$1.0E^{-3}$
l_pzt	Length of the piezoelectric stacks	$27.0E^{-3}$
pzt_od	Outer diameter of the piezoelectric stacks	$15.0E^{-3}$
pzt_id	Inner diameter of the piezoelectric stacks	$9.0E^{-3}$

Table 5.1 Parameters and dimensions of the bidirectional actuator

The mesh sizes are then manually set for the piezoelectric stacks, in order to control the amount of nodes and elements generated in the finite element model. The elements, used to mesh the housing and piston, are tetrahedral-shaped elements with a size of $2E^{-3}$ m. To generate a full finite element model of the actuator, the command VSYMM is executed, which reflects the model on the XY-plane. The nodes are then merged using the NUMMRG command. This is a crucial step, since the nodes on the symmetry plane are doubled. Therefore, if the nodes are not merged, ANSYS treats the model as two separate geometries that are not connected to each other. The generated finite element model is illustrated by Figure 5.4.

The bottom surface of the actuator, at location Y = 0, is constrained in all directions. In order to identify the free displacements of the bidirectional actuator, the model is solved in three phases, which simulate the generated displacements in the contracted, neutral and extended positions of the actuator. The electrical fields applied to the piezoelectric stacks are identical in strength to those of the dual-stack actuator for the contracted and extended positions. Note that since the configuration of the piston is modified, the orientation of the applied electrical fields is changed. To perform a contracting actuation, an electrical field of $V_{Stack1} = 0$ V, $V_{Stack2} = 100$ V is applied to the bidirectional actuator. In order to perform an extending actuation, an electrical field of $V_{Stack1} = 100$ V, $V_{Stack2} = 0$ V is applied.

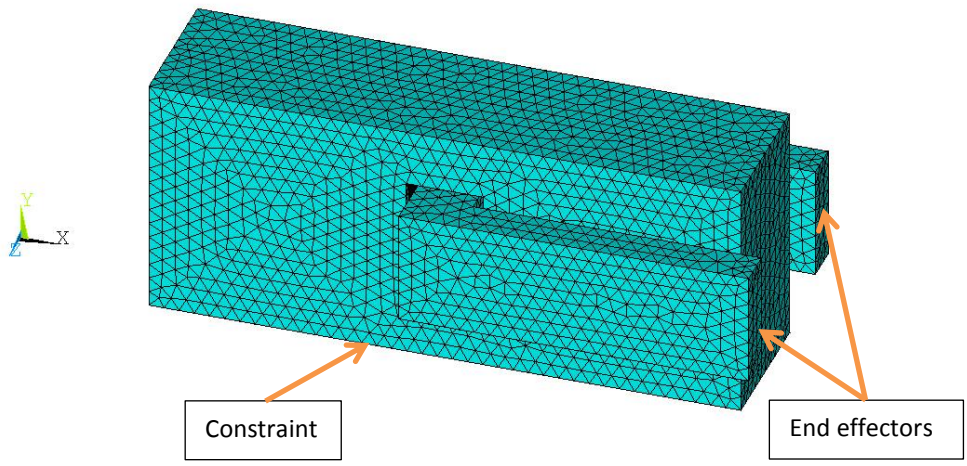

Figure 5.4 Generated finite element model of the bidirectional actuator

The neutral phase is simulated by applying an electrical field of 10 V to both piezoelectric stacks. The electrical field strength is greatly reduced, since it is not necessary to create any offset in displacement. The purpose of applying the electrical field, in the neutral phase, is solely to eliminate the need of a preload spring, which is used to retain the piezoelectric stacks under a constant force to protect the stacks against tensile loads. However, when an electrical field of 10 V is applied, both stacks expand and, therefore, keep each other under a constant load, which is called *active preloading* [18]. An overview of the applied electrical fields to the bidirectional actuator is given in Table 5.2.

Relevant information about the finite element model is described in Table 5.3. The mass is increased by approximately 150 g in comparison to that of the dual-stack actuator. The finite element model is solved for the X-component of displacement in three phases under different electrical fields, as described in Table 5.2.

Phase	V_{Stack1} **[V]**	V_{Stack2} **[V]**	**Position**
1	0	100	Contracted
2	10	10	Neutral
3	100	0	Extended

Table 5.2 Applied electrical loads [V] to the bidirectional actuator

Number of elements	92,724
Number of nodes	318,061
Analysis type	Small Displacement Static
Mass	342.6 g

Table 5.3 Finite element model information of the bidirectional actuator

5.2.2 Free Displacement Results of the Bidirectional Actuator

Figure 5.5, Figure 5.6 and Figure 5.7 illustrate the solution results of the X-component of displacement for the contracted, neutral and extended positions, respectively. The displacement values are obtained using the method described in Section 2.2.4. The X-component of displacement is mapped onto the nodes of the two end effectors of the piston that can be connected to an external load, illustrated by Figure 5.2. The average displacement value is then calculated.

The bidirectional actuator generates a contraction displacement of $-7.66E^{-6}$ m and an extension displacement of $7.46E^{-6}$ m. The neutral displacement has a value of $-0.02E^{-6}$ m.

A comparison between the generated free displacement values of the dual-stack actuator and the bidirectional actuator is given by Table 5.4. This table demonstrates that the undesired displacement produced by the bidirectional actuator, in the neutral position, is reduced by 99.5%. The displacement values of the bidirectional actuator, in the contracted and extended positions, are slightly reduced by approximately $0.5E^{-6}$ m, compared to the dual-stack actuator. This reduction is caused by the deformation of the actuator's housing wall, generated by the force of the piezoelectric stacks and can be reduced by increasing the thickness of the housing wall. However, since the reduction is only 6%, in this thesis, no further alterations are made to the bidirectional actuator.

Contracted position [m]	**Neutral position [m]**	**Extended position [m]**
$-4.32E^{-6}$	$3.73E^{-6}$	$11.78E^{-6}$
Δ displacement		Δ displacement
$8.05E^{-6}$		$8.05E^{-6}$

(a)

Contracted position [m]	**Neutral position [m]**	**Extended position [m]**
$-7.66E^{-6}$	$-0.0197E^{-6}$	$7.46E^{-6}$

(b)

Table 5.4 (a) free displacement values [m] generated by the dual-stack actuator; (b) free displacement results [m] generated by the bidirectional actuator

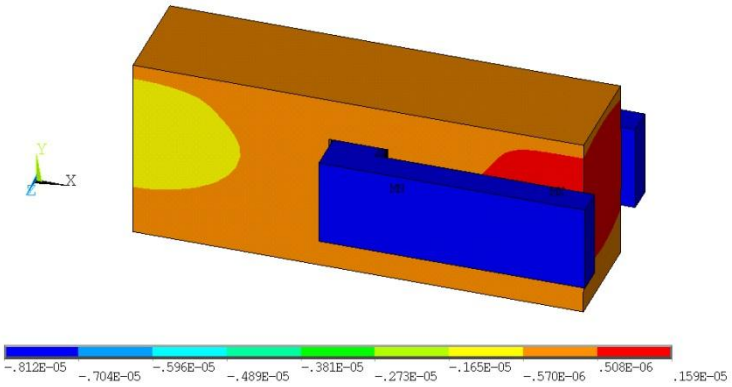

Figure 5.5 X-component of displacement [m] generated by the bidirectional actuator in the contracted position

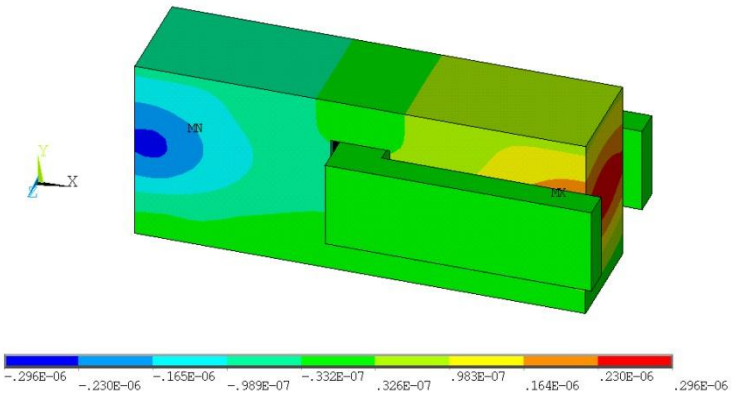

Figure 5.6 X-component of displacement [m] generated by the bidirectional actuator in the neutral position

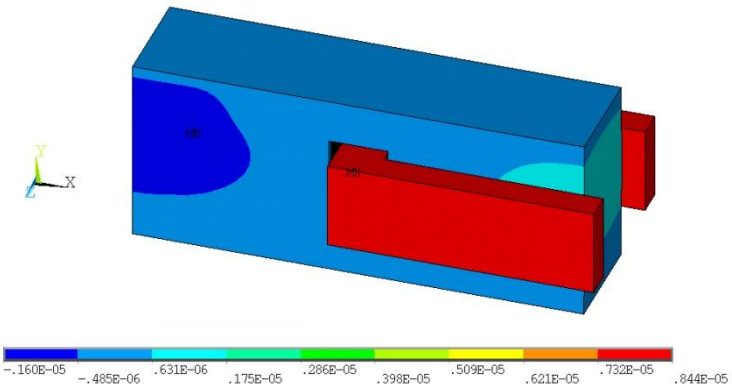

Figure 5.7 X-component of displacement [m] generated by the bidirectional actuator in the extended position

5.2.3 Blocked Force Results of the Bidirectional Actuator

The blocked force values of the bidirectional actuator are identified according to the method described in Section 2.2.5. To reiterate, the bottom side of the actuator is constrained in all directions and an electrical field of $V_{Stack1} = 0$ V, $V_{Stack2} = 100$ V is applied, causing the bidirectional actuator to contract. An extension force of increasing magnitude is then applied to the end effectors, illustrated in Figure 5.4, until the actuator reaches its neutral position at which point the pulling force is equivalent to the blocked contracting force. The reverse procedure is performed to identify the blocked extending force, where an electrical field of $V_{Stack1} = 100$ V, $V_{Stack2} = 0$ V is applied. An increasing compression force is then applied to the end effectors until it reaches the neutral position, at which point the compression force is equal to the blocked expansion force.

The relationship between the force and displacement generated by the bidirectional actuator is illustrated by Figure 5.8. The points, where the contracting and extending data lines intercept with the Y-axis, represent the blocked force.

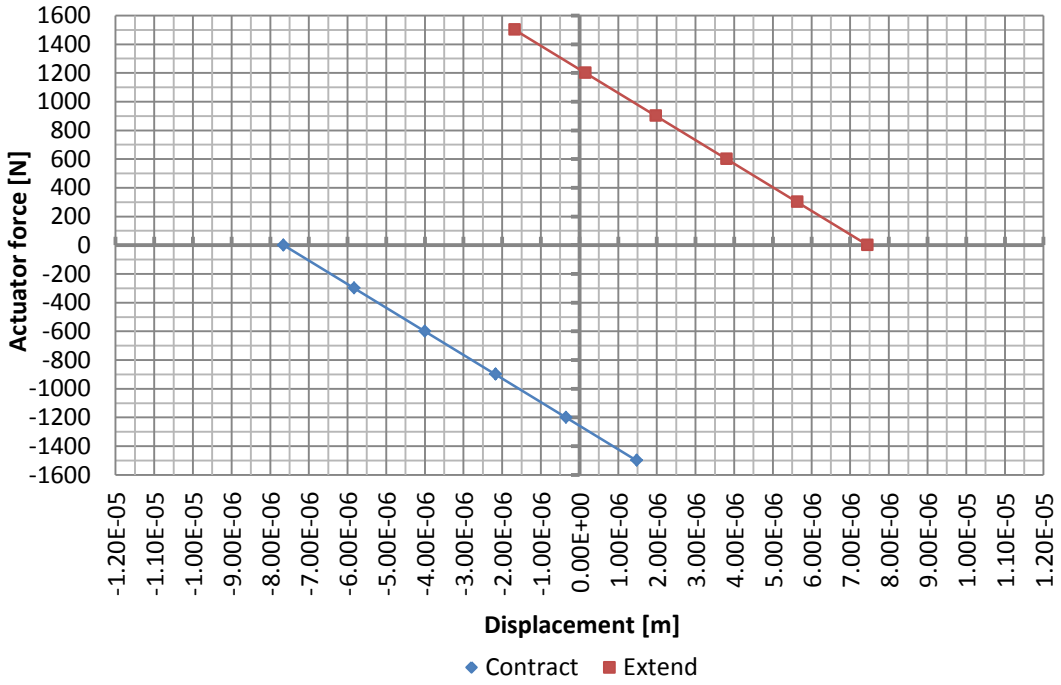

Figure 5.8 Force vs. displacement graph of the bidirectional actuator

The points, where both data lines intercept the X-axis, represent the free displacement values, which are identical to the values described in Table 5.4(b). To calculate the relationship between the free displacement and blocked force values of the bidirectional actuator, a linear regression fit is performed, which results in the following regression equations:

$$y_{con} = -1.64\mathrm{E}^{8}x - 1257, \tag{5.1}$$

and

$$y_{ext} = -1.64\mathrm{E}^{8}x + 1225. \tag{5.2}$$

The blocked force values generated by the bidirectional actuator are summarised and compared against the blocked force values of the dual-stack actuator by Table 5.5. The generated blocked force values of the bidirectional actuator are reduced by approximately 8.5% compared to the dual-stack actuator, which might be caused by the deformation of the u-shaped piston and the housing.

A plot of the distribution of the X-component of stress in the piston is illustrated by Figure 5.9 and demonstrates that the piston still deforms when a large force is generated. The piezoelectric stack that is generating the force, in Figure 5.9, is mounted in between the effectors of the piston. When the stack expands, it generates a force, which is transferred from the stack to the piston at the contact point. This force causes the effectors of the piston to deform, which explains why the stress on the inside of the end effectors, in Figure 5.9, is higher than the stress on the outside of the end effectors. However, a significant improvement of the bidirectional actuator is the elimination of the DC-bias voltage, which is illustrated by Figure 5.8, since the actuator does not generate a displacement in the neutral position.

	Pulling force [N]	**Pushing force [N]**
Dual-stack actuator	-1353	1365
Bidirectional actuator	-1257	1225

Table 5.5 Comparison of the blocked force values [N] generated by the dual-stack actuator and the bidirectional actuator

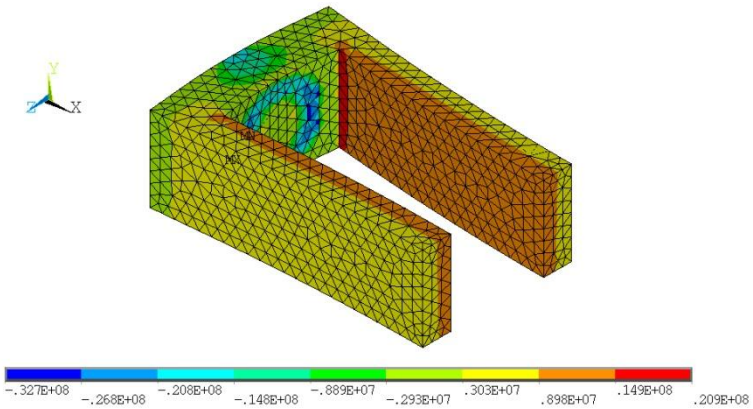

Figure 5.9 X-component of stress [Pa] of the piston when the bidirectional actuator contracts

5.3 Analysis of the Amplified Bidirectional Actuator

In the previous section, the free displacement and blocked force values of the bidirectional actuator are identified and compared against the values of the dual-stack actuator. In this section, the Amplified Bidirectional Actuator (ABA) is proposed. The finite element model of the ABA is built by incorporating an amplifying compliant structure to the finite element model of the bidirectional actuator. The free displacement and blocked force values of the ABA are then identified and compared against the values of the ADSA, as discussed in Section 4.4.

5.3.1 Geometry and Finite Element Model of the ABA

A new compliant structure is developed according to the dimensions of the bidirectional actuator. The geometry of the compliant structure and the bidirectional actuator is illustrated by Figure 5.10. When the bidirectional actuator is mounted directly into the compliant structure, a problem occurs regarding the wall-thickness of the bidirectional actuator's housing. The simulations conducted in Section 5.2.2, which identified the free displacements of the bidirectional actuator, demonstrate that the housing walls of the actuator exhibit a deformation when the actuator is performing a pulling or pushing actuation.

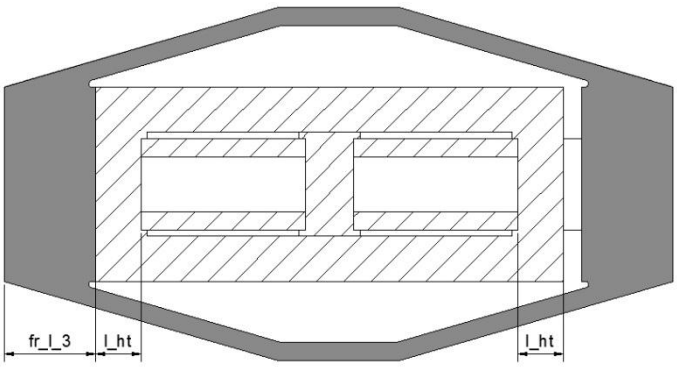

Figure 5.10 Geometry of the compliant structure and the unaltered bidirectional actuator

However, this deformation is almost identical for the pulling and pushing actuation, since the wall thickness on the left side of the actuator is identical to the wall thickness on the right side of the actuator, denoted by l_ht in Figure 5.10. Therefore, in order to achieve an identical pulling and pushing actuation, the wall thickness on the left and right sides of the actuator must be identical. When the bidirectional actuator is mounted into the compliant structure, as illustrated by Figure 5.10, the new wall-thickness on the left side of the bidirectional actuator equals $fr\_l\_3 + l\_ht$. The wall-thickness on the right side of the actuator remains equal to l_ht, which will increase the difference between the pulling and pushing displacements. Therefore, the wall thickness of the bidirectional actuator is modified to have identical values, when mounted onto the compliant structure.

The geometry of the modified bidirectional actuator and the compliant structure is illustrated by Figure 5.11, whereas the parameters and dimensions are described in Table 5.6. The piezoelectric elements are now constrained by the left wall of the compliant structure, denoted by fr_l_3, and the right wall of the bidirectional actuator, denoted by l_ht1, which have identical sizes. Calculating the amplification displacement of the compliant structure using (3.3) gives:

$$\delta = 14\mathrm{E}^{-3} - \sqrt{(14\mathrm{E}^{-3})^2 - 2 * 3.78\mathrm{E}^{-6} * 30.8\mathrm{E}^{-3} - (3.78\mathrm{E}^{-6})^2} = 8.54\mathrm{E}^{-6}\ \mathrm{m}. \tag{5.3}$$

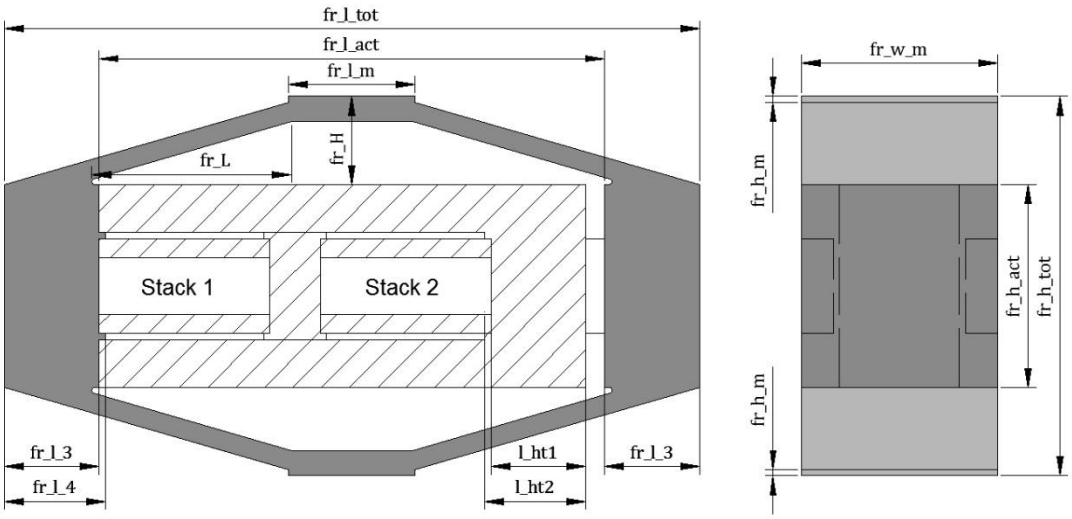

Figure 5.11 Geometry of the ABA

Parameter	Description	Value [m]
fr_l_tot	Total length of the compliant structure	$110.0E^{-3}$
fr_h_tot	Total height of the compliant structure	$60.0E^{-3}$
fr_w_m	Total width of the compliant structure and mounting area	$31.0E^{-3}$
fr_l_m	Length of the mounting area	$20.0E^{-3}$
fr_h_m	Height of the mounting area	$1.0E^{-3}$
fr_l_act	Free length to mount the bidirectional actuator	$80.0E^{-3}$
fr_h_act	Free height to mount the bidirectional actuator	$32.0E^{-3}$
fr_l_3	Wall thickness of the compliant structure	$15.0E^{-3}$
fr_l_4	Wall thickness of the stack holder of the structure	$16.0E^{-3}$
l_ht1	Wall thickness of the bidirectional actuator	$15.0E^{-3}$
l_ht2	Wall thickness of the stack holder of the actuator	$16.0E^{-3}$
fr_L	Length to theoretically verify the amplification factor	$31.6E^{-3}$
fr_H	Height to theoretically verify the amplification factor	$14.0E^{-3}$

Table 5.6 Parameters and dimensions of the ABA

The amplification factor of the compliant structure is calculated using (3.4), and equals:

$$r = \frac{8.54\text{E}^{-6}}{3.78\text{E}^{-6}} = 2.26. \tag{5.4}$$

Note that the displacement in (5.3) is calculated for the top part of the compliant structure. Therefore, the total estimated displacement of the compliant structure is estimated to be 17.1E^{-6} m. The total size of the ABA is larger in comparison to the ADSA, where the total length, width and height of the ABA is increased by, 4E^{-3} m, 6E^{-3} m and 9E^{-3} m, respectively. Hence, the mass of the ABA is 270 g more than the ADSA, since both bidirectional actuator and compliant structure are increased in size.

A new finite element model is built, utilising 3-dimensional SOLID226 elements, with KEYOPT(1) set to 1001, in order to perform a piezoelectric analysis. First one half of the geometry is built, and the piezoelectric stacks are glued and meshed. The global element size of the compliant structure and the housing of the bidirectional actuator are manually set to 4E^{-3} m. The mesh size at the contact areas, where the piezoelectric stack elements are in contact with the compliant structure and the housing, is set to 2E^{-3} m. The compliant structure and actuator's housing are then meshed with tetrahedral elements using the material stainless steel 304. All material properties, utilised in the model, are described in Appendix A. The generated finite element model of the ABA is illustrated by Figure 5.12.

In order to identify the free displacements, one output of the compliant structure is constrained in all directions. Therefore, the displacement of interest, i.e. the Y-component of displacement, only occurs at the unconstrained output of the compliant structure, illustrated in Figure 5.12. The model is solved for the free displacement and the blocked force. The electrical fields applied to the ABA, to identify the free displacements, are described in Table 5.2. Relevant information about the finite element model is described in Table 5.7.

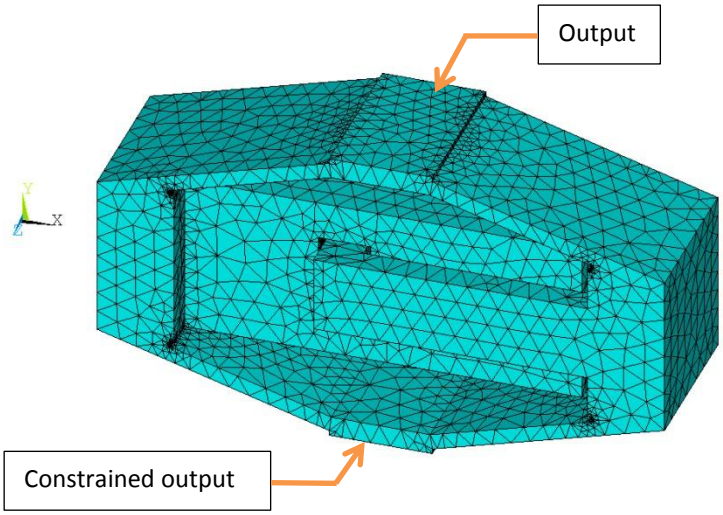

Figure 5.12 Generated finite element model of the ABA

Number of elements	126,982
Number of nodes	382,395
Analyses type	Small Displacement Static
Mass	740.59 g

Table 5.7 Finite element model information of the ABA

5.3.2 Free Displacement Results of the ABA

The Y-component of displacement values are acquired according to the method described in Section 2.2.4. The displacement results are mapped onto the nodes of the unconstrained output of the ABA. The average Y-component of displacement is then calculated. Figure 5.13, Figure 5.14 and Figure 5.15 illustrate the displacement in the Y-direction, generated by the ABA, in the contracted, neutral and expanded positions, respectively.

The displacement value generated by the ABA, in the contracted position, is simulated to be $-21.16E^{-6}$ m, whereas, the displacement in the expanded position, has a value of $17.14E^{-6}$ m. These values are presented in Table 5.8.

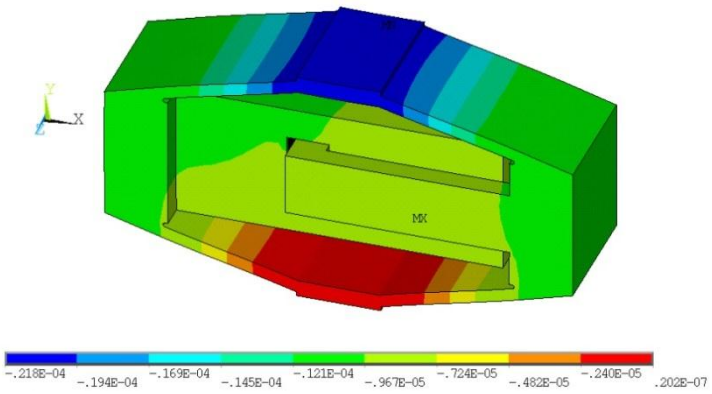

Figure 5.13 Y-component of displacement [m] generated by the ABA in the contracted position

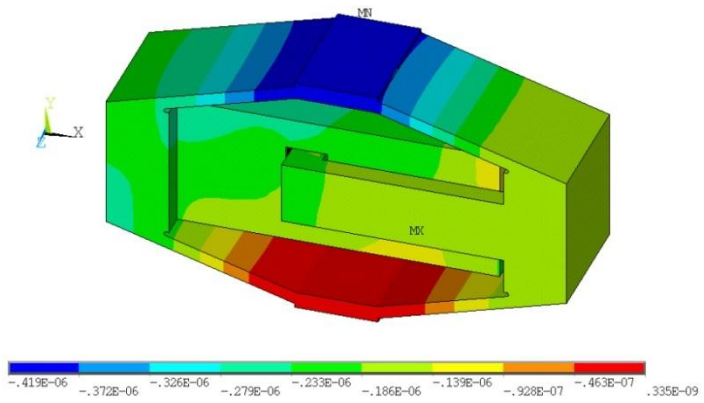

Figure 5.14 Y-component of displacement [m] generated by the ABA in the neutral position

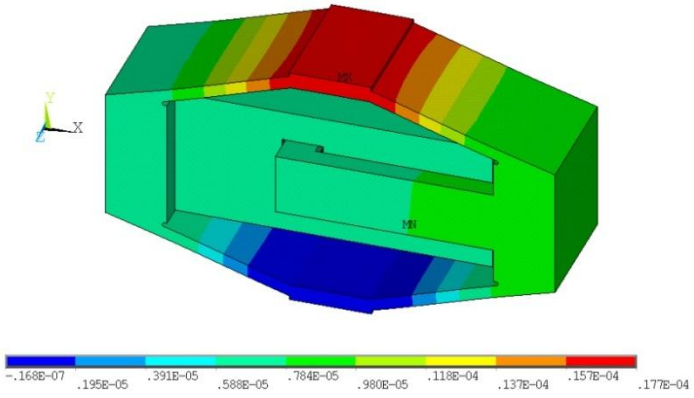

Figure 5.15 Y-component of displacement [m] generated by the ABA in the expanded position

Contracted position [m]	Neutral position [m]	Expanded position [m]
$-28.29E^{-6}$	$-9.09E^{-6}$	$10.11E^{-6}$
Δ displacement		Δ displacement
$19.20E^{-6}$		$19.20E^{-6}$

(a)

Contracted position [m]	Neutral position [m]	Expanded position [m]
$-21.16E^{-6}$	$-0.40E^{-6}$	$17.14E^{-6}$

(b)

Table 5.8 (a) Free displacement values [m] generated by the ADSA; (b) Free displacement values [m] generated by the ABA

The generated displacement by the ABA, in the neutral position, is reduced by 96% compared to the displacement value of the ADSA and has a value of $-0.40E^{-6}$ m.

The contracting displacement generated by the ABA is larger than the expanded displacement, which may be caused by the way the bidirectional actuator is mounted to the compliant structure. Piezoelectric Stack 1 is directly in contact with the compliant structure, whereas Stack 2 is in contact with the housing, as illustrated by Figure 5.11. The percentage difference is calculated to be:

$$\Delta_{ABA} = \left| \frac{21.16E^{-6} - 17.14E^{-6}}{(21.16E^{-6} + 17.14E^{-6})/2} \right| * 100\% = 21\% , \tag{5.5}$$

and

$$\Delta_{ADSA} = \left| \frac{28.29E^{-6} - 10.11E^{-6}}{(28.29E^{-6} + 10.11E^{-6})/2} \right| * 100\% = 95\% . \tag{5.6}$$

It is clear that the displacement values in the contracted and expanded positions of the ABA, which differ by 21%, are considerably closer together compared to the values of the ADSA, which differ by 95% when the neutral position is not taken into account.

The reduction in free displacement values is caused by the compliant structure, which is considerably wider when compared to the compliant structure of the ADSA,

thus resulting in an increase in stiffness of the compliant structure. Therefore, the bidirectional actuator has to generate a larger force, which results in a reduction of displacement to move the compliant structure. It is always possible to change the material of the compliant structure to a more advanced composite material. However, in order to make a fair comparison between the two actuators, stainless steel 304 material is used in this study to model the compliant structure.

5.3.3 Blocked Force Results of the ABA

The blocked force of the ABA, for the expansion direction, is identified according to the procedure described in Section 2.2.5. One output is constrained in all directions, as illustrated in Figure 5.12, and an electrical field of $V_{Stack1} = 0$ V, $V_{Stack2} = 100$ V is applied, causing the ABA to expand. A compression force of increasing magnitude is then applied to the unconstrained output, illustrated in Figure 5.12, until the ABA reaches its neutral position at which point the compression force is equivalent to the blocked expansion force. The reverse procedure is performed to identify the blocked contraction force, where an electrical field of $V_{Stack1} = 100$ V, $V_{Stack2} = 0$ V is applied. An increasing expansion force is then applied to the unconstrained output until it reaches the neutral position, at which point the expansion force is equal to the blocked contraction force.

Figure 5.16 illustrates the force versus displacement graph of the ABA. The points in the graph, where the two data lines intercept the Y-axis, represent the blocked forces. The maximum force, generated by the ABA, in the pulling direction has a value of -270 N, whereas, the maximum pushing force has a value of 219 N. The points in the graph, where the two data lines intercept with the X-axis, represent the free displacement of the ABA and are identical to the values described in Table 5.8(b). The graph, represented in Figure 5.16, is particularly useful to identify the amount of displacement that the ABA is able to generate when the external load is known.

To calculate the relationship between the free displacement and blocked force values of the bidirectional actuator, a linear regression fit is performed, which results in the following regression equations:

$$y_{cont} = -1.28\text{E}^{7}x - 270.24, \tag{5.7}$$

and

$$y_{ext} = -1.28\text{E}^{7}x + 219.04. \tag{5.8}$$

The blocked force values, generated by the ADSA, are described in Table 5.9(a), where the DC-bias is either enabled or disabled.

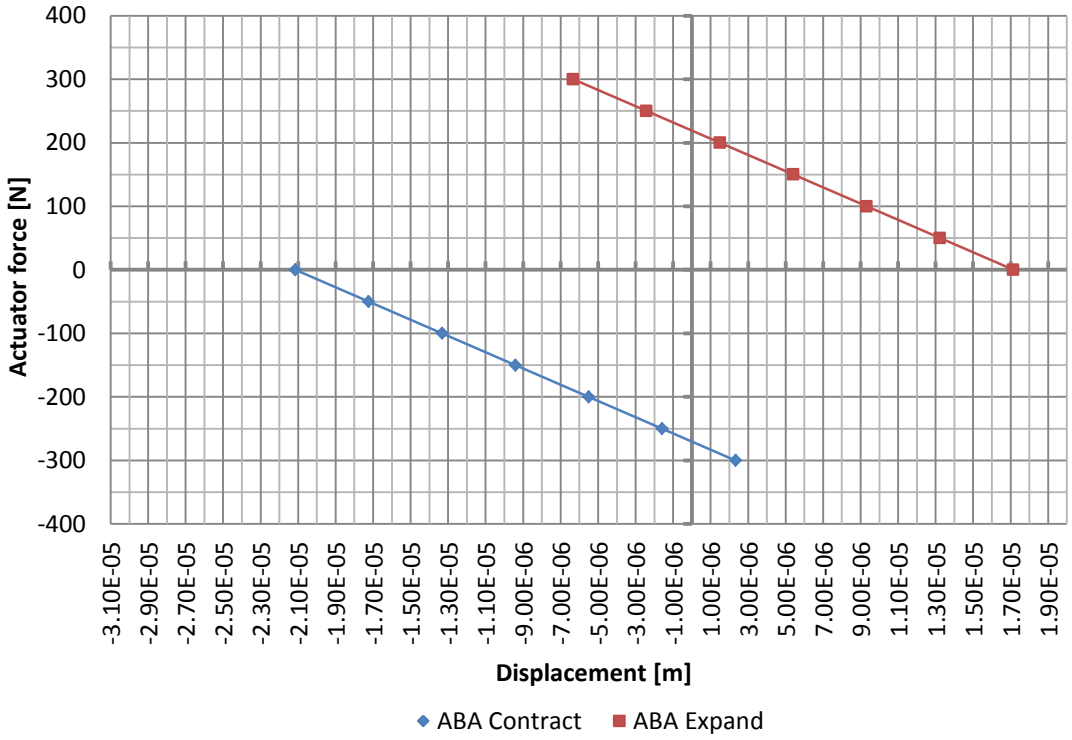

Figure 5.16 Force vs. displacement graph of the ABA

DC-Bias	ADSA pulling blocked force [N]	ADSA pushing blocked force [N]
Enabled	−236	237
Disabled	−347	125

(a)

DC-Bias	ABA pulling blocked force [N]	ABA pushing blocked force [N]
N/A	−270	219

(b)

Table 5.9 (a) Blocked force values [N] generated by the ADSA; (b) Blocked force values [N] generated by the ABA

The DC-bias is applied to the ADSA to generate equal pulling and pushing displacements and blocked forces. However, the DC-bias has some major drawbacks. As described in Section 4.6, the DC-bias also generates an undesired displacement of the structure, since the ADSA contracts when the DC-bias is applied. Therefore, the DC-bias should not be enabled when the ADSA is employed for shape control. Another drawback of the DC-bias is the unnecessary power consumption when the ADSA does not have to compensate for the shape distortions. As a result, the free displacement and blocked force values of the ADSA must also be considered when the DC-bias is disabled. Table 5.9 demonstrates that the blocked force values of the ABA differ by 21%, whereas the blocked force values of the ADSA, when the DC-bias is not taken into account, differ by 94%. The ABA, which does not need a DC-bias, demonstrates to be a significant improvement compared to the ADSA.

5.4 Thermal Deformation Compensation Performance of the ABA

A finite element model is built to identify the compensation performance of the ABA. The test structure is identical to that described in Section 4.6, apart from the substitution of the ABA actuator in place of the ADSA actuator.

The geometry and dimensions of the finite element model are illustrated and described in Figure 5.17 and Table 5.10, respectively. The beam structure and film heaters are identical in size as the structure and heaters employed in the benchmark model. However, since the dimensions of the ABA have changed, the position and height of the rib are altered in order to mount the ABA onto the beam structure. The beam structure is modelled out of aluminium alloy T6, whereas the ABA is modelled out of stainless steel 304, which properties can be found in Appendix A. The model is built using 3-dimensional SOLID226 elements, with KEYOPT(1) set to 1011, to perform a structural-thermoelectric coupled-field analysis. The finite element model of the ABA, illustrated by Figure 5.12, is expanded to incorporate the beam structure and film heaters. The beam structure is then meshed with tetrahedral-shaped elements with a size of $5E^{-3}$ m, whereas the film heaters are meshed with $2E^{-3}$ m hexahedral-shaped elements. The left most side of the model is constrained in all

directions. Both film heaters and the ABA are mounted onto the beam structure using the MPC contact algorithm.

The procedure of solving the model and applying the loads is identical to the procedure used for the benchmark model, and consists of six phases described in Table 5.11. V_{Stack1} and V_{Stack2} represent the electrical fields applied to piezoelectric Stack 1 and Stack 2, respectively. The top film heater is denoted by H_{top} and the bottom film heater by H_{bot}. The amount of electrical field and thermal loadings, applied to the finite element model, are identical to the loads of the benchmark model.

The first three phases, described in Table 5.11, simulate and identify the achieved compensation of the beam structure by the ABA, when the structure exhibits a deformation in an upward direction caused by the thermally induced loading. The last three phases identify the achieved compensation by the ABA, when the beam structure exhibits a deformation in the downward direction caused by the thermally induced loading. Phases 1 and 4 simulate the beam structure under thermal loading to identify the thermal deformation. Phases 2 and 5 then simulate the beam structure, where only the ABA is activated to identify the generated displacements by the actuator. In the final Phases, 3 and 6, the finite element model is solved for thermal and electrical loading to identify the displacements of the compensated beam structure. Therefore, both the ABA and the film heaters are activated. After solving each phase, the solution information is written to a database file for post-processing purposes.

Relevant information about the generated finite element model is described in Table 5.12. The finite element model consists of a larger number of nodes and elements compared to the finite element model of the ADSA, which is described in Section 4.6. The generated finite element model is illustrated by Figure 5.18. The figure illustrates the locations of the MPC contact points. The left end of the beam and the ABA are constrained in all directions.

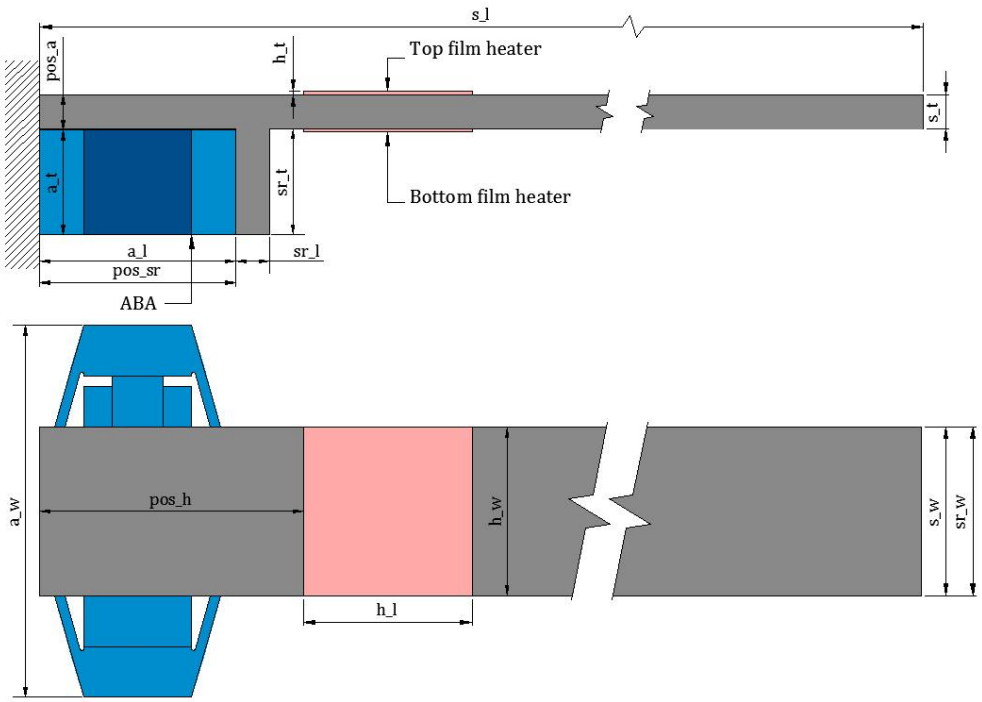

Figure 5.17 Geometry of the beam structure and the ABA

Parameter	Description	Value [m]
s_l	Length of the beam structure	$800.0E^{-3}$
s_w	Width of the beam structure	$50.0E^{-3}$
s_t	Thickness of the beam structure	$10.0E^{-3}$
h_l	Length of the film heaters	$50.0E^{-3}$
h_w	Width of the film heaters	$50.0E^{-3}$
h_t	Thickness of the film heaters	$0.\ 2E^{-3}$
a_l	Length of the ABA	$58.0E^{-3}$
a_w	Width of the ABA	$110.0E^{-3}$
a_t	Thickness of the ABA	$31.0E^{-3}$
sr_l	Length of the rib	$10.0E^{-3}$
sr_w	Width of the rib	$50.0E^{-3}$
sr_t	Thickness of the rib	$31.5E^{-3}$
pos_h	Position of the film heaters	$78.0E^{-3}$
pos_a	Position of the ABA	$10.5E^{-3}$
pos_sr	Position of the rib	$58.0E^{-3}$

Table 5.10 Parameters and dimensions of the beam structure and the ABA

Phase 1	21. Apply electrical field, $V_{Stack1} = V_{Stack\,2} = 0$ V, 22. Apply temperature, $H_{top} = 45$ °C , $H_{bot} = 50$ °C, 23. Apply a convection coefficient to air of 5 W/(m^2·°C), 24. Set reference temperature to 22 °C, 25. Solve and save solution results.
↓	
Phase 2	26. Delete temperature load at H_{top} and H_{bot}, 27. Apply electrical field, $V_{Stack1} = 100$ V, $V_{Stack2} = 0$ V, 28. Solve and save solution results.
↓	
Phase 3	29. Apply temperature, $H_{top} = 45$ °C , $H_{bot} = 50$ °C, 30. Apply electrical field, $V_{Stack1} = 100$ V, $V_{Stack2} = 0$ V, 31. Solve and save solution results.
↓	
Phase 4	32. Apply electrical field, $V_{Stack1} = V_{Stack\,2} = 0$ V, 33. Apply temperature, $H_{top} = 50$ °C , $H_{bot} = 45$ °C, 34. Solve and save solution results.
↓	
Phase 5	35. Delete temperature load at H_{top} and H_{bot}, 36. Apply electrical field, $V_{Stack1} = 0$ V, $V_{Stack2} = 100$ V, 37. Solve and save solution results.
↓	
Phase 6	38. Apply temperature, $H_{top} = 50$ °C , $H_{bot} = 45$ °C, 39. Apply electrical field, $V_{Stack1} = 0$ V, $V_{Stack2} = 100$ V, 40. Solve and save solution results.

Table 5.11 Applied loads and solution process of the beam structure and ABA

Number of elements	143,562
Number of nodes	414,875
Analysis type	Small Displacement Static
Total mass	1864.54 g

Table 5.12 Finite element model information of the beam structure and ABA

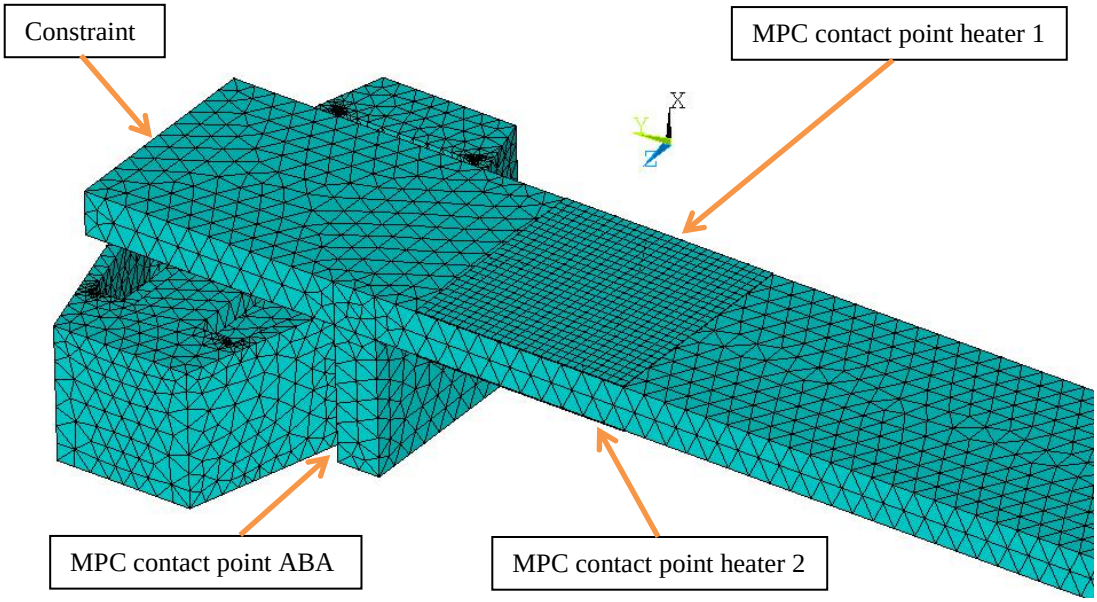

Figure 5.18 Partial view of the generated finite element model of the beam structure and the ABA

5.4.1 Post-Processing the Solution Results of the ABA Structure

The displacement of the beam structure is acquired by executing the PATH operation in the post-processor. The generated path contains 200 data points. The X-component of displacement is then mapped onto the path.

Figure 5.19 and Figure 5.20 illustrate the X-component of displacement of the beam structure, acquired from the first three and last three solution phases, respectively. In Phase 1, 2 and 3 the model is solved for the displacement, where the beam structure deforms in an upward direction, caused by the thermal loading. The displacement of the beam structure caused by the thermal loading, simulated in

Phase 1, has a value of $291E^{-6}$ m. The generated displacement by the ABA, simulated in Phase 2, has a value of $-336E^{-6}$ m. In Phase 3, the model is solved for the displacement where the beam structure is subjected to both thermally induced heating and ABA actuation. The displacement of the structure in this phase has a value of $-45.7E^{-6}$ m, which indicates that the ABA is over compensating the structure. In Phases 4, 5 and 6, described in Table 5.11, the model is solved for the displacement where the beam structure deforms in a downward direction, which is caused by the thermally induced loading. The beam exhibits a displacement of $-674E^{-6}$ m under the thermal loading, simulated in Phase 4, whereas the ABA generates a displacement of $272E^{-6}$ m, which is simulated in Phase 5. The maximum displacement that occurs when the beam structure is compensated for the thermal deformation that is simulated in Phase 6 is $-402E^{-6}$ m.

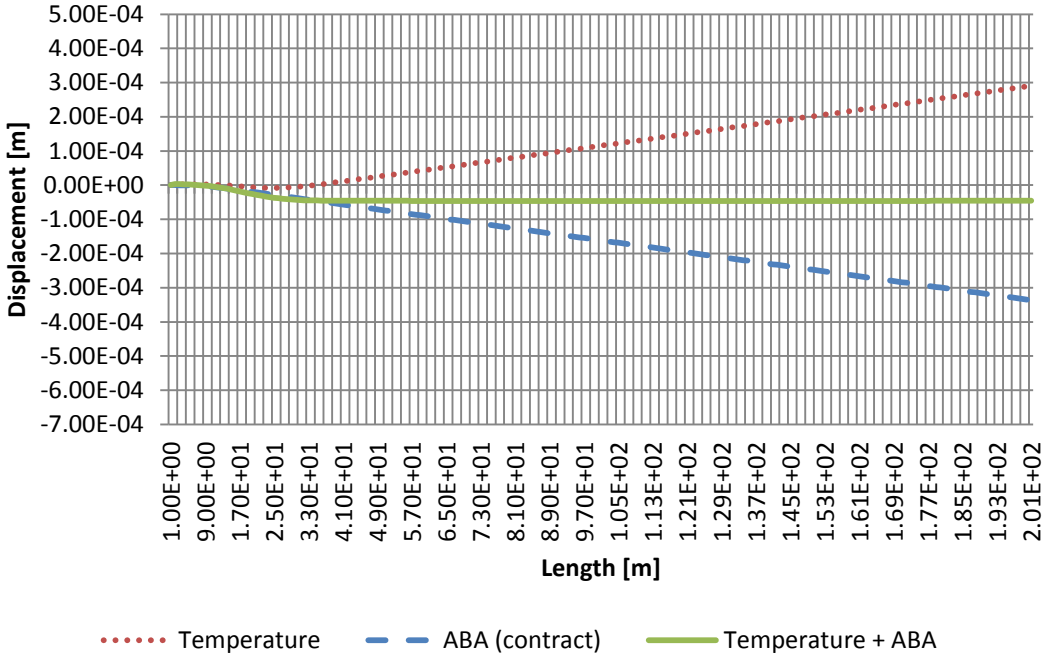

Figure 5.19 X-component of displacement exhibited by the ABA structure for the solution Phases 1, 2, and 3, described in Table 5.11

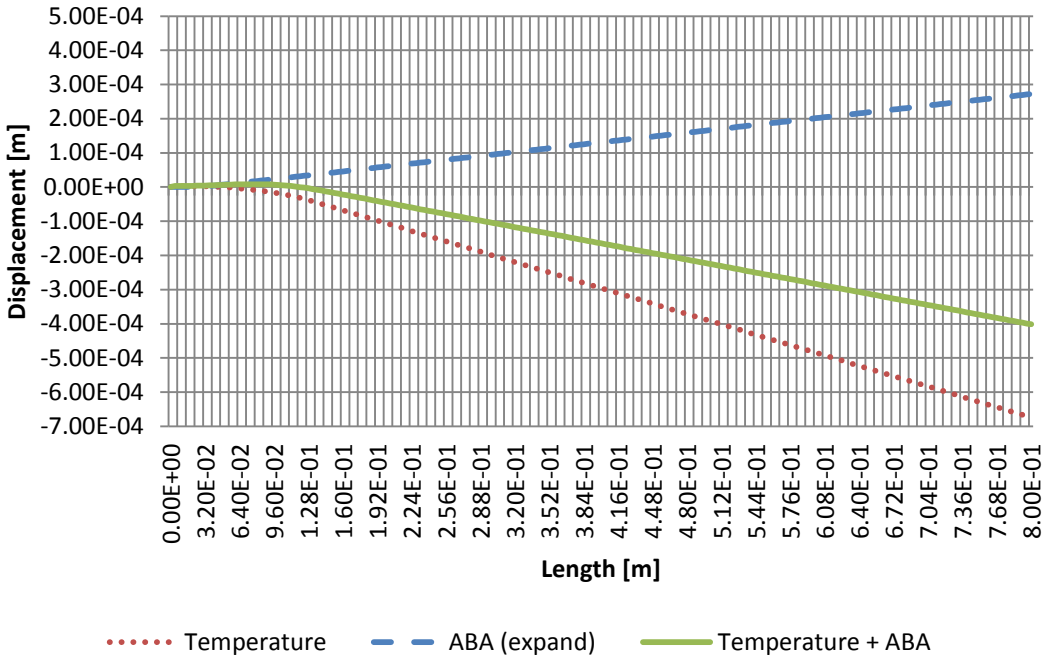

Figure 5.20 X-component of displacement exhibited by the ABA structure for the solution Phases 4, 5, and 6, described in Table 5.11

A summary of the compensation values is given by Table 5.13, which demonstrates that the ABA is able to compensate the beam structure when it deforms upwards. A compensation of 40% is achieved, by the ABA, when the structure deforms in a downward direction. The reason that the compensation percentages are not identical to each other is the fact that the structure is not symmetrical, since the ABA is mounted to the rib on the bottom side of the structure. However, the compensation performance of the actuator, described in Table 5.13(b), demonstrates a 10% increase, when the results of the ABA are compared against the results of the ADSA, which are described in Table 4.20(b). Therefore, the compensation percentages generated by the ABA are closer together than the compensation percentages of the ADSA.

The most significant improvement is illustrated by Figure 5.21, which demonstrates the displacement of the beam generated by the ABA, when it expands, contracts or remains in its neutral position.

Structure demonstrates upward deformation caused by thermal loading		
Thermal displacement [m]	Compensated displacement [m]	Compensation percentage
$291E^{-6}$	$-45.7E^{-6}$	115.7%

(a)

Structure demonstrates downward deformation caused by thermal loading		
Thermal displacement [m]	Compensated displacement [m]	Compensation percentage
$-674E^{-6}$	$-402E^{-6}$	40.4%

(b)

Table 5.13 (a) Compensation results of the ABA where the structure deflects upward [m]; (b) Compensation results of the ABA where the structure deflects downward [m]

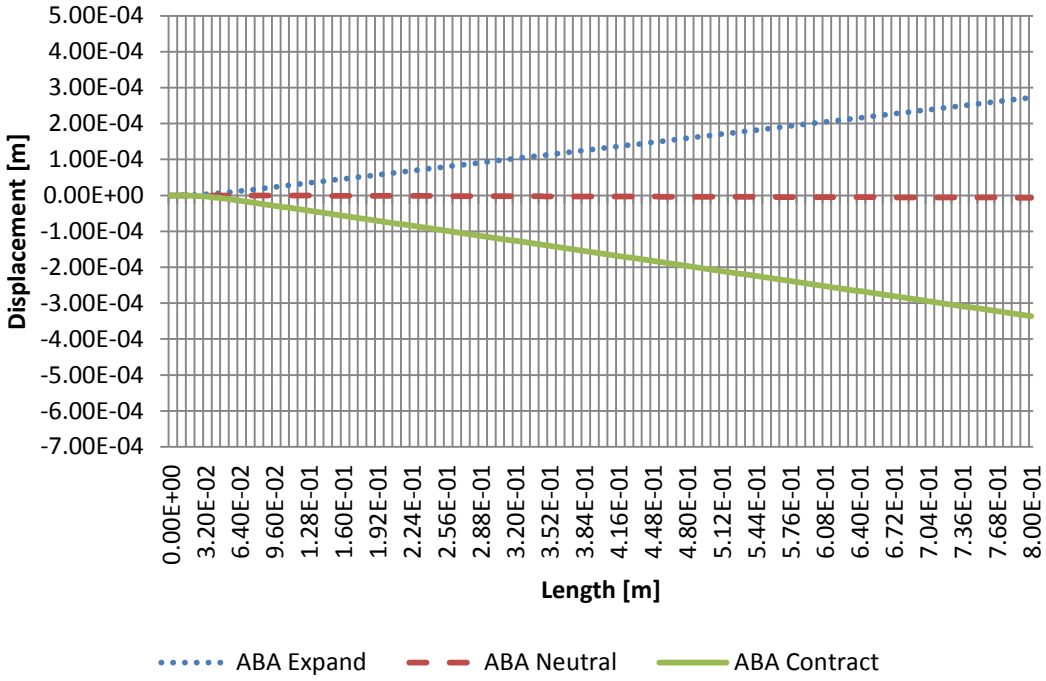

Figure 5.21 X-component of displacement exhibited by the beam structure subjected to ABA actuation

The displacement of the beam structure, when the ABA remains in its neutral position, is represented by the red dashed line in Figure 5.21, and has a value of $-6.41E^{-6}$ m, whereas the ADSA generates a displacement of $-138E^{-6}$ m. This is an improvement of 95%, which makes the ABA more suitable for shape control applications than the ADSA.

A comparison between the compensation performances of the ABA and ADSA is given in Table 5.14. The compensation generated by the ABA, in Phase 3, is less than the generated compensation by the ADSA. However, the ABA is able to generate a larger compensation in Phase 6. Therefore, the compensation performances of the ABA, generated in Phase 3 and 6, are closer together compared to the ADSA. The largest improvement of the ABA is its ability to generate almost zero displacement in its neutral position. The neutral position preloads the piezoelectric stacks employed inside the ABA and, therefore, eliminates the use of a preload spring.

	ADSA	**ABA**	**Improvement**
Compensation Phase 3	122.26%	115.72%	−6.54%
Compensation Phase 6	28.99%	40.40%	11.41%
Displacement in neutral position	$-138E^{-6}$ m	$-6.41E^{-6}$ m	95.36%

Table 5.14 Comparison between the compensation performances of the ADSA and ABA in Phase 3 and 6, described in Table 5.11, and the displacement generated in the neutral position

5.5 Chapter Summary

A novel bidirectional actuator is proposed in this chapter. The bidirectional actuator employs identical piezoelectric stacks, as used in the dual-stack actuator discussed in Chapter 4, in order to make a fair comparison. The configuration of the piezoelectric stacks in the bidirectional actuator is optimised, to achieve identical pulling and pushing displacements and to eliminate the use of a DC-bias voltage. FEM analyses are conducted to identify the behaviour and performance of the bidirectional actuator and demonstrate that the actuator is able to generate identical pulling and pushing displacements without the need of a DC-bias. A small electrical field is applied to both piezoelectric stacks, when the bidirectional actuator remains in its neutral position, to allow active preloading, thus eliminating the use of a preload spring.

The bidirectional actuator is then mounted into a diamond-shaped compliant structure in order to amplify the bidirectional displacements, which forms the amplified bidirectional actuator (ABA). FEM analyses are conducted, which demonstrate that the bidirectional displacements are doubled. The results are then compared to the ADSA. The comparison demonstrates that the ABA is able to generate a bidirectional actuation without the use of a DC-bias, which makes the ABA more suitable for shape control applications.

In order to compare the compensation performance of the ABA to the ADSA, the ABA is mounted onto a beam structure that is subjected to a thermally induced loading. The beam structure is identical to the structure used for the benchmark model and the ADSA. The achieved compensation performance of the ABA, for upwards and downwards thermal induced deformation, is simulated to be 116% and 40%, respectively. Comparing these results to the compensation percentages achieved by the ADSA, demonstrates that the compensation performances of the ABA are closer together. The most significant improvement of the ABA, compared to the ADSA, is the elimination of the distortion caused by the DC-bias voltage.

The finite element analyses in this chapter provide a clear understanding of the behaviour and actuation performance of the bidirectional actuator and amplified bidirectional actuator. Furthermore, the results of the conducted analyses demonstrate that the proposed bidirectional actuator and the ABA are more suitable

to minimise the deformation of a structure that is subjected to thermally induced loading.

Chapter 6

Summary, Conclusion and Future Work

6.1 Summary

Increasingly, engineers are pushing the boundaries of aerospace vehicles to fly at hypersonic speeds of Mach 10. However, flying at these speeds introduces aerothermoelastic problems, since the skin of the hypersonic vehicle is subjected to friction with the hypersonic airstream, which causes the skin to deform as well as melting of the leading edges of the vehicle. The attention has focussed on active means of controlling this deformation by employing a smart material.

Controlling the shape of a structure, induced by thermal loading, remains a challenging task, since the high temperature influences the actuation performance of the smart material. The material is activated by an external stimulus, typically an electrical field. The amount of actuation depends on the strength of the applied external stimulus. However, when shape control is applied to aerospace structures, the possibility of generating a large amount of external stimulus is not always guaranteed. The distortions caused by the thermal loading are bidirectional, forcing the structure to exhibit an upward or downward displacement. The challenge arises that most smart materials, used for shape control, exhibit unidirectional or semi-

bidirectional displacements and, therefore, only compensate for shape distortions in one direction. To overcome this challenge, the smart material can be mounted to both sides of the structure, for example, inside and outside the skin of a hypersonic vehicle. However, given the thermal considerations, it is not desired to mount the smart material on the outside surface of the skin of a vehicle, since it will result in loss of actuation performance. The aim of this research is to develop a bidirectional actuator that can be mounted to the internal frame of a structure, to compensate for the displacement generated by the thermally induced loading.

The literature surveyed in the course of this research reveals that piezoelectric ceramics are the most suitable material to control the shape of a thermally induced structure. Piezoelectric materials are able to generate high forces and can be used for applications, from near static to high frequency dynamics, with a fast response time. The most promising methodology to achieve an amplified bidirectional actuation appears to be the combination of a piezoelectric ceramic with a compliant structure.

In this thesis, two amplified bidirectional actuators are proposed, namely: the Amplified Dual-Stack Actuator (ADSA), and the Amplified Bidirectional Actuator (ABA). Both actuators consist of a diamond-shaped amplifying compliant mechanism to amplify the generated displacements of the actuators. It is claimed that the proposed ABA is able to compensate the shape of a thermally induced structure, when it is mounted to only one side of the structure. In order to justify this claim, the following summary of the work undertaken is presented.

Dual-Stack Actuator

The dual-stack actuator, developed by Heverly *et al.* [41] was chosen as the basis for the proposed amplified bidirectional actuators. The dual-stack actuator employs two piezoelectric stacks, which consist of ring elements. The stacks are operated in opposing fashion, i.e. when Stack 1 contracts, Stack 2 extends, and vice versa. The stacks are connected to each other by a piston, and encapsulated by a compliant mechanism to generate the bidirectional displacements. To achieve comparable contracting and extending displacements, the electrical fields applied to both piezoelectric stacks are operated around a DC-bias. The magnitude of the DC-bias is acquired by dividing the total electrical field range, applied to the piezoelectric stack,

in half. Therefore, the dual-stack actuator always experiences a compressive stress, caused by the DC-bias in the neutral position, which eliminates the need for mechanical preloading.

A finite element model of the Heverly *et al.* [41] dual-stack actuator is built in ANSYS in order to identify its behaviour, free displacement and blocked force values. The free displacement is simulated for the contracted, neutral and extended positions. The simulation results demonstrate that the piston deforms, due to the generated force by the piezoelectric stacks. Hence, the free displacement, generated by the dual-stack actuator in the contracted position, is less than the generated free displacement, in the extended position. However, when the dual-stack actuator remains in its neutral position, it generates a small displacement in the extending direction, which is caused by the DC-bias. Therefore, the bidirectional free displacements, i.e. the differences between the neutral and the contracted and extended positions, are identical.

The blocked force of the actuator is identified by blocking the motion of the actuator during pulling and pushing actuation, while applying the maximum electrical field. A large difference is identified when the FEM-computed blocked force is compared to the blocked force reported in the paper of Heverly *et al*. [41]. The reason for this difference is that Heverly *et al*. [41] defined the blocked force in their study as the difference between the extended and contracted position and, therefore, compressing the piezoelectric stack past its neutral point. However, the conventional way of measuring the blocked force, as used in this thesis, is to constrain the stack to zero, or, in the case of the dual-stack actuator, the neutral position.

The FEM simulations demonstrate that the dual-stack actuator is able to generate equal bidirectional displacements. However, the bidirectional displacements are limited and are only half the displacement of a single piezoelectric stack. In order to compensate the shape of a structure, affected by thermally induced loading, a large displacement is required. Therefore, the dual-stack actuator is mounted within a diamond-shaped amplifying compliant mechanism that amplifies the displacement.

Amplified Dual-Stack Actuator (ADSA)

A diamond-shaped amplifying compliant structure is utilised to amplify the bidirectional displacements of the dual-stack actuator. The compliant structure is easy to manufacture and does not contain any movable parts. Instead, flexible hinges are used to reduce the wear and tear of the structure. The dimensions of the compliant structure are theoretically estimated, based on the desired amplification factor. The calculations demonstrate that the amplification factor depends on the length and height ratio of the compliant structure. Amplification is achieved by making the length n times greater than the height. The amplification factor is limited by the height of the compliant mechanism, where the displacement δ must be smaller than the height h of the compliant structure.

The solution results of the FEM-computed free displacements demonstrate that the compliant structure amplifies the free displacements of the dual-stack actuator by approximately 2.37 times. The theoretically calculated amplification factor is estimated to be 2.40 times. This small error is caused by the assumption that the arms of the compliant mechanism do not flex, which is not the case. The error in calculation can be reduced by making the structure thinner at the hinges. As a result, more displacement will be achieved. The bidirectional displacements, which are acquired by taking the difference between the contracted and neutral position or the expanded and neutral position, are identical in value.

The method to simulate the blocked force of the ADSA is identical to the method used to simulate the blocked force of the dual-stack actuator. As a consequence of the trade-off between the blocked force and the free displacement, the simulated blocked force of the ADSA is significantly lower than to the blocked force of the dual-stack actuator. In order to identify the compensation performance of the ADSA, a FEM benchmark model is built.

Performance of ADSA vs. Benchmark Model

The benchmark model contains a beam structure with two film heaters mounted onto each side of the structure, to induce a through-the-thickness thermal gradient. As a result, the beam deforms in an upward or downward direction. Two piezoelectric

patches are used to compensate for the thermally induced deformation, which are also mounted onto each side of the beam.

The thermal loads are applied to the structure and the deformation is simulated. The piezoelectric patches are then enabled and the displacement is identified, while the structure is still experiencing the thermal loads. The amount of compensation is acquired by calculating the difference in displacements of both simulations. The compensation performance of the piezoelectric patches serves as a benchmark to identify the performance of the ADSA. The ADSA is mounted onto an identical beam structure, as used in the benchmark model. The compensation performance of the ADSA is simulated, using identical loads, as employed in the benchmark model.

Both piezoelectric patches are able to compensate the deformation of the beam structure for approximately 11%. One single ADSA is able to compensate the deformation of the structure, in the upward and downward direction, for approximately 122% and 29%, respectively. Comparing the compensation results of the ADSA, to the compensation results of the piezoelectric patches, demonstrates that the ADSA is able to generate a much larger compensation. One reason that the compensation results of the ADSA vary, is that the ADSA is mounted onto the bottom side of the structure. The structure is therefore not symmetrical, resulting in a variation in compensation. The most significant factor, which causes the difference in compensation, is the fact that the neutral position is not taken into account. The dual-stack actuator is only able to generate identical bidirectional displacements by taking the difference between the contracted and neutral positions and the extended and neutral positions. However, the simulations demonstrate that the dual-stack actuator and ADSA generate a displacement in the neutral position, which is caused by the DC-bias. This displacement is undesired, since the ADSA excites the beam structure, when it is not subjected to any thermal loads. Another drawback of the applied DC-bias is the unnecessary power consumption in the neutral position. Therefore, both actuators, which cannot perform an identical bidirectional actuation without the application of a DC-bias, are not ideal for shape control of structures subjected to thermal loading. To overcome this problem, a novel bidirectional actuator and amplified bidirectional actuator are proposed.

Bidirectional Actuator

A bidirectional actuator is designed with the aim of eliminating the DC-bias voltage, while still exhibiting equal displacements and blocked forces. The bidirectional actuator employs two identical piezoelectric stack elements as used in the dual-stack actuator. The configuration of the piezoelectric stacks in the bidirectional actuator is optimised, which eliminates the need for a DC-bias voltage. A FEM model is built and the free displacement and blocked force values of the bidirectional actuator are identified, by applying identical loads, as applied to the dual-stack actuator. To achieve active preloading of the bidirectional actuator, and therefore eliminate the need for a preload spring, a small electrical field is applied to the bidirectional actuator in the neutral position. The applied electrical field is 80% less than the electrical field applied to the dual-stack actuator, which results in a more efficient actuator.

The FEM simulations demonstrate that the bidirectional actuator is able to generate identical contracting and extending displacements, whereas the undesired displacement generated in the neutral position, is reduced by 99%. The blocked force values of the bidirectional actuator are slightly reduced, by approximately 8.5%, compared to the values of the dual-stack actuator. To amplify the displacement values of the bidirectional actuator, it is mounted into a diamond-shaped amplifying compliant structure.

Amplified Bidirectional Actuator

A new compliant structure is developed, according to the dimensions of the bidirectional actuator, and the FEM model of the bidirectional actuator is expanded. The amplification factor of the compliant structure is theoretically estimated to be 2.26 times.

The acquired free displacement values, generated by the ABA, demonstrate a difference of approximately $4E^{-6}$ m in the pulling and pushing directions. This variation in displacement is caused by the way the bidirectional actuator is mounted into the compliant structure. However, a great advantage of the ABA over the ADSA is the significantly reduced displacement by 96% in the neutral position.

The FEM-computed blocked force values of the ABA vary from each other by

21%. Comparing the results of the ABA against the ADSA, demonstrates the advantage of the ABA, with blocked force values differing by only 21% without the use of a DC-bias voltage, compared to the difference of 94% of the ADSA. To identify the compensation performance of the ABA, it is mounted to an identical beam structure as used in the benchmark model.

Performance of ABA vs. ADSA and Benchmark model

The ABA is mounted to an identical beam structure as used in the benchmark model, and the compensation performance is identified using identical loads, as used in the benchmark model. Therefore, it is possible to compare the compensation results of the piezoelectric patches, ADSA and ABA against each other.

The achieved compensation performance of the ABA, when the structure deforms in the upward and downward direction, is simulated to be 116% and 40%, respectively. Comparing these results, to the compensation percentages achieved by the ADSA, shows that the compensation percentages of the ABA are closer together. However, the most significant improvement of the ABA, compared to the ADSA, is the elimination of the DC-bias voltage. This results in a decrease of displacement of the beam structure generated by the actuator, in the neutral position, by 95%.

The conducted finite element simulations provide a clear understanding of the behaviour of the ABA and demonstrate that the ABA is superior to the ADSA, when the actuator is applied to compensate the shape of a thermally distorted structure. Moreover, the ABA does not need a DC-bias to generate almost identically pulling and pushing actuations, which results in lower power consumption and more efficiency.

6.2 Conclusion

The outcomes of this research provide a basis for further development of bidirectional actuators to control and minimise the shape of thermally distorted structures. The results of the finite element method simulations demonstrate that the actuators, i.e. the dual-stack actuator, the amplified dual-stack actuator (ADSA), the

bidirectional actuator and the amplified bidirectional actuator (ABA), are all able to generate a bidirectional actuation.

From the simulations, it can be concluded that, although the ADSA is able to generate an amplified bidirectional actuation as a consequence of the DC-bias voltage, it is not suitable to compensate the shape of a thermally distorted structure. This voltage is set to be half the maximum applied voltage. Hence, the actuators are actively preloaded to protect the piezoelectric stacks from tensile stresses. The applied DC-bias causes the ADSA to contract, which causes the structure to excite an undesirable displacement.

The finite element simulations demonstrate that the proposed ABA is able to generate a bidirectional actuation, without the need for a DC-bias. The ABA is actively preloaded to eliminate the need of a preload spring. Therefore, the ABA is more suitable to compensate and minimise the deformation of a structure subjected to thermal loading, in comparison to the ADSA.

6.3 Recommendations for Future Work

A number of recommendations for future research can be made, based on the results of this thesis.

In this study, the behaviour and performance of the actuators are based on theoretical calculations and FEM computations. Both calculations and computations are based on the material data provided by the manufacturer. Unfortunately, it is virtually impossible to exactly model piezoelectric stacks according to the specified piezoelectric data. In addition, due to the ferroelectric nature of PZT-ceramics, the specified piezoelectric data can vary significantly with the operating electrical field strength [18]. Furthermore, the FEM simulations in this study are linear. However, in practice, piezoelectric materials exhibit a small hysteresis, which is not taken into account in the FEM simulations. The hysteresis does not affect the values of the free displacements, as concluded in the study of Medid and Lim [69], and blocked force as such, since these are the maximum values.

However, the hysteresis starts to play a significant role when the voltages are varied. Therefore, it is suggested that a practical validation of the performance, free displacements and blocked forces of the amplified bidirectional actuator (ABA), be conducted.

The generated displacements by the ABA are of the order of microns. It is therefore important that, in the fabrication of the ABA, a minimum number of screw connections be used since each connection makes the material weaker and, therefore, dissipates a certain amount of the displacement.

It is recommended to verify the compensation performance of the ABA, by mounting the actuator onto a beam structure that is subjected to thermal loading. The heat can be induced by two film heaters that are bonded onto each surface of the structure. The temperature of the film heaters can be controlled with a temperature controller, which controls the temperature of the film heaters according to a pre-set value. Initially, the displacement of the beam can be measured using strain gauges or a laser displacement sensor. By measuring the deformation of the structure generated by the film heaters, the displacement of the structure generated by the ABA and the compensated displacement, it is possible to make a comparison between the measured displacement values and the FEM-computed values.

The development of a control method to actively monitor and control the deformation of the beam structure, generated by the thermally induced heating, could be a promising research direction. The measured deformation, by the strain gauges or the laser displacement sensor of the beam structure, can serve as feedback for the controller. However, the use of the ABA as a sensor and actuator, known as a sensoriactuator, can be considered as an alternative solution. Additional circuitry can be developed to minimise the hysteresis of the ABA.

The housing and diamond-shaped amplifying compliant structure, are developed out of the reasonably heavy material stainless steel 304. Research into stronger and lightweight materials may be useful in obtaining further reduction of the ABA's weight.

This work serves as a foundation study to examine the potential of using amplified bidirectional actuators to control the shape of thermally distorted structures, e.g. the skin of a hypersonic vehicle subjected to friction of the air. Once

the validation tests are performed, to corroborate the simulation results presented in this thesis, the next step will be to create a larger test structure to identify the real-time compensation results of the structure.

Appendix A

Material Properties

This appendix describes the material data used in the FEM software ANSYS. In Section 3.2, two initial bidirectional actuator configurations are analysed. The piezoelectric stack elements, employed in both models, are of the type PZT-5H. As previously described in Section 2.2.2, a piezoelectric stack is modelled by employing two material types, where one material has the opposite signs to the others for the values of the piezoelectric matrix. Table A.1 and Table A.2 describe the piezoelectric material data, derived from [70], used to model the horizontal piezoelectric stacks, illustrated by Figure 3.4 and Figure 3.5. The material data in Table A.1 and Table A.2 are defined as Material 1 and 2, respectively. It does not matter which material number is used to define the material, as long as each material in the analysis has its own unique material number. Both tables describe the material data for the PZT-5H material, which is polarised in the X-direction. The material data, described in Table A.3 and Table A.4, is for the same PZT-5H material. However, the polarisation direction is changed to the Y-direction. The material data, described in the tables, is used to model the vertical piezoelectric stacks, illustrated by Figure 3.5.

/com	**PZT-5H**	**X-polarised**				
/com	Stiffness					
TB,	ANEL,	1	,	1	,	0
TBDATA,	1,	1.1744E+11	,	8.4670E+10	,	8.4670E+10
TBDATA,	7,	1.2720E+11	,	8.0212E+10		
TBDATA,	12,	1.2720E+11				
TBDATA,	16,	2.2989E+10				
TBDATA,	19,	2.3474E+10				
TBDATA,	21,	2.2989E+10				
/com	Piezo matrix					
TB,	PIEZ,	1				
TBDATA,	1,	23.2403				
TBDATA,	4,	-6.6228				
TBDATA,	7,	-6.6228				
TBDATA,	11,	17.0345				
TBDATA,	18,	17.0345				
/com	Permittivity					
EMUNIT,	EPZRO,	8.85E-12				
MP,	PERX,	1	,	1434		
MP,	PERY,	1	,	1704		
MP,	PERZ,	1	,	1704		
/com	Density					
MP,	DENS,	1	,	7500		

Table A.1 Material properties of PZT-5H, X-polarised, defined as Material 1, used to model the horizontal piezoelectric stacks in Figure 3.4 and Figure 3.5

/com	**PZT-5H**	**X-polarised**		**Inverted**		
/com	Stiffness					
TB,	ANEL,	2	,	1	,	0
TBDATA,	1,	1.1744E+11	,	8.4670E+10	,	8.4670E+10
TBDATA,	7,	1.2720E+11	,	8.0212E+10		
TBDATA,	12,	1.2720E+11				
TBDATA,	16,	2.2989E+10				
TBDATA,	19,	2.3474E+10				
TBDATA,	21,	2.2989E+10				
/com	Piezo matrix					
TB,	PIEZ,	2				
TBDATA,	1,	-23.2403				
TBDATA,	4,	6.6228				
TBDATA,	7,	6.6228				
TBDATA,	11,	-17.0345				
TBDATA,	18,	-17.0345				
/com	Permittivity					
EMUNIT,	EPZRO,	8.85E-12				
MP,	PERX,	2	,	1434		
MP,	PERY,	2	,	1704		
MP,	PERZ,	2	,	1704		
/com	Density					
MP,	DENS,	2	,	7500		

Table A.2 Material properties of PZT-5H, X-polarised, defined as Material 2 with inverted piezoelectic matrix, used to model the horizontal piezoelectric stacks in Figure 3.4 and Figure 3.5

```
/com      PZT-5H      Y-polarised

/com      Stiffness
TB,       ANEL,              4  ,            1  ,           0
TBDATA,   1,          1.2720E+11  ,  8.4670E+10  ,  8.0212E+10
TBDATA,   7,          1.1744E+11  ,  8.4670E+10
TBDATA,   12,         1.2720E+11
TBDATA,   16,         2.2989E+10
TBDATA,   19,         2.2989E+10
TBDATA,   21,         2.3474E+10

/com      Piezo matrix
TB,       PIEZ,              4
TBDATA,   2,            -6.6228
TBDATA,   5,            23.2403
TBDATA,   8,            -6.6228
TBDATA,   10,           17.0345
TBDATA,   15,           17.0345

/com      Permittivity
EMUNIT,   EPZRO,      8.85E-12
MP,       PERX,              4  ,         1704
MP,       PERY,              4  ,         1434
MP,       PERZ,              4  ,         1704

/com      Density
MP,       DENS,              4  ,         7500
```

Table A.3 Material properties of PZT-5H, Y-polarised, defined as Material 4, used to model the vertical piezoelectric stacks in Figure 3.5

/com	**PZT-5H**	**Y-polarised**		**Inverted**		
/com	Stiffness					
TB,	ANEL,	5	,	1	,	0
TBDATA,	1,	1.2720E+11	,	8.4670E+10	,	8.0212E+10
TBDATA,	7,	1.1744E+11	,	8.4670E+10		
TBDATA,	12,	1.2720E+11				
TBDATA,	16,	2.2989E+10				
TBDATA,	19,	2.2989E+10				
TBDATA,	21,	2.3474E+10				
/com	Piezo matrix					
TB,	PIEZ,	5				
TBDATA,	2,	6.6228				
TBDATA,	5,	-23.2403				
TBDATA,	8,	6.6228				
TBDATA,	10,	-17.0345				
TBDATA,	15,	-17.0345				
/com	Permittivity					
EMUNIT,	EPZRO,	8.85E-12				
MP,	PERX,	5	,	1704		
MP,	PERY,	5	,	1434		
MP,	PERZ,	5	,	1704		
/com	Density					
MP,	DENS,	5	,	7500		

Table A.4 Material properties of PZT-5H, Y-polarised, defined as Material 5 with inverted piezoelectric matrix, used to model the horizontal piezoelectric stacks in Figure 3.5

The proposed actuators, discussed and simulated in Chapter 4 and Chapter 5, are modelled using identical piezoelectric stack elements. The stack elements are manufactured by American Piezo Ceramics, and are of type: HPst 150/14-10/25. The material properties of the stacks, used to conduct the FEM simulations in ANSYS, are derived from the manufacture's specifications, specified in [18], and described in six tables. The tables define the material for the X, Y and Z polarisation directions, where each polarisation direction contains a piezoelectric matrix and inverted piezoelectric matrix.

The material data described in Table A.5 and Table A.6 defines the properties for the piezoelectric material polarised in the X-direction. This data is used in the FEM simulations of the bidirectional actuator and ABA, illustrated by Figure 5.4 and Figure 5.12, respectively. Note that the geometry and orientation of the model determine the polarisation direction of the piezoelectric material. It is therefore the designer's responsibility to build the piezoelectric stack in ANSYS according to the polarisation direction of the specified material.

Table A.7 and Table A.8 represent the defined properties for the piezoelectric material polarised in the Y-direction. The material data is used to simulate the dual-stack actuator, illustrated in Figure 4.7, and the piezoelectric patches that are employed in the benchmark model, illustrated in Figure 4.21.

The material data, described in Table A.9 and Table A.10, describe the properties for the piezoelectric material polarised in the Z-direction. This data is used to model the ADSA, illustrated in Figure 4.15. In addition, the data is used in the FEM simulations to identify the compensation performance of the ADSA and ABA, illustrated by Figure 4.25 and Figure 5.18, respectively.

The dimensions and relevant specifications of the piezoelectric stack, which are listed by the manufacturer in [71], are described in Table A.11.

```
/com      PSt 150      X-polarised

/com      Stiffness
TB,       ANEL,                1  ,            1  ,            0
TBDATA,   1,           2.5987E+11  ,  2.1916E+11  ,  2.1916E+11
TBDATA,   7,           2.6025E+11  ,  2.0918E+11
TBDATA,   12,          2.6025E+11
TBDATA,   16,          2.2989E+10
TBDATA,   19,          2.3474E+10
TBDATA,   21,          2.2989E+10

/com      Piezo matrix
TB,       PIEZ,                1
TBDATA,   1,             37.9101
TBDATA,   4,              3.0280
TBDATA,   7,              3.0280
TBDATA,   11,            17.0345
TBDATA,   18,            17.0345

/com      Permittivity
EMUNIT,   EPZRO,        8.85E-12
MP,       PERX,                1  ,          880
MP,       PERY,                1  ,         1704
MP,       PERZ,                1  ,         1704

/com      Density
MP,       DENS,                1  ,         8000

/com      THERMAL CONDUCTIVITY  W M^-1 C^-1
MP,       KXX,    1,    1.5

/com      SPECIFIC HEAT J KG^-1 C^-1
MP,       C,      1,    380

/com      THERMAL EXPANSION COEFFICIENT C^-1
MP,       ALPX,   1,    0.4E-5
```

Table A.5 Material properties of HPst 150, X-polarised, defined as Material 1, used to model the bidirectional actuator and ABA, illustrated in Figure 5.4 and Figure 5.12, respectively

/com	**PSt 150**	**X-polarised**		**Inverted**		
/com	Stiffness					
TB,	ANEL,	2	,	1	,	0
TBDATA,	1,	2.5987E+11	,	2.1916E+11	,	2.1916E+11
TBDATA,	7,	2.6025E+11	,	2.0918E+11		
TBDATA,	12,	2.6025E+11				
TBDATA,	16,	2.2989E+10				
TBDATA,	19,	2.3474E+10				
TBDATA,	21,	2.2989E+10				
/com	Piezo matrix					
TB,	PIEZ,	2				
TBDATA,	1,	-37.9101				
TBDATA,	4,	-3.0280				
TBDATA,	7,	-3.0280				
TBDATA,	11,	-17.0345				
TBDATA,	18,	-17.0345				
/com	Permittivity					
EMUNIT,	EPZRO,	8.85E-12				
MP,	PERX,	2	,	880		
MP,	PERY,	2	,	1704		
MP,	PERZ,	2	,	1704		
/com	Density					
MP,	DENS,	2	,	8000		
/com	THERMAL CONDUCTIVITY W M^-1 C^-1					
MP,	KXX,	2,	1.5			
/com	SPECIFIC HEAT J KG^-1 C^-1					
MP,	C,	2,	380			
/com	THERMAL EXPANSION COEFFICIENT C^-1					
MP,	ALPX,	2,	0.4E-5			

Table A.6 Material properties of HPst 150, X-polarised, defined as Material 2 with inverted piezoelectric matrix, used to model the bidirectional actuator and ABA, illustrated in Figure 5.4 and Figure 5.12, respectively

```
/com      PSt 150      Y-polarised

/com      Stiffness
TB,       ANEL,                1  ,            1  ,            0
TBDATA,   1,           2.6025E+11  ,  2.1916E+11  ,  2.0918E+11
TBDATA,   7,           2.5987E+11  ,  2.1916E+11
TBDATA,   12,          2.6025E+11
TBDATA,   16,          2.2989E+10
TBDATA,   19,          2.2989E+10
TBDATA,   21,          2.3474E+10

/com      Piezo matrix
TB,       PIEZ,                1
TBDATA,   2,                3.0280
TBDATA,   5,               37.9101
TBDATA,   8,                3.0280
TBDATA,   10,              17.0345
TBDATA,   15,              17.0345

/com      Permittivity
EMUNIT,   EPZRO,        8.85E-12
MP,       PERX,                1  ,         1704
MP,       PERY,                1  ,          880
MP,       PERZ,                1  ,         1704

/com      Density
MP,       DENS,                1  ,         8000

/com      THERMAL CONDUCTIVITY  W M^-1 C^-1
MP,       KXX,    1,    1.5

/com      SPECIFIC HEAT J KG^-1 C^-1
MP,       C,      1,    380

/com      THERMAL EXPANSION COEFFICIENT C^-1
MP,       ALPX,   1,    0.4E-5
```

Table A.7 Material properties of HPst 150, Y-polarised, defined as Material 1, used to model the dual-stack actuator and PZT patches, illustrated in Figure 4.7 and Figure 4.21, respectively

```
/com      PSt 150      Y-polarised      Inverted
/com      Stiffness
TB,       ANEL,                2  ,           1  ,           0
TBDATA,   1,           2.6025E+11  ,  2.1916E+11  ,  2.0918E+11
TBDATA,   7,           2.5987E+11  ,  2.1916E+11
TBDATA,   12,          2.6025E+11
TBDATA,   16,          2.2989E+10
TBDATA,   19,          2.2989E+10
TBDATA,   21,          2.3474E+10

/com      Piezo matrix
TB,       PIEZ,                2
TBDATA,   2,               -3.0280
TBDATA,   5,              -37.9101
TBDATA,   8,               -3.0280
TBDATA,   10,             -17.0345
TBDATA,   15,             -17.0345

/com      Permittivity
EMUNIT,   EPZRO,           8.85E-12
MP,       PERX,                2  ,        1704
MP,       PERY,                2  ,         880
MP,       PERZ,                2  ,        1704

/com      Density
MP,       DENS,                2  ,        8000

/com      THERMAL CONDUCTIVITY  W M^-1 C^-1
MP,       KXX,     2,     1.5

/com      SPECIFIC HEAT J KG^-1 C^-1
MP,       C,       2,     380

/com      THERMAL EXPANSION COEFFICIENT C^-1
MP,       ALPX,    2,     0.4E-5
```

Table A.8 Material properties of HPst 150, Y-polarised, defined as Material 2 with inverted piezoelectric matrix, used to model the dual-stack actuator illustrated in Figure 4.7

```
/com     PSt 150     Z-polarised

/com     Stiffness
TB,      ANEL,       1            ,  1            ,  0
TBDATA,  1,          2.6025E+11   ,  2.0918E+11   ,  2.1916E+11
TBDATA,  7,          2.6025E+11   ,  2.1916E+11
TBDATA,  12,         2.5987E+11
TBDATA,  16,         2.3474E+10
TBDATA,  19,         2.2989E+10
TBDATA,  21,         2.2989E+10

/com     Piezo matrix
TB,      PIEZ,       1
TBDATA,  3,          3.0280
TBDATA,  6,          3.0280
TBDATA,  9,          37.9101
TBDATA,  14,         17.0345
TBDATA,  16,         17.0345

/com     Permittivity
EMUNIT,  EPZRO,      8.85E-12
MP,      PERX,       1            ,  1704
MP,      PERY,       1            ,  1704
MP,      PERZ,       1            ,  880

/com     Density
MP,      DENS,       1            ,  8000

/com     THERMAL CONDUCTIVITY  W M^-1 C^-1
MP,      KXX,    1,      1.5

/com     SPECIFIC HEAT J KG^-1 C^-1
MP,      C,      1,      380

/com     THERMAL EXPANSION COEFFICIENT C^-1
MP,      ALPZ,   1,      0.4E-5
```

Table A.9 Material properties of HPst 150, Z-polarised, defined as Material 1, used to model the ADSA and the ADSA and ABA in the benchmark model, illustrated in Figure 4.15, Figure 4.25 and Figure 5.18, respectively

/com	**PSt 150**	**Z-polarised**	**Inverted**	
/com	Stiffness			
TB,	ANEL,	2	, 1	, 0
TBDATA,	1,	2.6025E+11	, 2.0918E+11	, 2.1916E+11
TBDATA,	7,	2.6025E+11	, 2.1916E+11	
TBDATA,	12,	2.5987E+11		
TBDATA,	16,	2.3474E+10		
TBDATA,	19,	2.2989E+10		
TBDATA,	21,	2.2989E+10		
/com	Piezo matrix			
TB,	PIEZ,	2		
TBDATA,	3,	-3.0280		
TBDATA,	6,	-3.0280		
TBDATA,	9,	-37.9101		
TBDATA,	14,	-17.0345		
TBDATA,	16,	-17.0345		
/com	Permittivity			
EMUNIT,	EPZRO,	8.85E-12		
MP,	PERX,	2	, 1704	
MP,	PERY,	2	, 1704	
MP,	PERZ,	2	, 880	
/com	Density			
MP,	DENS,	2	, 8000	
/com	THERMAL CONDUCTIVITY W M^-1 C^-1			
MP,	KXX,	2, 1.5		
/com	SPECIFIC HEAT J KG^-1 C^-1			
MP,	C,	2, 380		
/com	THERMAL EXPANSION COEFFICIENT C^-1			
MP,	ALPZ,	2, 0.4E-5		

Table A.10 Material properties of HPst 150, Z-polarised, defined as Material 2 with inverted piezoelectric matrix, used to model the ADSA and the ADSA and ABA in the benchmark model, illustrated in Figure 4.15, Figure 4.25 and Figure 5.18, respectively

Manufacturer	American Piezo Ceramics (APC)
Model	Low voltage ring actuator without casing
Type	HPst 150/14-10/25

Description	Value	Unit	Notes
Outer diameter	$15E^{-3}$	m	
Inner diameter	$9E^{-3}$	m	
Length	$27E^{-3}$	m	
Capacitance	$5.2E^{-6}$	F	
Stiffness	120	N/µm	
Resonance frequency	22	kHz	
Free displacement	$25E^{-6}$	m	measured at 0 to 150 V input voltage
	$32E^{-6}$	m	measured at −30 to 150 V input voltage
Blocked force	4500	N	measured at −30 to 150 V input voltage
Max. compressive force	6000	N	

Table A.11 HPSt 150/14-10/25 piezoelectric stack specifications [71]

The defined material properties for stainless steel 304, acquired from [67], are described in Table A.12. This material is used in the FEM simulations to model the diamond-shaped amplifying compliant mechanism and the housing of the dual-stack actuator and bidirectional actuator. The table demonstrates that there are piezoelectric properties defined. When conducting a structural-piezoelectric analysis using ANSYS, all the coupled-field elements, regardless of whether they have VOLT degrees of freedom, must be of piezoelectric types. Therefore, very small piezoelectric coefficients are specified for non-piezoelectric elements. Table A.13 describes the defined material data for aluminium 6061 T6 [72], which is used to model the beam structure. In addition, for this material, small piezoelectric coefficients are defined in order to use this material in a structural-piezoelectric analysis.

```
/COM   STAINLESS STEEL 304 MATERIAL PROPERTIES
MP,    DENS,    3,    7750       !DENSITY (KG M^-3)
MP,    EX,      3,    193E9      !YOUNGS MODULUS (PA)
MP,    NUXY,    3,    0.31       !POISSON'S RATIO
MP,    C,       3,    500        !SPECIFIC HEAT (J KG^-1 C^-1)
MP,    KXX,     3,    16.2       !THERMAL CONDUCTIVITY (W M^-1 C^-1)
MP,    ALPX,    3,    1.73E-5    !THERMAL EXPANSION COEFFICIENT (C^-1)

TB,    PIEZ,    3
TBDATA,         3,    0.1E-4
TBDATA,         6,    0.1E-4
TBDATA,         9,    0.1E-4
TBDATA,         14,   0.1E-4
TBDATA,         16,   0.1E-4

MP,    PERX,    3,    1E-3
MP,    PERY,    3,    1E-3
MP,    PERZ,    3,    1E-3
```

Table A.12 Material properties of stainless steel 304, defined as Material 3 [67]

```
/COM   ALU 6061 T6 MATERIAL PROPERTIES
MP,    DENS,    4,    2700       !DENSITY (KG M^-3)
MP,    EX,      4,    6.89E10    !YOUNGS MODULUS (PA)
MP,    NUXY,    4,    0.33       !POISSON'S RATIO
MP,    C,       4,    896        !SPECIFIC HEAT (J KG^-1 C^-1)
MP,    KXX,     4,    167        !THERMAL CONDUCTIVITY (W M^-1 C^-1)
MP,    ALPX,    4,    2.34E-5    !THERMAL EXPANSION COEFFICIENT (C^-1)

TB,    PIEZ,    4
TBDATA,         3,    0.1E-4
TBDATA,         6,    0.1E-4
TBDATA,         9,    0.1E-4
TBDATA,         14,   0.1E-4
TBDATA,         16,   0.1E-4

MP,    PERX,    4,    1E-3
MP,    PERY,    4,    1E-3
MP,    PERZ,    4,    1E-3
```

Table A.13 Material properties of aluminium alloy 6061 T6, defined as Material 4 [72]

The defined properties to model the film heaters are described in Table A.14. The properties of the film heaters are acquired form the study conducted by Song *et al.* in [7]. The film heaters are used in the benchmark model, and the models to verify the compensation performance of the ADSA and ABA.

```
/COM  FILM HEATER MATERIAL PROPERTIES
MP,   DENS,   5,   1420     !DENSITY (KG M^-3)
MP,   EX,     5,   7.1E10   !YOUNGS MODULUS (PA)
MP,   NUXY,   5,   0.33     !POISSON'S RATIO
MP,   C,      5,   1090     !SPECIFIC HEAT (J KG^-1 C^-1)
MP,   KXX,    5,   0.12     !THERMAL CONDUCTIVITY (W M^-1 C^-1)
MP,   ALPX,   ,    3.2E-5   !THERMAL EXPANSION COEFFICIENT (C^-1)

TB,   PIEZ,   5
TBDATA,       3,   0.1E-4
TBDATA,       6,   0.1E-4
TBDATA,       9,   0.1E-4
TBDATA,       14,  0.1E-4
TBDATA,       16,  0.1E-4

MP,   PERX,   5,   1E-3
MP,   PERY,   5,   1E-3
MP,   PERZ,   5,   1E-3
```

Table A.14 Material properties of the film heaters, defined as Material 5 [7]

Bibliography

[1] S. Y. Ho and A. Paull, "Coupled thermal, structural and vibrational analysis of a hypersonic engine for flight test," *Aerospace science and technology*, vol. 10, pp. 420-426, July 2006.

[2] NASA, "NASA's X-43A Scramjet", Source: http://apod.nasa.gov/apod/ap040329.html. Date Accessed: 28/10/2011.

[3] Z. Gubinyi, C. Batur, A. Sayir, and F. Dynys, "Electrical properties of PZT piezoelectric ceramic at high temperatures," *Journal of Electroceramics*, vol. 20, pp. 95-105, 2008.

[4] S. Sherrit, G. Yang, H. Wiederick, and B. Mukherjee, "Temperature dependence of the dielectric, elastic and piezoelectric material constants of lead zirconate titanate ceramics," *Journal of Applied Physics*, vol. 42, pp. 2219-2230, 1971.

[5] B. Berton, "Shape Memory Alloys Application: Trailing Edge Shape Control," Dassault Aviation, Saint-Cloud, 01 October 2006.

[6] D. G. Cole and R. L. Clark, "Adaptive compensation of piezoelectric sensoriactuators," *Journal of Intelligent Material Systems and Structures*, vol. 5, p. 665, 1994.

[7] G. Song, X. Zhou, and W. Binienda, "Thermal deformation compensation of a composite beam using piezoelectric actuators," *Smart Materials and Structures*, vol. 13, p. 30, 2004.

[8] P. Binette, M. L. Dano, and G. Gendron, "Active shape control of composite structures under thermal loading," *Smart Materials and Structures*, vol. 18, p. 025007, 2009.

[9] D. J. Leo, *Engineering analysis of smart material systems*: John Wiley & Sons, Inc., 2007.

[10] C. Rogers and V. Giurgiutiu, "2. Concepts of Adaptronic Structures," *Adaptronics and Smart Structures: Basics, Materials, Design, and Applications*, p. 1641, 1999.

[11] R. W. Moses, A. S. Pototzky, D. A. Henderson, S. C. Galea, D. S. Manokaran, D. G. Zimcik, V. Wickramasinghe, D. M. Pitt, and M. A. Gamble, "Controlling Buffet Loads by Rudder and Piezo-Actuation," presented at the International Forum on Aeroelasticity and Structural Dynamics, Munich, 2005.

[12] A. J. Fleming and S. O. R. Moheimani, "Spatial system identification of a simply supported beam and a trapezoidal cantilever plate," *IEEE Transactions on Control Systems Technology*, vol. 11, pp. 726-736, 2003.

[13] Q. Chen, D. Natale, B. Neese, K. Ren, M. Lin, Q. Zhang, M. Pattom, K. Wang, H. Fang, and E. Im, "Piezoelectric polymers actuators for precise shape control of large scale space antennas," *Electroactive Polymer Actuators and Devices*, vol. 6524, 2007.

[14] H. P. Monner, "Smart materials for active noise and vibration reduction," presented at the Noise and Vibration: Emerging Methods, Saint-Raphael, France, 2005.

[15] F. Doengi, U. Herold-Schmidt, and E. Floeth, "Space qualification of smart structures for vibration and shape control," presented at the Proceedings European Conference on Spacecraft Structures, Materials and Mechanical Testing, Braunschweig, Germany, 1999.

[16] S. Sherrit, X. Bao, Y. Bar-Cohen, and Z. Chang, "Resonance analysis of high temperature piezoelectric materials for actuation and sensing," presented at the SPIE Smart Structures Conference, San Diego, CA, 2004.

[17] R. Kažys, A. Voleišis, and B. Voleišien "High temperature ultrasonic transducers: review," *Ultragarsas (Ultrasound)*, vol. 63, pp. 7–17, 2008.

[18] APC. (2010). *First Steps towards Piezoaction*. Available: http://www.americanpiezo.com/stack-actuator-book.html. Date Accessed: 28/10/2011.

[19] A. Kawamata, H. Hosaka, and T. Morita, "Non-hysteresis and perfect linear piezoelectric performance of a multilayered lithium niobate actuator," *Sensors and Actuators A: Physical*, vol. 135, pp. 782-786, 2007.

[20] A. Sofla, D. Elzey, and H. Wadley, "Two-way antagonistic shape actuation based on the one-way shape memory effect," *Journal of Intelligent Material Systems and Structures*, vol. 19, pp. 1017-1027, 2008.

[21] L. Shili, G. Wenjie, and L. Shujun, "Optimal Design of Compliant Trailing Edge for Shape Changing," *Chinese Journal of Aeronautics*, vol. 21, pp. 187-192, 2008.

[22] D. P. Wang, J. D. Bartley-Cho, C. A. Martin, and B. J. Hallam, "Development of high-rate large-deflection hingeless trailing-edge control surface for the Smart Wing wind tunnel model," *Proceedings of SPIE*, vol. 4332, pp. 407-417, 2001.

[23] S. Barbarino, S. Ameduri, and L. Lecce, "Wing Shape Control through an SMA-Based Device," *Journal of Intelligent Material Systems and Structures*, vol. 20, pp. 283-296, 2009.

[24] F. Claeyssen, N. Lhermet, and T. Maillard, "Magnetostrictive actuators compared to piezoelectric actuators," *Proceedings of SPIE*, vol. 4763, pp. 194-200, 2003.

[25] L. Sandlund, M. Fahlander, T. Cedell, A. E. Clark, J. B. Restorff, and M. Wun-Fogle, "Magnetostriction, elastic moduli, and coupling factors of composite Terfenol-D," *Journal of Applied Physics*, vol. 75, pp. 5656-5658, 1994.

[26] R. Kellogg and A. Flatau, "Blocked force investigation of a Terfenol-D transducer," presented at the SPIE's 6th Annual International Symposium on Smart Structures and Materials, 1999.

[27] R. Kellogg and A. Flatau, "Experimental Investigation of Terfenol-D's Elastic Modulus," *Journal of Intelligent Material Systems and Structures*, vol. 19, pp. 583-595, 2008.

[28] R. C. Fenn, J. R. Downer, D. A. Bushko, V. Gondhalekar, and N. D. Ham, "Terfenol-D driven flaps for helicopter vibration reduction," *Smart Materials and Structures,* vol. 5, pp. 49-57, 1996.

[29] G. Friedmann and T. Millott, "Magnetostrictively actuated control flaps for vibration reduction in helicopter rotors - design considerations for implementation," *Mathematical and computer modelling,* vol. 33, pp. 1203-1217, 2001.

[30] T. Zhang, C. Jiang, H. Zhang, and H. Xu, "Giant magnetostrictive actuators for active vibration control," *Smart Materials and Structures,* vol. 13, pp. 473-477, 2004.

[31] H. Kawai, "The piezoelectricity of poly (vinylidene fluoride)," *Japanese Journal of Applied Physics,* vol. 8, pp. 975-976, 1969.

[32] H. Irschik, "A review on static and dynamic shape control of structures by piezoelectric actuation," *Engineering Structures,* vol. 24, pp. 5-11, 2002.

[33] D. B. Koconis, L. P. Kollár, and G. S. Springer, "Shape control of composite plates and shells with embedded actuators. I. Voltages specified," *Journal of Composite Materials,* vol. 28, pp. 415-458, 1994.

[34] D. B. Koconis, L. P. Kollar, and G. S. Springer, "Shape control of composite plates and shells with embedded actuators. II. Desired shape specified," *Journal of Composite Materials,* vol. 28, pp. 262-285, 1994.

[35] T. I. Thinh and L. K. Ngoc, "Static behavior and vibration control of piezoelectric cantilever composite plates and comparison with experiments," *Computational Materials Science,* vol. 49, pp. S276-S280, 2010.

[36] K. Chandrashekhara and S. Varadarajan, "Adaptive shape control of composite beams with piezoelectric actuators," *Journal of Intelligent Material Systems and Structures,* vol. 8, pp. 112-124, 1997.

[37] L. Ren, "A theoretical study on shape control of arbitrary lay-up laminates using piezoelectric actuators," *Composite Structures,* vol. 83, pp. 110-118, 2008.

[38] Q. Luo and L. Tong, "High precision shape control of plates using orthotropic piezoelectric actuators," *Finite elements in analysis and design*, vol. 42, pp. 1009-1020, 2006.

[39] L. L. Howell, *Compliant Mechanisms*: John Wiley & Sons, 2001.

[40] C. Mangeot, B. Andersen, and R. Hilditch. (2010). New actuators for aerospace. Available: http://www.noliac.com/Files/Billeder/05%20News/Diamond_actuator_for_aerospace.pdf. Date Accessed: 28/10/2011.

[41] D. Heverly, K. Wang, and E. Smith, "Dual-stack piezoelectric device with bidirectional actuation and improved performance," *Journal of Intelligent Material Systems and Structures*, vol. 15, pp. 565-574, 2004.

[42] S. Bharti and M. I. Frecker, "Optimal design and experimental characterization of a compliant mechanism piezoelectric actuator for inertially stabilized rifle," *Journal of Intelligent Material Systems and Structures*, vol. 15, pp. 93-106, 2004.

[43] E. V. Ardelean, D. G. Cole, and R. L. Clark, "High Performance V-stack Piezoelectric Actuator," *Journal of Intelligent Material Systems and Structures*, vol. 15, pp. 879-889, 2004.

[44] H. Zhou, B. Henson, A. Bell, A. Blackwood, A. Beck, and R. Burn. Linear Piezo-Actuator and its applications. Available: http://zhouhx.tripod.com/piezopaper.pdf. Date Accessed: 28/10/2011.

[45] R. C. Sneed, R. R. Smith, M. F. Cash, and E. H. Anderson, "Smart-material based hydraulic pump system for actuation of a morphing wing," presented at the 48th AIAA/ASME/ASCE/AHS/ASC Structures, Structural Dynamics and Materials Conference, Hawaii, 2007.

[46] E. H. Anderson, G. L. Bales, and E. V. White, "Application of smart material-hydraulic actuators," presented at the Smart Structures and Materials 2003: Industrial and Commercial Applications of Smart Structures Technologies, San Diego, CA, USA, 2003.

[47] E. H. Anderson, J. E. Lindler, and M. E. Regelbrugge, "Design and Testing of Piezoelectric-Hydraulic Actuators," presented at the Smart Structures and Materials 2003: Industrial and Commercial Applications of Smart Structures Technologies, San Diego, CA, USA, 2003.

[48] H. Zhou and B. Henson, "Analysis of a diamond-shaped mechanical amplifier for a piezo actuator," *The International Journal of Advanced Manufacturing Technology,* vol. 32, pp. 1-7, 2007.

[49] Q. Xu and Y. Li, "Analytical modeling, optimization and testing of a compound bridge-type compliant displacement amplifier," *Mechanism and Machine Theory,* vol. 46, pp. 183-200, 2010.

[50] M. Pozzi and T. King, "Piezoelectric actuators in micropositioning," *Engineering Science and Education Journal,* vol. 10, pp. 31-36, 2002.

[51] J. M. Breguet, R. Perez, A. Bergander, C. Schmitt, R. Clavel, and H. Bleuler, "Piezoactuators for motion control from centimeter to nanometer," presented at the Proceedings of the 2000 IEEE/RSJ International Conference on Intelligent Robots and Systems, 2000.

[52] J. Kim and J. H. Lee, "Self-moving cell linear motor using piezoelectric stack actuators," *Smart Materials and Structures,* vol. 14, pp. 934-940, 2005.

[53] C. Potthast, R. Eisseler, D. Klotz, J. Wallaschek, and U. Heisel, "Piezoelectric actuator design for ultrasonically assisted deep hole drilling," *Journal of Electroceramics,* vol. 20, pp. 187-192, 2008.

[54] D. G. Lee, S. W. Or, and G. P. Carman, "Design of a piezoelectric-hydraulic pump with active valves," *Journal of Intelligent Material Systems and Structures,* vol. 15, pp. 107-115, 2004.

[55] Cedrat Technologies. *Amplified Piezoelectric Actuators*. Available: http://www.cedrat.com/en/mechatronic-products/actuators/apa.html. Date Accessed: 28/10/2011.

[56] Dynamic Structures & Materials. *FPA FlexFrame PiezoActuator™*. Available: http://www.dynamic-structures.com/Actuators/#FPA. Date Accessed: 28/10/2011.

[57] "IEEE Standard on Piezoelectricity," *ANSI/IEEE Std 176-1987*, 1988.

[58] Physik Instrumente, "Orthogonal system describing the properties of a poled piezoelectric ceramic", Source: http://www.physikinstrumente.com. Date Accessed: 28/10/2011.

[59] ANSYS. (2010). *ANSYS Mechanical APDL Coupled-Field Analysis Guide*. Date Accessed: 01/10/2011.

[60] G. R. Liu and S. S. Quek, *The Finite Element Method: A Practical Course*: Butterworth Heinemann, 2003.

[61] ANSYS. (2010). *ANSYS Mechanical APDL Element Reference*. Date Accessed: 02/10/2011.

[62] ANSYS. (2010). *ANSYS Mechanical APDL and Mechanical Applications Theory Reference*. Date Accessed: 01/10/2011.

[63] F. Pigache. (2007). *Conversion of Piezoelectric Material for Ansys. Source: http://smartmaterials.free.fr/ressources.html*. Date Accessed: 28/10/2011.

[64] D. H. Johnson and D. Pal. Simulation of an Ultrasonic Piezoelectric Transducer. Available: http://www.ohiocae.com/piezo-paper.htm. Date Accessed: 28/10/2011.

[65] Physik Instrumente, "Electrical design of a stack translator", Source: http://www.physikinstrumente.com. Date Accessed: 28/10/2011.

[66] ANSYS Mechanics Group, "Contact Analysis in ANSYS," in *2004 International ANSYS Conference*, 2004.

[67] eFunda. *Material properties of AISI Type 304 Stainless steel*. Available: http://www.efunda.com/materials/alloys/stainless_steels/show_stainless.cfm?id=aisi_type_304&prop=all&page_title=aisi%20type%20304. Date Accessed: 28/10/2011.

[68] P. Binette, M. Dano, and G. Gendron, "Active shape control of composite structures under thermal loading," *Smart Materials and Structures*, vol. 18, pp. 1-12, 2009.

[69] S. Mekid and B. Lim, "Characteristics comparison of piezoelectric actuators at low electric field: analysis of strain and blocking force," *Smart Materials and Structures*, vol. 13, p. N93, 2004.

[70] eFunda. *Material properties of Lead Zirconate Titanate PZT-5H*. Available: http://www.efunda.com/materials/piezo/material_data/matdata_output.cfm?Material_ID=PZT-5H. Date Accessed: 28/10/2011.

[71] APC. "Piezo Mechanical and Electrostrictive Stack and Ring Actuators: Product Range & Technical Data," *APC_International*. Available: http://www.americanpiezo.com/images/stories/content_images/pdf/APC_Stack_Specs.pdf. Date Accessed: 28/10/2011

[72] ASM. *Material properties of Aluminum 6061-T6*. Available: http://asm.matweb.com/search/SpecificMaterial.asp?bassnum=MA6061t6. Date Accessed: 28/10/2011.